Aalto University
School of Science
and Technology

TECHNISCHE
UNIVERSITÄT
DRESDEN

Faculty of Electronics, Communications and Automation Department of Radio Science and Engineering

Final Project

NON-RADIATING WAVEGUIDE WITH HIGH PERMITTIVITY DIELECTRIC AND ANTENNAS BASED ON IT

Bernhard Beuerle
Dresden University of Technology

Supervised by:
Prof. Antti Räisänen
Dr. Sergey Dudorov
Dr.-Ing. Dirk Plettemeier
Dipl.-Ing. Michael Jenning

Submitted on 27th July 2010

ABSTRACT

In this thesis the propagation characteristics of non-radiating dielectric waveguides (NRD guide) and its feasibility for end-fire and leaky-wave antenna structures in the W frequency band were studied. To obtain the propagation constant, MARCATILI's approximation method was extended to be used with NRD guides and the outcome was verified with simulation results. In order to connect the NRD guide to standard metal waveguides a new direct connection transition was developed and a prototype was manufactured and measured. Based on the concept of a dielectric rod waveguide antenna an NRD guide end-fire antenna is presented and verified experimentally based on the the same experimental NRD guide used for the transition. Furthermore a concept for a new type of periodic leaky-wave antenna based on the NRD guide is presented, where high impedance surfaces allow the radiated electromagnetic wave to propagate out of the waveguide structure.

TABLE OF CONTENTS

LIST OF ABBREVIATIONS **III**

LIST OF SYMBOLS **V**

1 INTRODUCTION **1**

2 NON-RADIATING DIELECTRIC WAVEGUIDES **3**

2.1 Basic principles 3

2.1.1 MAXWELL's equations 3

2.1.2 Standard metal waveguides 8

2.1.3 Dielectric rod waveguides 10

2.1.4 Non-radiating dielectric waveguides 12

2.2 NRD guide model 15

2.3 MARCATILI's method for non-radiating dielectric waveguides 19

2.4 Standard metal waveguide to NRD guide transition 43

2.4.1 Design 43

2.4.2 Simulation results 44

2.4.3 Measurement results 49

3 NON-RADIATING DIELECTRIC WAVEGUIDE ANTENNAS **53**

3.1 Basic principles 54

3.1.1 Antenna parameters 54

3.1.2 Leaky-wave antennas 57

3.1.3 High impedance surfaces 60

3.2 NRD guide end-fire antenna 62

3.2.1 Design 62

3.2.2 Simulation results 63

3.2.3 Measurement results 69

3.3 NRD guide leaky-wave antennas 77

3.3.1 Design 77
3.3.2 Simulation results 81

4 CONCLUSIONS **88**

5 OUTLOOK **90**

APPENDICES **91**

A FIGURES **91**
A.1 NON-RADIATING DIELECTRIC WAVEGUIDES 91
A.1.1 NRD guide model 91
A.1.2 MARCATILI's method for non-radiating dielectric waveguides 94
A.1.3 Standard metal waveguide to NRD guide transition 98
A.2 NON-RADIATING DIELECTRIC WAVEGUIDE ANTENNAS 108
A.2.1 NRD guide end-fire antenna 108
A.2.2 NRD guide leaky-wave antennas 113

B LISTINGS **115**

C LONGITUDINAL AND TRANSVERSE FIELD COMPONENTS **117**

D PROPAGATION CONSTANT **119**

E DIELECTRIC ROD WAVEGUIDE ANTENNA **123**

BIBLIOGRAPHY **132**

LIST OF FIGURES **139**

LIST OF ABBREVIATIONS

AUT ..... Antenna Under Test

DRW ..... Dielectric Rod Waveguide

DRWA ..... Dielectric Rod Waveguide Antenna

DUT ..... Device Under Test

FEM ..... Finite Element Method

FF ..... Far-Field

FSS ..... Frequency Selective Surface

HFSS ..... High Frequency Structure Simulator

HIS ..... High Impedance Surface

LSE mode ..... Longitudinal Section Electric Mode

LSM mode .... Longitudinal Section Magnetic Mode

MMIC ..... Monolithic Microwave Integrated Circuit

MVNA ..... Millimeter Vector Network Analyzer

NF ..... Near-Field

NRD guide .... Nonradiating Dielectric Waveguide

PEC ..... Perfect Electric Conductor

PMC ..... Perfect Magnetic Conductor

RBC ..... Radiation Boundary Condition

RWG ..... Rectangular Waveguide

TE mode ..... Transverse Electric Mode

TEM mode .... Transverse Electromagnetic Mode

TM mode ..... Transverse Magnetic Mode

VNA ..... Vector Network Analyzer

LIST OF SYMBOLS

α	attenuation constant	Np/m
β	phase constant	rad/m
Δs	scan step size	mm
$\Delta\theta$	beam width	deg
γ	propagation constant	–
λ	wavelength	m
λ_0	wavelength in free space	m
λ_g	guide wavelength	m
$\mathbf{B}$	magnetic flux density vector	T
$\mathbf{D}$	electric displacement field vector	C/m^2
$\mathbf{E}$	electric field vector	V/m
$\mathbf{e}$	versor of the cartesian coordinate system	–
$\mathbf{E}_t$	transverse electric field vector	V/m
$\mathbf{H}$	magnetic field vector	A/m
$\mathbf{H}_t$	transverse magnetic field vector	A/m
$\mathbf{J}_s$	electric surface current density vector	A/m^2
$\mathbf{M}$	magnetization vector	A/m
$\mathbf{M}_s$	magnetic surface current density vector	V/m
$\mathbf{n}$	normal vector	–

$\mathbf{P}$	polarization density vector	$\mathrm{C/m^2}$
$\mathcal{E}$	time-dependent electric field vector	$\mathrm{V/m}$
$\mathcal{H}$	time-dependent magnetic field vector	$\mathrm{A/m}$
∇	vector differential operator	–
∇_t	transverse vector differential operator	–
ω	angular frequency	$\mathrm{s^{-1}}$
ϕ	azimuth angle	deg
Ψ	vector field	–
θ	zenith angle	deg
θ_m	beam angle	deg
θ_{max}	maximum vertical scanning angle	deg
φ_{max}	maximum horizontal scanning angle	deg
C	capacitance	F
D	antenna directivity	dB
D_0	maximum antenna directivity	dB
d_m	AUT - probe measurement distance	mm
E	electric field component	$\mathrm{V/m}$
e	antenna radiation efficiency	–
e_c	conductive efficiency	–
e_c	dielectric efficiency	–
f	frequency	Hz
G	antenna gain	dB
G_0	maximum antenna gain	dB
H	magnetic field component	$\mathrm{A/m}$

k	wavenumber	m^{-1}
k_0	wavenumber in free space	m^{-1}
k_x	wavenumber component in x -direction	m^{-1}
k_y	wavenumber component in y -direction	m^{-1}
k_z	wavenumber component in z -direction	m^{-1}
L	inductance	H
s_{11}	s-parameter reflection coefficient	dB
s_{21}	s-parameter transmission coefficient	dB
t	time	s

Constants

μ	permeability	$\mathrm{H/m}$
μ_0	permeability of free space	$\mathrm{H/m}$
ρ	charge density	$\mathrm{C/m^3}$
ε	permittivity, dielectric tensor	$\mathrm{F/m}$
ε_0	permittivity of free space	$\mathrm{F/m}$
ε_r	relative permittivity	–
c	speed of light in free space	$\mathrm{m/s}$
n	refractive index	–

Dimensions

A	antenna diameter	mm
a	width of dielectric rod	mm
b	height of dielectric rod	mm
d	distance of metal plates	mm
dl	length of discontinuity	mm

dw	width of discontinuity	mm
g	gap between dielectric and metal plate	mm
h	height of the NRD guide	mm
l	length of NRD guide section	mm
m	length of taper section	mm
p	period of discontinuities	mm
R	FRAUNHOFER distance	mm
s	metal plate offset	mm
t	metal thickness	mm
u	inner height of standard metal waveguide	mm
w	inner width of standard metal waveguide	mm
x_max	maximum horizontal scan movement	m
y_max	maximum vertical scan movement	m

1 INTRODUCTION

The non-radiating dielectric waveguide (NRD guide) is a waveguide for the millimeter wave frequency range which offers interesting properties. It can be considered as a standard metal waveguide with the upper and lower plates removed, and the sidewalls extended and placed closer to each other. Its structure is similar to that of an H-guide, however it is capable of suppressing radiation loss, which is a problem with dielectric waveguides.

Using high permittivity dielectric materials it is possible to design dielectric rod waveguides (DRW) for high frequencies with small dimensions, enabling transitions to the standard metal waveguide. By chosing high permittivity dielectric materials with a low dielectric loss tangent for the dielectric material in the NRD guide, the NRD guide can be used in the desired W frequency band ranging from 75 to 110 GHz and transitions to other waveguides can be introduced so that the NRD guide can be integrated in millimeter wave circuits. The research for this thesis was carried out during a study visit at the Department of Radio Science and Engineering[1] at Aalto University[2] School of Science and Technology[3] (formerly known as Helsinki University of Technology) in Espoo, Finland. Based on previous research on dielectric rod waveguides in the W frequency band at the department, the propagation characteristics of NRD guides and its feasibility for both end-fire and leaky-wave antenna structures were studied in this thesis.

MARCATILI's method is an approximation method used for rectangular shaped dielectric waveguides to estimate the propagation constant. In this thesis MARCATILI's method was extended to be used for NRD guides. The knowledge of the propagation constant of the NRD guide mode of operation is crucial for the design of periodic leaky-wave antennas. After theoretically deriving the approx-

[1] http://radio.tkk.fi/en/
[2] http://www.aalto.fi/en/
[3] http://www.tkk.fi/en/

imation method based on the assumptions used in MARCATILI's method, the results were compared to the dispersion characteristics obtained by simulating the NRD guide structure with the finite element method solver Ansoft[4] HFSS (High Frequency Structural Simulator).

In order to connect an NRD guide to a standard metal waveguide, a proper transition is needed. This transition should offer low reflection, good transmission characteristics and should be easy to manufacture. Therefore different types of transitions were studied. A experimental prototype of the transition was then assembled and measured. Previously certain DRW end-fire antennas were presented at the Department of Radio Science and Engineering, also for the W band. Based on that concept, and NRD guide end-fire antenna was developed. The prototype of the transition was then used for the measurement of the radiation characteristics of the NRD guide end-fire antenna. The experimental end-fire antenna was therefore measured in the anechoic antenna chamber of the deparment. To verify the radiation characteristics, the results were compared to the ones obtained from simulating the structure within HFSS. As mentioned before, the NRD guide suppresses radiation out of the structure while operating in the mode for which the electric field is parallel to the metal plates. In this thesis a concept for periodic leaky-wave antennas based on NRD guides is presented. In order to allow radiation, caused by introduced discontinuities, out of the waveguide structure, the properties of the sidewalls need to be changed. High impedance surfaces (HIS) can be placed on the inner surface of the metal plates to alter its characteristics and make the antenna structure leaky. HIS are frequency selective surfaces (FSS), however at previous research at the Department of Radio Science and Engineering a voltage controlled HIS was presented. This offers interesting possibilities also for the proposed leaky-wave antenna concept.

[4] http://www.ansoft.com/

2 NON-RADIATING DIELECTRIC WAVEGUIDES

In this chapter the propagation characteristics of non-radiating dielectric waveguides (NRD guide) in the **W** frequency band ranging from 75 to 110 GHz are discussed and MARCATILI's method was extended to be used for NRD guides. The results of the calculated propagation characteristics were then verified by simulation results using the finite element method (FEM) solver Ansoft HFSS. Furthermore a novel metal waveguide to NRD guide transition is presented. The simulated results of the transition were verified with an experimental NRD guide.

2.1 Basic principles

2.1.1 MAXWELL's equations

The MAXWELL equations are a set of four differential equations giving the relations between the electric and magnetic field and their sources. Their differential forms are given as [1]

$$\nabla \cdot \mathbf{D} = \rho \tag{2.1a}$$

$$\nabla \cdot \mathbf{B} = 0 \tag{2.1b}$$

$$\nabla \times \mathbf{E} = -\frac{\partial \mathbf{B}}{\partial t} \tag{2.1c}$$

$$\nabla \times \mathbf{H} = \mathbf{J}_f + \frac{\partial \mathbf{D}}{\partial t} \tag{2.1d}$$

with (2.1a) being GAUSS's law, (2.1b) GAUSS's law for magnetism, (2.1c) FARADAY's law and (2.1d) AMPÈRE's circuital law with MAXWELL's correction where **D** is the electric displacement field, **B** the magnetic flux density field, **E** the electric field and **H** the magnetic intensity field.

The electric displacement field is related to the electric field with the polarization density **P**:

$$\mathbf{D} = \varepsilon_0 \mathbf{E} + \mathbf{P} \tag{2.2}$$

where ε_0 is the permittivity of free space. In a linear, homogeneous and isotropic dielectric equation (2.2) is

$$\mathbf{D} = \varepsilon \mathbf{E} \tag{2.3}$$

where $\varepsilon = \varepsilon_r \varepsilon_0$ is the permittivity and ε_r the relative permittivity of the material.

The magnetic field intensity and the magnetic flux density are related to each other with the magnetization **M**:

$$\mathbf{H} = \frac{\mathbf{B}}{\mu_0} - \mathbf{M} \tag{2.4}$$

where μ_0 is the permeability of free space. If there exists an approximately linear relationship between **M** and **H**, which is the case for a large class of magnetic materials [1], **H** and **B** are also related linearly to each other and equation (2.4) simplifies to

$$\mathbf{B} = \mu_0 \mu \mathbf{H} \tag{2.5}$$

where μ is the permeability of the material. For a more detailed discussion of MAXWELL's equations refer to [1].

Boundary conditions

The boundary conditions at the interface between two general medias are derived from MAXWELL's equations [2]:

$$\mathbf{n} \cdot (\mathbf{D}_2 - \mathbf{D}_1) = \rho_{es} \ , \tag{2.6a}$$

$$\mathbf{n} \cdot (\mathbf{B}_2 - \mathbf{B}_1) = \rho_{ms} \ , \tag{2.6b}$$

$$\mathbf{n} \times (\mathbf{E}_2 - \mathbf{E}_1) = -\mathbf{M}_s \ , \tag{2.6c}$$

$$\mathbf{n} \times (\mathbf{H}_2 - \mathbf{H}_1) = \mathbf{J}_s \ , \tag{2.6d}$$

where [3] ρ_{es} is the electric surface charge density, ρ_{es} the magnetic surface charge density, $\mathbf{M}_s$ the magnetic surface current density, $\mathbf{J}_s$ the electric surface

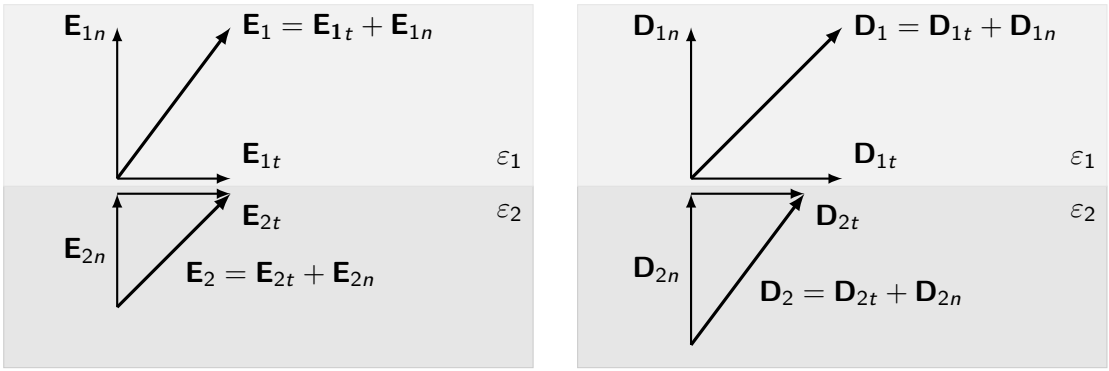

Figure 2.1: *Decomposition of the (a) electric field and (b) electric flux density at the interface of two dielectrics with different relative permittivity into tangential and nominal components*

current density and **n** is the unit normal vector.

Figure 2.1 illustrates the decomposition of the electric field and the electric flux density into their tangential and normal components at the boundary of two dielectrics with different relative permittivity. The tangential component of the electric field is continous across that boundary,

$$\mathbf{E}_{1t} = \mathbf{E}_{2t} \ , \tag{2.7}$$

whereas for the electric flux density **D** the normal component is continous across the boundary. With $\mathbf{D} = \varepsilon\mathbf{E} = \varepsilon_0\varepsilon_r\mathbf{E}$ the second boundary condition for the electric field then is:

$$\varepsilon_{r1}\mathbf{E}_{1n} = \varepsilon_{r2}\mathbf{E}_{2n} \ . \tag{2.8}$$

The conditions for the magnetic field intensity **H** and the magnetic flux density **B** at the interface of two media with different permeability $\mu_1 \neq \mu_2$ can be obtained similar to the conditions for **E** and **D** [1]:

$$\mathbf{H}_{1t} = \mathbf{H}_{2t} \ , \tag{2.9}$$

and with $\mathbf{B} = \mu\mu_0\mathbf{H}$

$$\mu_1\mathbf{H}_{1n} = \mu_2\mathbf{H}_{2n} \ . \tag{2.10}$$

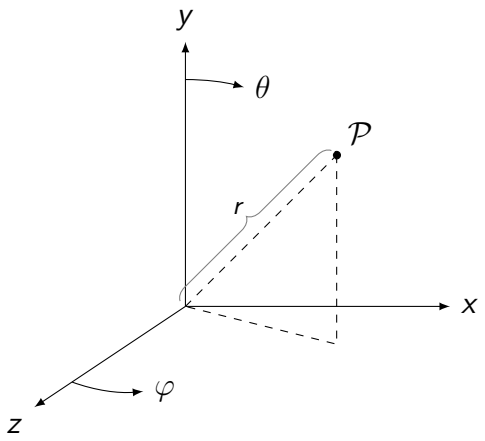

Figure 2.2: *Cartesian and polar coordinate system*

Wave equation

The propagation constant γ of a wave traveling along the z -direction with the form

$$\mathcal{E}(x, y, z) = \mathbf{E}(x, y) \cdot e^{-\gamma z} \,, \tag{2.11a}$$

$$\mathcal{H}(x, y, z) = \mathbf{H}(x, y) \cdot e^{-\gamma z} \tag{2.11b}$$

is defined as

$$\gamma = \alpha + j\beta \,, \tag{2.12}$$

where α is the attenuation constant and β the phase constant.

A field which is both a function of time and space is refered to as a *wave*. Being more restrictive with the defintion, a wave is a solution of a *wave equation* [4]. Thus, the electric and magnetic field have to fulfill the HELMHOLTZ equation

$$\nabla^2 \Psi + k^2 \Psi = 0 \,, \tag{2.13}$$

where $k = k_0\sqrt{\varepsilon_r}$ is the wavenumber in the region of propagation and k_0 the wavenumber in free space. The wavenumber is the spatial equivalent to frequency telling the number of radians per unit length and it is real valued for lossless media and complex valued for lossy media. The HELMHOLTZ equation is a

special case of the wave equation in three dimensions and gives

$$\left(\frac{\partial^2}{\partial x^2}+\frac{\partial^2}{\partial y^2}+\frac{\partial^2}{\partial z^2}\right)\cdot\mathbf{E}+k^2\cdot\mathbf{E}=0\,, \tag{2.14a}$$

$$\left(\frac{\partial^2}{\partial x^2}+\frac{\partial^2}{\partial y^2}+\frac{\partial^2}{\partial z^2}\right)\cdot\mathbf{H}+k^2\cdot\mathbf{H}=0 \tag{2.14b}$$

for the electric and magnetic field respectively (the coordinate system is illustrated in *Figure 2.2*). If a time harmonic wave $\mathbf{E},\mathbf{H}\sim e^{j\omega t}$ is considered, the propagating electric and magnetic wave can be described as

$$\mathcal{E}(x,y,z,t)=\mathbf{E}\cdot e^{j(\omega t-k_x x-k_y y-k_z z)}\,, \tag{2.15a}$$

$$\mathcal{H}(x,y,z,t)=\mathbf{H}\cdot e^{j(\omega t-k_x x-k_y y-k_z z)}\,. \tag{2.15b}$$

To get the relation for the wavenumber components of the propagating wave, the HELMHOLTZ equation for either the electric or the magnetic field is calculated. Inserting the electric wave equation (2.15a) into equation (2.14a) leads to

$$-\left(k_x^2+k_y^2+k_z^2\right)\cdot\mathbf{E}+k^2\cdot\mathbf{E}=0\,. \tag{2.16}$$

and subsequently to the equation for the cartesian wavenumber components:

$$k_x^2+k_y^2+k_z^2=k^2\,. \tag{2.17}$$

If the z -axis is defined as the direction of propagation, the k_z wavenumber component tells us for a given frequency the speed with which the nodes of the wave are propagating along the guiding structure [5] and is equal to β in equation (2.12). As time harmonic waves are considered, MAXWELL's equations (2.1c) and (2.1d) can be rewritten as (using $\frac{\partial}{\partial t}=j\omega$)

$$\nabla\times\mathbf{H}=j\omega\varepsilon\mathbf{E}\,, \tag{2.18a}$$

$$-\nabla\times\mathbf{E}=j\omega\mu\mathbf{H}\,. \tag{2.18b}$$

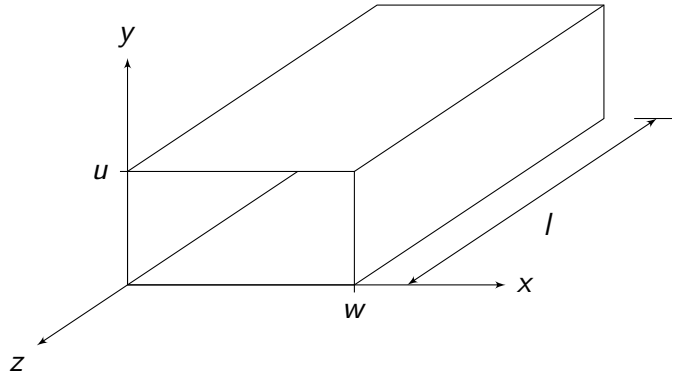

Figure 2.3: *Schematic model of a WR-10 rectangular waveguide for the **W** band having the inner dimensions* [mm] $w = 2.54$ *and* $u = 1.27$ *[6]*

2.1.2 Standard metal waveguides

Hollow metal waveguides are not supporting *transversal electromagnetic* (*TEM*) waves, but instead the propagating waves are *transversal electric* (*TE*) and *transversal magnetic* (*TM*) waves. The most common hollow waveguide has a rectangular cross-section as sketched in *Figure 2.3*. It is standardized with different sizes for frequencies as high as 333 GHz [6].

For *TE* modes for which the electric field has no component in the direction of propagation, the wavenumber components k_x and k_y can be derived by applying boundary conditions as [6]

$$k_x = \frac{n\pi}{w}, \qquad n = 0, 1, 2, ... \tag{2.19}$$

$$k_y = \frac{m\pi}{u}, \qquad m = 0, 1, 2, ... \tag{2.20}$$

and now equation (2.17) can be written as

$$k_z = \sqrt{\left(\frac{2\pi}{\lambda_0}\right)^2 - \left(\frac{n\pi}{w}\right)^2 - \left(\frac{m\pi}{u}\right)^2}. \tag{2.21}$$

For the TE_{10} mode (the distribution of the electric and magnetic field is illustrated in *Figure 2.4a*) the electric field in the waveguide has the form shown in *Figure 2.4b*,

$$E_y = E_0 \sin k_x x e^{\omega t - k_z z} \tag{2.22}$$

with $m = 0$, and thus $k_y = 0$. The guide wavelength of the waveguide is calculated

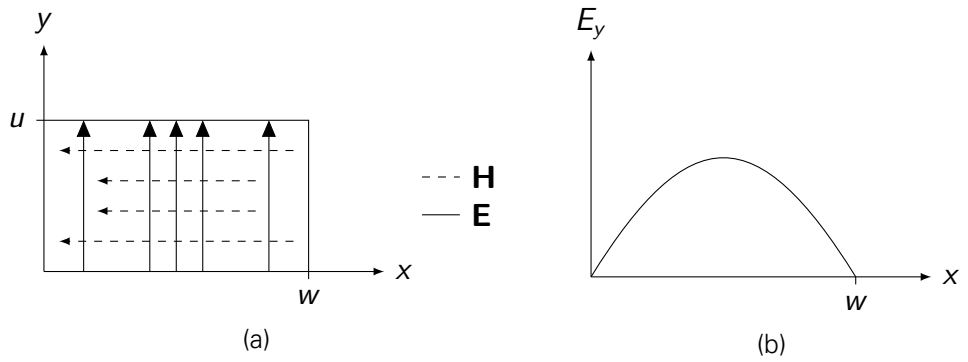

Figure 2.4: *(a) Electric and magnetic field lines for the TE_{10} mode in the cross-sectional plane of a rectangular waveguide [6] and (b) the distribution of the electric field for some value of z [5]*

by [6]

$$\lambda_g = \frac{2\pi}{\beta} = \frac{\lambda_0}{\sqrt{1-(\lambda_0/\lambda_c)^2}} = \frac{\lambda_0}{\sqrt{1-(f_c/f_0)^2}}\,, \tag{2.23}$$

where λ_0 is the free-space wavelength and λ_c and f_c the cut-off wavelength and frequency, respectively. For high frequencies equation (2.23) approaches the free-space wavelength λ_0, whereas for lower frequencies the value inside the square root of equation (2.21) eventually becomes negative. For the case that $\lambda_0 > 2w$ equation (2.21) for the TE_{10} mode turns imaginary, $k_z = \pm jk'$, and substituting it in equation (2.22) leads to

$$E_y = E_0 \sin k_x x e^{\pm k' z} e^{j\omega t}\,. \tag{2.24}$$

This represents a wave oscillating with time but decaying exponentially along the waveguide away from the source and which is not able to propagate in the waveguide. The cut-off frequency for the different TE_{nm} modes is given by [6]

$$f_{c,nm} = \frac{c}{2\pi}\sqrt{\left(\frac{n\pi}{w}\right)^2 + \left(\frac{m\pi}{u}\right)^2} \tag{2.25}$$

where c is the velocity of light. For the **W** band with the frequency range of 75 to 110 GHz the inner dimensions of the waveguide are set by the waveguide standard WR-10 [7] to be [mm] $w = 2.54$ and $u = 1.27$. A detailed analysis of the rectangular waveguide can be found for instance in [5] and [6]. The TE_{10} mode in the rectangular waveguide can be represented as the superposition of two *TEM* waves reflected by the walls of the waveguide as shown in *Figure 2.5*.

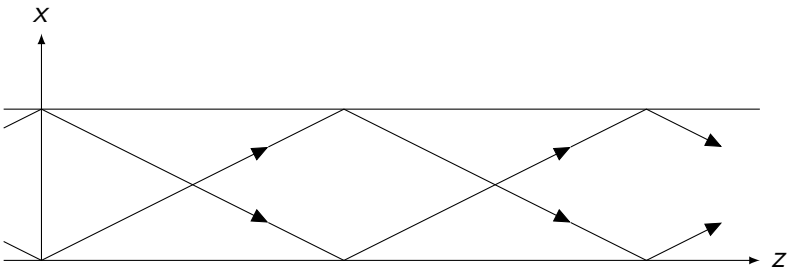

Figure 2.5: *Decomposition of the TE_{10} mode into two plane waves inside a rectangular waveguide [6]*

2.1.3 Dielectric rod waveguides

The dielectric rod waveguide (DRW) is a dielectric waveguide having a rectangular cross-section. Compared to low permittivity dielectric rod waveguides, DRW with high permittivity material have the advantage of smaller dimensions. Thereby, it is easier to manufacture and integrate in systems working at millimeter wave frequencies and also enables transitions to standard rectangular waveguides. Nowadays it is possible to manufacture components with small dimensions with the needed precision [8]. It is therefore desirable to chose high permittivity dielectrics with relative permittivity of 10-15 and a low loss tangent [9].

For the dielectric rod waveguide two families of guided modes exist: the E^y_{pq} modes and the E^x_{pq} modes, with p and q indicating the mode order corresponding to the number of maxima the field distribution has across the structure in the x - and y -direction, respectively. The upper letters ^{x} and ^{y} indicate the strongest component of the electric field [9] in that mode. *Figure 2.7* exemplarily demonstrates the field distributions for the E^y_{11} mode.

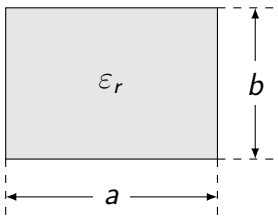

Figure 2.6: *Cross-sectional view of a dielectric rod waveguide with width a and height b having the permittivity ε_r*

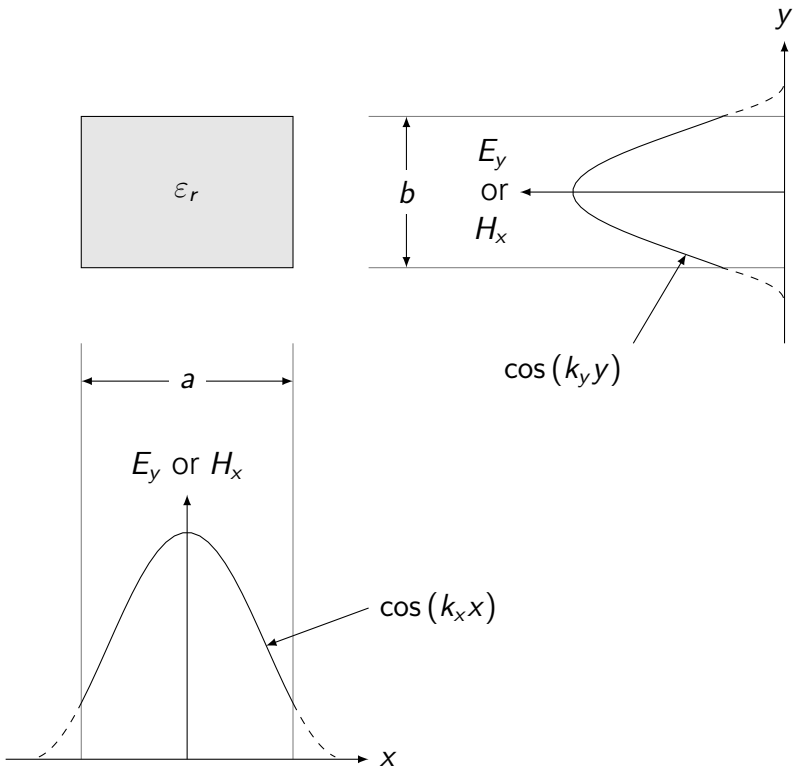

Figure 2.7: *Illustration of the distribution of the field components E_y and H_x for the E_{11}^y dielectric rod waveguide mode [10]*

Table 2.1: Dielectric properties of materials at 140GHz [9]

Material	Si	Diamond	GaAs	Sapphire
Crystal structure	Diamond	Diamond	Zinc blende	Wurtzite
Relative permittivity	$11.6 - 11.8$	5.66	$10.9 - 13.03$	$9.39, 11.56$
$\tan\delta\ [\times 10^{-4}]$	0.03	0.06	$3 - 14$	$1.1 - 1.4$

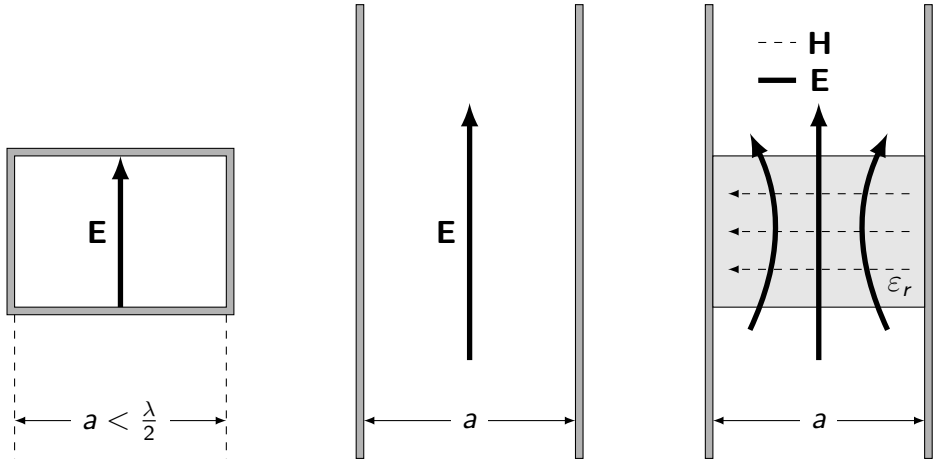

Figure 2.8: *Principle of operation of the NRD guide: (a) Rectangular waveguide working below cutoff, (b) parallel plates waveguide still below cutoff and (c) low-loss LSM_{01} mode electric and magnetic field lines for non-radiating dielectric waveguides [11]*

2.1.4 Non-radiating dielectric waveguides

The non-radiating dielectric waveguide (NRD guide) was first proposed by Yoneyama and Nishida [12] and, since then, has been widely adapted in the millimeter-wave field. It is a low-loss transmission line with a topology similar to the *H*-guide. NRD guide components can be easily employed in monolithic millimeter integrated circuits (MMIC). The main advantage of the NRD guide is the non-radiating behaviour outside of the dielectric strip between the metal plates where the spacing is less than half the free-space wavelength and the cut-off state is reached. However, in the dielectric strip the wave can propagate because the wavelength is shortened and therefore removes the cutoff. The principle of operation is illustrated in 2.8. In most of the cases, the preferred mode of operation is the longitudinal section magnetic (*LSM*) hybrid mode [13], where the magnetic field lines are parallel to the air/dielectric interface compared to the electric ones for *LSE* modes as shown in 2.8c. Therefore the primary LSM_{01} mode has lower conducting and dielectric losses. The wave propagation inside the NRD guide for the LSM_{01} mode is similar to the propagation in the rectangular waveguide, where plane waves propagate in zigzag path through the waveguide [14].

Besides the standard NRD guide shown in *Figure 2.9a*, there also exist a model of an asymmetric NRD guide with a gap between the dielectric rod and

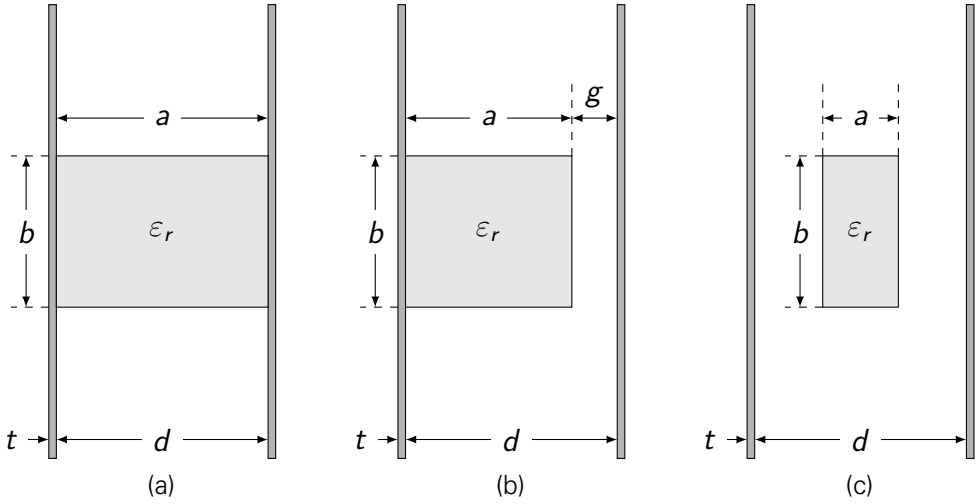

Figure 2.9: *Cross-sectional view of the (a) symmetric NRD guide, (b) asymmetric NRD guide with introduced gap [15] and (c) symmetric NRD guide with a narrow dielectric rod having permittivity ε_r; with b being the height, a the width of the dielectric rod, d the separation between the parallel metal plates and t the thickness of the plates*

one metal plate (*Figure 2.9b*). While manufacturing, this kind of gap can be caused for instance due to bended metal plates. Reaching a certain value, the gap g causes a shift in the phase constant β resulting also in a shift of the guide wavelength λ_g and leakage away from the dielectric rod [15]. The NRD guide is used for various antenna concepts [16] [17].

In this thesis MARCATALI's method is extended for the use with non-radiating waveguides. The primary *LSM* mode of propagation in the NRD guide is similar to the E_{11}^y mode in the DRW, with the assumption that E_y is the main electric field component. Connecting the NRD guide to a standard metal waveguide with a proper transition, the dominant *LSM* mode can be excited by the TE_{10} mode of a standard metal waveguide.

Due to the symmetric geometry of the NRD guide, symmetry planes can be introduced to reduce the complexity in electromagnetic field simulations (*Figure 2.10*). Thus, only one quarter of the model has to be simulated. The boundary conditions for the electric symmetry plane are

$$\mathbf{E}_t = 0 \,, \tag{2.26a}$$

$$\mathbf{H}_n = 0 \,, \tag{2.26b}$$

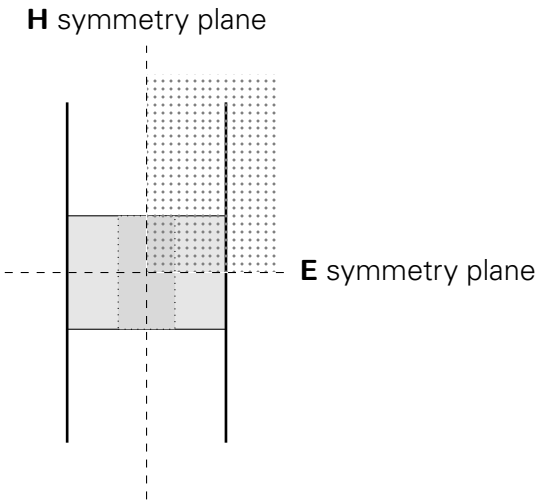

Figure 2.10: *NRD guide symmetry planes*

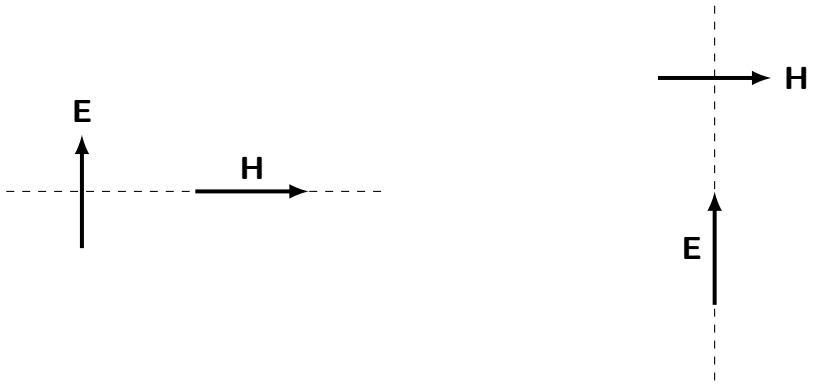

(a) *electric symmetry* (b) *magnetic symmetry*

Figure 2.11: *Symmetry planes*

and for the magnetic symmetry plane

$$\mathbf{E}_n = 0 \,, \tag{2.27a}$$

$$\mathbf{H}_t = 0 \,. \tag{2.27b}$$

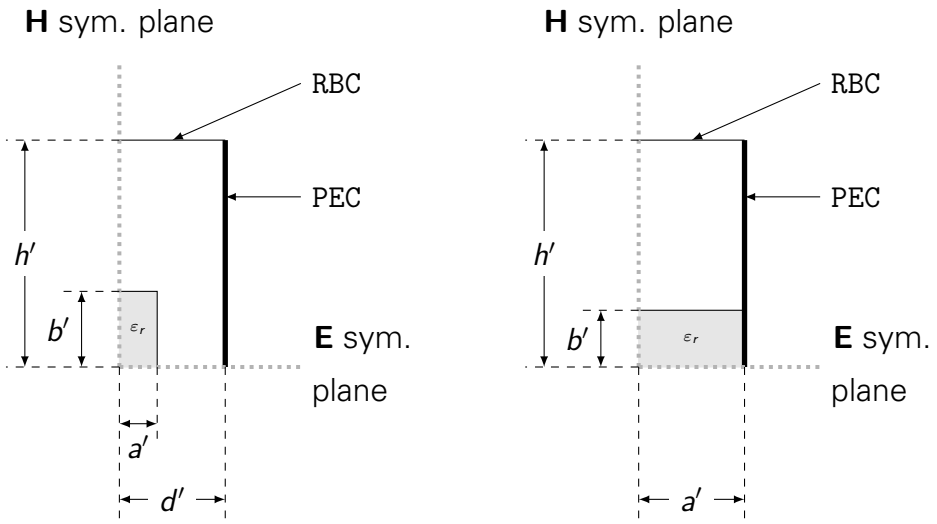

(a) $a < d$ (b) $a = d$

Figure 2.12: *HFSS simulation model cross-sections of the NRD guide using electric and magnetic symmetry planes with* $a' = a/2$, $b' = b/2$, $d' = d/2$ *and* $h' = h/2$.

2.2 NRD guide model

To study the propagation characteristics of the NRD guide a waveguide model was designed and simulated with *Ansoft HFSS*. HFSS is a finite element method solver for electromagnetic structures. The cross-section of the two NRD guide models simulated are shown in *Figure 2.12* on page 15. For the model depicted in *Figure 2.12a* the dielectric rod having a smaller width than the distance of the metal plates $a < d$ was placed symmetrically between the parallel metal plates, whereas *Figure 2.12b* illustrates the classical NRD guide with $a = d$. The metal plates were modeled assigning perfect electric conductors (PEC) for the side wall of the air box and the electric and magnetic symmetry planes as described in Section 2.1.4 were utilized to shorten simulation time. At the top face of the airbox radiation boundary condition (RBC) was assigned. As the dielectric rod silicon with a relative permittivity of $\varepsilon_r = 11.9$ (value used in HFSS) was chosen.

For the non-radiating behaviour of the waveguide the distance of the metal plates has to fullfill the condition $d < \frac{\lambda_{u0}}{2}$ for the upper limiting frequency f_u of the desired frequency range. The upper limiting frequency was set to $f_u = 100$ GHz

and thus

$$d < \frac{\lambda_{u0}}{2} = \frac{c}{2 \cdot f_u} \approx 1.5 \text{ mm} , \tag{2.28}$$

$$d = 1.4 \text{ mm} , \tag{2.29}$$

with c being the speed of light. In theory the limiting frequency for the defined distance would be $f_u|_{d=1.4\text{ mm}} \approx 107.14$ GHz. The dimensions of the silicon rod for the NRD guide shown in *Figure 2.12a* with $a < d$ were derived from [9] with $a = 0.5$ mm and $b = 1$ mm. The height of the metal plates was set to be $h = 3$ mm.

With HFSS port mode simulation the guide wavelength λ_g and the propagation constant k_z were obtained. The dispersion diagrams $k_z/k_0 - f$ for the classical NRD guide with $a = d$ are presented in *Figures 2.13* and *A.1* for different values of the dielectric rod height b. The guide wavelength is shown in *Figure 2.14* on page 18 for in mm $b = 0.5$ and $b = 0.75$ and in *Figure A.2* on page 93 for in mm $b = 0.6$ and $b = 0.7$. It is also possible to derive the propagation constant k_z and the guide wavelength λ_g analytically from the simulation results as described in Appendix D.

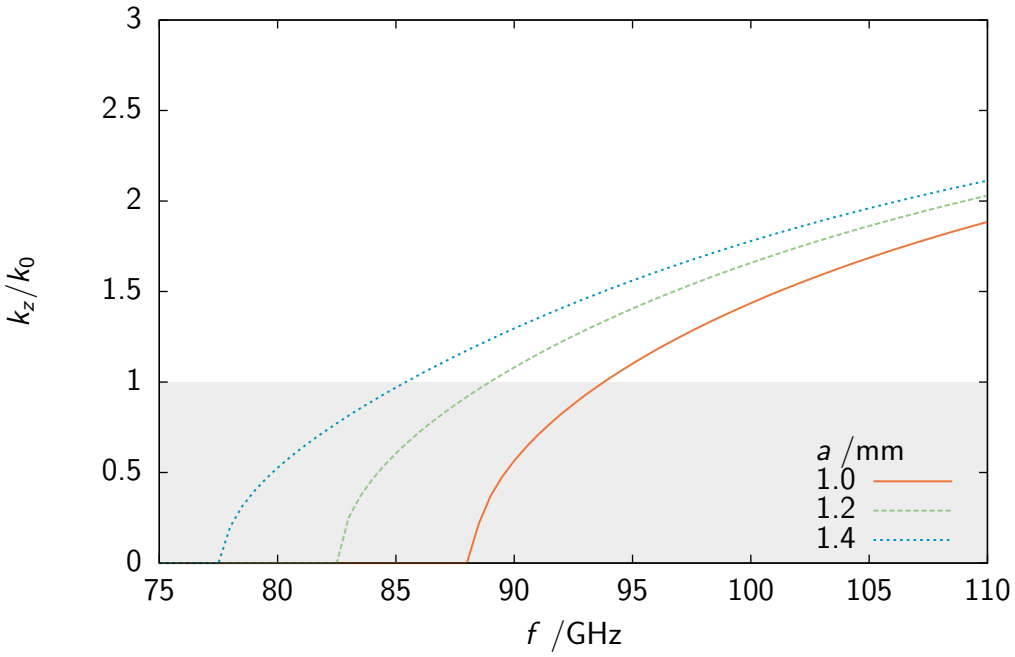

(a) $b = 0.5$ mm

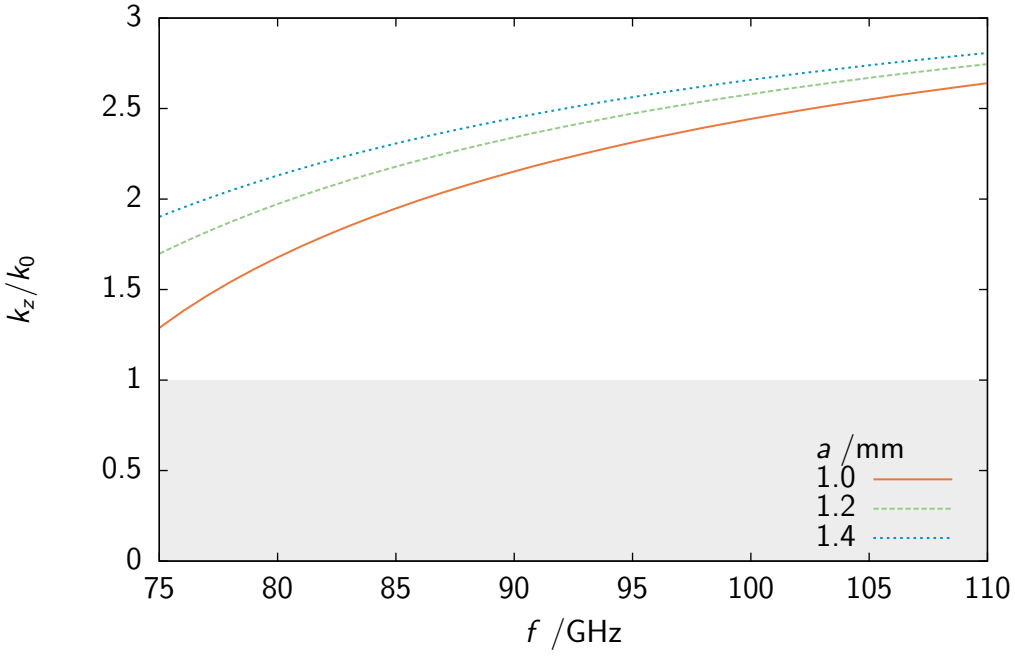

(b) $b = 0.75$ mm

Figure 2.13: *Simulation results of the propagation constant k_z of the classical NRD guide $a = d$*

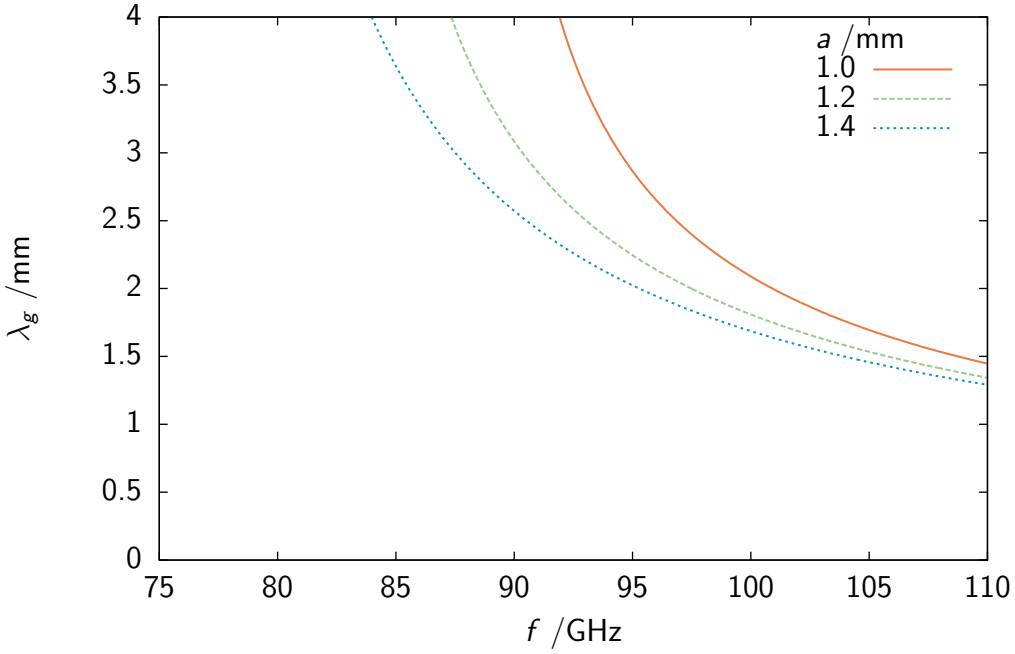

(a) $b = 0.5$ mm

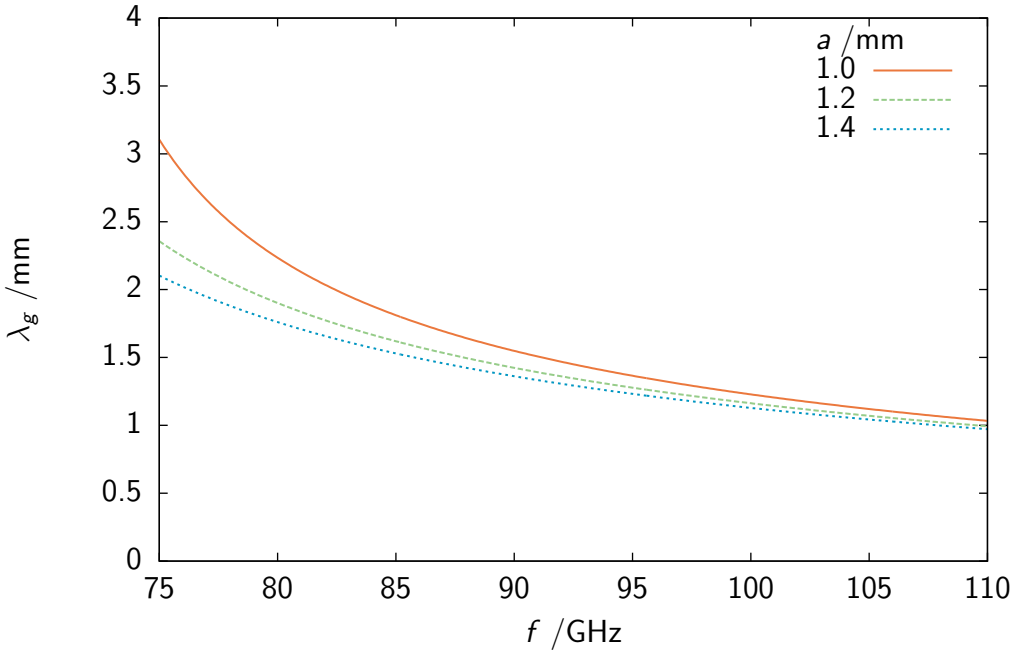

(b) $b = 0.75$ mm

Figure 2.14: *Simulation results of the guide wavelength λ_g of the classical NRD guide $a = d$*

2.3 MARCATILI's method for non-radiating dielectric waveguides

In contrast to circular dielectric waveguides, of which the propagation characteristics can relatively easily be calculated using Bessel functions, the geometry of rectangular shaped dielectric waveguides makes it rather difficult. The reason is, that the field of the modes is diverging in the corners of the waveguide which complicates the design of converging numerical algorithms. An accurate analysis of this problem is discussed by Sudbø [18].

The MARCATILI method is an approximation method which was first presented by Enrico A. J. Marcatili in the *Bell Labs Technical Journal* in 1969 [19]. It can be used to calculate the propagation constant of a rectangular waveguide. Therefore a rectangular waveguide as shown in *Figure 2.15* is modeled, consisting of a core with high refractive index n_1 in the middle, denoted as area I in the model, surrounded by homogenous regions II, III, IV and V with low refrective indices $n_{2..5}$. For the case that the propagation constant is far from the cut-off, the electromagnetic field is mainly distributed in the core and only a small part of its energy spreads to the surrounding regions. The energy distributed in the shaded areas is even less and can therefore be disregarded [20].

As outlined in more detail in Appendix C the electric and magnetic field can be described by longitudinal and transverse components [21]. Using the MAXWELL equations

$$\nabla \times \mathbf{E} = -\mu \frac{\partial \mathbf{H}}{\partial t} = -j\omega\mu\mathbf{H} \tag{2.30a}$$

$$\nabla \times \mathbf{H} = \varepsilon \frac{\partial \mathbf{E}}{\partial t} = j\omega\varepsilon\mathbf{E} \tag{2.30b}$$

The vectors of the electric and the magnetic field can be divided into a longitudinal and a transversal component

$$\mathbf{E} = \mathbf{e}_z E_z + \mathbf{E}_t \tag{2.31a}$$

$$\mathbf{H} = \mathbf{e}_z H_z + \mathbf{H}_t \ . \tag{2.31b}$$

Furthermore the vector differential operator **del**, represented by the greek symbol

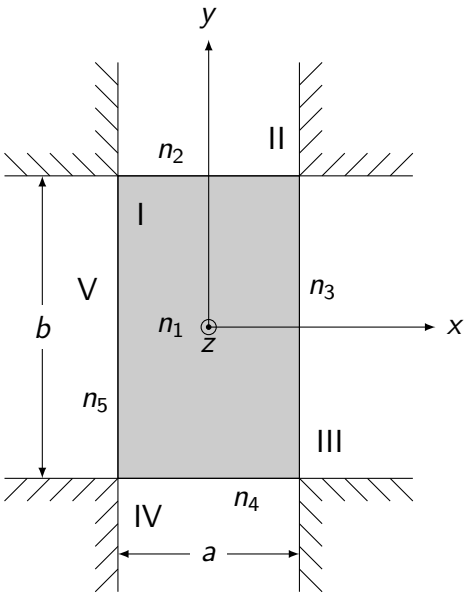

Figure 2.15: *The cross-sectional view of a dielectric rod waveguide in* MARCATILI*'s method*

∇, is expressed in the same manner:

$$\nabla = \mathbf{e}_z \frac{\partial}{\partial z} + \nabla_t \ , \tag{2.32}$$

with

$$\nabla_t = \mathbf{e}_x \frac{\partial}{\partial x} + \mathbf{e}_y \frac{\partial}{\partial y} \ . \tag{2.33}$$

The longitudinal field components traveling along the structure can be expressed as

$$E_z = E_z(x, y) e^{-jk_z z} \ , \tag{2.34a}$$

$$H_z = H_z(x, y) e^{-jk_z z} \ , \tag{2.34b}$$

and thus the derivative in the direction of propagation is

$$\frac{\partial}{\partial z} = -jk_z \ . \tag{2.35}$$

Substituting equations (2.32) and (2.35) into equation (2.30a) leads to

$$\left(\nabla_t + \mathbf{e}_z \frac{\partial}{\partial z}\right) \times (\mathbf{e}_z E_z + \mathbf{E}_t) = -j\omega\mu(\mathbf{e}_z H_z + \mathbf{H}_t) \,, \tag{2.36}$$

$$\nabla_t \times \mathbf{e}_z E_z + \nabla_t \times \mathbf{E}_t + \mathbf{e}_z \frac{\partial}{\partial z} \times \mathbf{E}_t = -j\omega\mu(\mathbf{e}_z H_z + \mathbf{H}_t) \,. \tag{2.37}$$

The z and the transversal components then are given as:

longitudinal:

$$\nabla_t \times \mathbf{E}_t = -j\omega\mu \mathbf{e}_z H_z \,, \tag{2.38a}$$

$$\nabla_t \times \mathbf{H}_t = j\omega\varepsilon \mathbf{e}_z E_z \,. \tag{2.38b}$$

transversal:

$$\nabla_t \times \mathbf{e}_z E_z + \mathbf{e}_z \frac{\partial}{\partial z} \times \mathbf{E}_t = -j\omega\mu \mathbf{H}_t \tag{2.38c}$$

$$\nabla_t \times \mathbf{e}_z H_z + \mathbf{e}_z \frac{\partial}{\partial z} \times \mathbf{H}_t = j\omega\varepsilon \mathbf{E}_t \tag{2.38d}$$

Finally the transversal components of the electric and magnetic field can be expressed by the longitudinal components E_z and H_z as

$$\mathbf{H}_t = \frac{1}{k_z^2 - k^2} \left(jk_z \nabla_t H_z + jk^2 \varepsilon \mathbf{e}_z \times \nabla_t E_z \right) \,, \tag{2.39a}$$

$$\mathbf{E}_t = \frac{1}{k_z^2 - k^2} \left(jk_z \nabla_t E_z - jk^2 \mu \mathbf{e}_z \times \nabla_t H_z \right) \,. \tag{2.39b}$$

After obtaining the transversal components k_x and k_y of the wavenumber k, the propagation constant k_z can be calculated:

$$k_z^2 = k^2 - k_x^2 - k_y^2 \,, \tag{2.40a}$$

$$k_z = \sqrt{k_0^2 \varepsilon_r - k_x^2 - k_y^2} \,. \tag{2.40b}$$

The wavelength of a waveguide mode is given by [21]

$$\lambda_g = \frac{2\pi}{k_z} \,. \tag{2.41}$$

In MARCATILI's method the transversal components is estimated by considering vertical and horizontal dielectric slab waveguides [22].

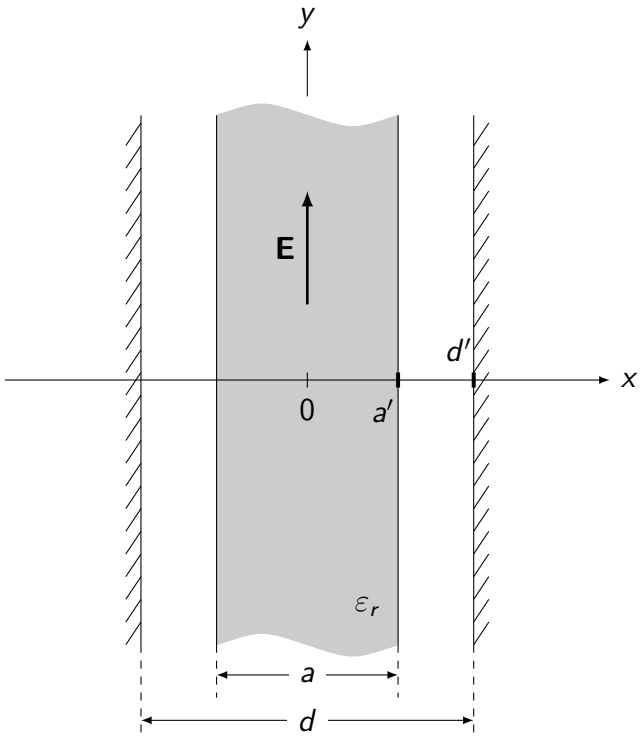

Figure 2.16: *Cross-sectional view of the vertical dielectric slab waveguide for* MARCATILI*'s method embedded between parallel metal plates (refer to* Figure 2.9c*) with width* $a = 2a'$ *and distance of the metal plates* $d = 2d'$

Vertical dielectric slab waveguide embedded between parallel metal plates

To use MARCATILI's method for the chosen NRD guide the assumptions for the vertical dielectric slab waveguide have to be extended. Therefore parallel conducting plates separated by the distance d in which the slab waveguide is embedded symmetrically as shown in *Figure 2.16* are modeled. For the vertical dielectric slab waveguide no dependence of the field components in the vertical y -direction is assumed ($\frac{\partial}{\partial y} = 0$) and equation (2.33) therefore reduces to

$$\nabla_t = \mathbf{e}_x \frac{\partial}{\partial x} \,. \tag{2.42}$$

Now the cross products of equations (2.38a) and (2.38c) are calculated as

$$\nabla_t \times \mathbf{e}_t = \begin{vmatrix} \mathbf{e}_x & \mathbf{e}_y & \mathbf{e}_z \\ \frac{\partial}{\partial x} & 0 & 0 \\ E_x & E_y & 0 \end{vmatrix} = \mathbf{e}_z \frac{\partial E_y}{\partial x} , \tag{2.43a}$$

$$\mathbf{e}_z \times \mathbf{E}_t = \begin{vmatrix} \mathbf{e}_x & \mathbf{e}_y & \mathbf{e}_z \\ 0 & 0 & 1 \\ E_x & E_y & 0 \end{vmatrix} = -\mathbf{e}_x E_y + \mathbf{e}_y E_x , \tag{2.43b}$$

$$\nabla_t \times \mathbf{e}_z = \begin{vmatrix} \mathbf{e}_x & \mathbf{e}_y & \mathbf{e}_z \\ \frac{\partial}{\partial x} & 0 & 0 \\ 0 & 0 & 1 \end{vmatrix} = -\mathbf{e}_y \frac{\partial}{\partial x} , \tag{2.43c}$$

and the components for cartesian coordinates are:

$$\underline{\text{x:}} \quad jk_z E_y = -j\omega\mu H_x , \tag{2.44a}$$

$$\text{y:} \quad jk_z E_x + \frac{\partial E_z}{\partial x} = j\omega\mu H_y , \tag{2.44b}$$

$$\underline{\text{z:}} \quad \frac{\partial E_y}{\partial x} = -j\omega\mu H_z . \tag{2.44c}$$

Using equation (2.30b) the other three equations can be derived similarly:

$$\text{x:} \quad jk_z H_y = j\omega\varepsilon E_x , \tag{2.45a}$$

$$\underline{\text{y:}} \quad -jk_z H_x - \frac{\partial H_z}{\partial x} = j\omega\varepsilon E_y , \tag{2.45b}$$

$$\text{z:} \quad \frac{\partial H_y}{\partial x} = j\omega\mu E_z . \tag{2.45c}$$

It has to be noted that equations (2.44a), (2.44c) and (2.45b) involve only three field components E_y, H_x and H_z, whereas the other three components E_x, H_y and E_z are present in equations (2.44b), (2.45a) and (2.45c). That is, there are two independent sets of equations, corresponding to *TE* (set 1 with $E_z = 0$) and *TM* (set 2 with $H_z = 0$) wave modes. The *TE* modes are selected, as E_y is assumed to be the main electric field component.

From our set of equations for *TE* modes it is possible to express the other two field components H_x and H_z with respect to E_y. Converting equation (2.44a)

delivers

$$H_x = -\frac{k_z}{\omega\mu} E_y \tag{2.46}$$

and rewriting equation (2.44c) gives

$$H_z = -\frac{1}{j\omega\mu} \cdot \frac{\partial E_y}{\partial x} \,. \tag{2.47}$$

It is then assumed that the dominant electric field component E_y is distributed cosinusoidally inside the dielectric slab (refer to *Figure 2.7* on page 11) and decaying exponentially in the air-filled region between the dielectric and the metal plates:

$$E_y = \begin{cases} A \cdot \cos(k_x x) & , |x| < a' \\ B_1 \cdot e^{-\gamma_x x} + B_2 \cdot e^{\gamma_x x} & , |x| > a' \end{cases} \tag{2.48}$$

where k_x and α_x are the wave parameters. Inserting equation (2.48) into equation (2.47) then leads to

$$H_z = \begin{cases} \dfrac{A \cdot k_x}{j\omega\mu} \cdot \sin(k_x x) & , |x| < a' \\ \dfrac{\gamma_x}{j\omega\mu} \cdot (B_1 e^{-\gamma_x x} - B_2 e^{\gamma_x x}) & , |x| > a' \end{cases} \tag{2.49}$$

Furthermore the assumption that the field distribution does not depend on the vertical y -coordinate and thus $k_y = 0$, reduces equation (2.40a) to

$$k^2 = k_x^2 + k_z^2 \,, \tag{2.50}$$

$$k_x^2 = k^2 - k_z^2 \,. \tag{2.51}$$

For the wave propagation in the air-filled region $a' < x < d'$ equation (2.40a) similarly leads to

$$k_0^2 = -\gamma_x^2 + k_z^2 \,, \tag{2.52}$$

$$\gamma_x^2 = k_z^2 - k_0^2 \,. \tag{2.53}$$

Now boundary conditions at the dielectric-air interface and the metal plates can be applied to eliminate the unknowns A, B_1 and B_2.

Boundary condition: $\underline{E_y(d') = 0}$ **(metal plate)**

As the electric field on the surface of a conductor is perpendicular to it, the electric field component E_y tangential to the surface layer has to fullfill the boundary condition $E_y(d') = 0$ at the metal plate and thus equation (2.48) has to be zero for $x = d' > a'$:

$$B_1 e^{-\gamma_x d'} + B_2 e^{\gamma_x d'} = 0 \,. \tag{2.54}$$

$$\tag{2.55}$$

The relation between the unknowns B_1 and B_2 is then given by:

$$B_2 = -B_1 e^{-2\gamma_x d'} \,. \tag{2.56}$$

Inserting equation (2.59) into equation (2.48) leads to

$$E_y = \begin{cases} A \cdot \cos(k_x x) & , |x| < a' \\ B_1 \cdot \left(e^{-\gamma_x x} - e^{\gamma_x (x-2d')}\right) & , |x| > a' \end{cases} \tag{2.57}$$

and equation (2.49) becomes

$$H_z = \begin{cases} \dfrac{A \cdot k_x}{j\omega\mu} \cdot \sin(k_x x) & , |x| < a' \\ \dfrac{B_1 \cdot \gamma_x}{j\omega\mu} \cdot \left(e^{-\gamma_x x} + e^{\gamma_x (x-2d')}\right) & , |x| > a' \end{cases} \tag{2.58}$$

Boundary condition: $\underline{E_y(a' - 0) = E_y(a' + 0)}$ **(dielectric–air interface)**

As described in Section 2.1.1 the tangential electric field component at an interface between two media with $\varepsilon_1 \neq \varepsilon_2$ are equal and thus $E_y|_{x=a'-0}$ inside the dielectric core is equal to $E_y|_{x=a'+0}$ in the air region at the interface: Using equation (2.57) gives

$$A \cdot \cos(k_x a') = B_1 \left(e^{-\gamma_x a'} - e^{\gamma_x (a'-2d')}\right) \,. \tag{2.59}$$

Boundary condition: $\underline{H_z(a-0) = H_z(a+0)}$ **(dielectric–air interface)**

The same boundary condition as for E_y at the dielectric-air interface also applies for the longitudinal magnetic field component H_z and with equation (2.58):

$$\frac{A \cdot k_x}{j\omega\mu} \cdot \sin\left(k_x a'\right) = \frac{B_1 \cdot \gamma_x}{j\omega\mu} \cdot \left(e^{-\gamma_x a'} + e^{\gamma_x (a'-2d')}\right) , \tag{2.60}$$

$$A \cdot k_x \cdot \sin\left(k_x a'\right) = B_1 \cdot \gamma_x \cdot \left(e^{-\gamma_x a'} + e^{\gamma_x (a'-2d')}\right) . \tag{2.61}$$

To eliminate the leftover unknowns A and B_1 equation (2.59) is divided through equation (2.61):

$$\frac{\text{eq. (2.59)}}{\text{eq. (2.61)}}: \qquad \frac{A \cdot \cos\left(k_x a'\right)}{A \cdot k_x \cdot \sin\left(k_x a'\right)} = \frac{B_1 \cdot \left(e^{-\gamma_x a'} - e^{\gamma_x (a'-2d')}\right)}{B_1 \cdot \gamma_x \cdot \left(e^{-\gamma_x a'} + e^{\gamma_x (a'-2d')}\right)} , \tag{2.62}$$

$$\frac{1}{\tan\left(k_x a'\right)} = \frac{k_x}{\gamma_x} \cdot \underbrace{\frac{e^{-\gamma_x a'} - e^{\gamma_x (a'-2d')}}{e^{-\gamma_x a'} + e^{\gamma_x (a'-2d')}}}_{\mathcal{C}} . \tag{2.63}$$

Let us denote

$$\mathcal{C} = \frac{e^{-\gamma_x a'} - e^{\gamma_x (a'-2d')}}{e^{-\gamma_x a'} + e^{\gamma_x (a'-2d')}} . \tag{2.64}$$

Using

$$\tan(\alpha) = \cot(\beta) = \cot\left(\frac{\pi}{2} - \alpha\right) \tag{2.65}$$

equation (2.63) can then be rewritten as:

$$\tan\left(\frac{\pi}{2} - k_x a'\right) = \frac{k_x}{\gamma_x} \cdot \mathcal{C} , \tag{2.66}$$

$$\frac{\pi}{2} - k_x a' = \arctan\left(\frac{k_x}{\gamma_x} \cdot \mathcal{C}\right) - n\pi , \tag{2.67}$$

$$k_x a' = \frac{\pi}{2} - n\pi - \arctan\left(\frac{k_x}{\gamma_x} \cdot \mathcal{C}\right) , \tag{2.68}$$

with $n = 0, \pm 1, \pm 2, \pm 3, \ldots$ Substituting $a' = \frac{a}{2}$ and $d' = \frac{d}{2}$ gives

$$k_x a = p\pi - 2\arctan\left(\frac{k_x}{\gamma_x} \cdot \mathcal{C}\right) , \tag{2.69}$$

with $p = p_e = \pm 1, \pm 3, \pm 5, ...$ and

$$\mathcal{C} = \frac{e^{-\gamma_x \frac{a}{2}} - e^{\gamma_x \left(\frac{a}{2} - d\right)}}{e^{-\gamma_x \frac{a}{2}} + e^{\gamma_x \left(\frac{a}{2} - d\right)}}, \tag{2.70}$$

$$\gamma_x = \sqrt{k_0^2(\varepsilon_r - 1) - k_x^2}\,. \tag{2.71}$$

The parameter $\mathcal{C}$ can written in a more convenient way using the hyperbolic tangent function $\tanh(x) = \dfrac{e^x - e^{-x}}{e^x + e^{-x}}$:

$$\mathcal{C} = \frac{e^{-\gamma_x \frac{a}{2}} - e^{\gamma_x \left(\frac{a}{2} - d\right)}}{e^{-\gamma_x \frac{a}{2}} + e^{\gamma_x \left(\frac{a}{2} - d\right)}} \cdot \frac{e^{\gamma_x \frac{d}{2}}}{e^{\gamma_x \frac{d}{2}}} = \frac{e^{-\frac{\gamma_x}{2}(a-d)} - e^{\frac{\gamma_x}{2}(a-d)}}{e^{-\frac{\gamma_x}{2}(a-d)} + e^{\frac{\gamma_x}{2}(a-d)}}, \tag{2.72}$$

$$\mathcal{C} = \tanh\left(\frac{\gamma_x}{2}(d-a)\right). \tag{2.73}$$

For now H_z was assumed to be distributed sinusoidally in the vertical dielectric slab waveguide. However, if a cosinusoidal distribution is considered, a phase difference of $\frac{\pi}{2}$ is added to equation (2.49) due to that

$$\cos(k_x x) = \cos(-k_x x) = \sin\left(k_x x + \frac{\pi}{2}\right). \tag{2.74}$$

and after similar calculations obtain:

$$k_x a' = -n\pi - \arctan\left(\frac{k_x}{\gamma_x} \cdot \mathcal{C}\right), \tag{2.75}$$

with $n = 0, \pm 1, \pm 2, \pm 3, ...$ Substituting $a' = \frac{a}{2}$ the parameter p of the transcentenal equations in that case is $p = p_o = 0, \pm 2, \pm 4, ...$ Only positive propagation parameters are considered, therefore the minus signs are omitted. Now the transcendetal equations for even and odd modes are merged and the parameter p becomes

$$p = p_e + p_o = 1, 2, ... \tag{2.76}$$

($p = 0$ is not considered as the right part of equation (2.77) will become negative in that case). The transcendental equation representing the solution for the

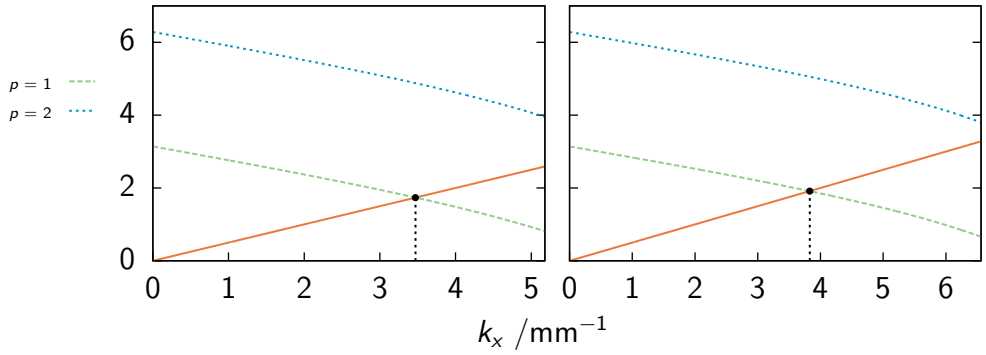

(a) $f_1 = 75$ GHz (b) $f_2 = 95$ GHz

Figure 2.17: *Graphical method to obtain the solutions for the transcendental equation* (2.68) *for* k_x *with dimensions in* mm $a = 0.5$, $b = 1$ *and* $d = 1.4$*; limited by* $k_{xl} = k_0\sqrt{\varepsilon_r - 1}$ *, with* $k_{xl|75\text{GHz}} = 5.19\ \text{mm}^{-1}$ *and* $k_{xl|95\text{GHz}} = 6.57\ \text{mm}^{-1}$

wavenumber component k_x of the NRD guide then is:

$$k_x a = p\pi - 2\arctan\left(\frac{k_x}{\gamma_x}\cdot\mathcal{C}\right) . \tag{2.77}$$

For the special case $a = d$ – depicting the classical NRD guide as shown in *Figure 2.9a* on page 13 – the coefficient $\mathcal{C}$ becomes zero and therefore equation (2.77) simplifies to the well known equation

$$k_x = \frac{p\pi}{a} . \tag{2.78}$$

In *Figure 2.17* the graphical procedure to detect the solution of the transcendental equation (2.77) is revealed exemplarily for $f_1 = 75$ GHz and $f_2 = 95$ GHz. It is shown that for the chosen parameters only the mode for $p = 1$ is supported for these two frequencies, and for the second mode $p = 2$ there is no intersection and thus no solution.

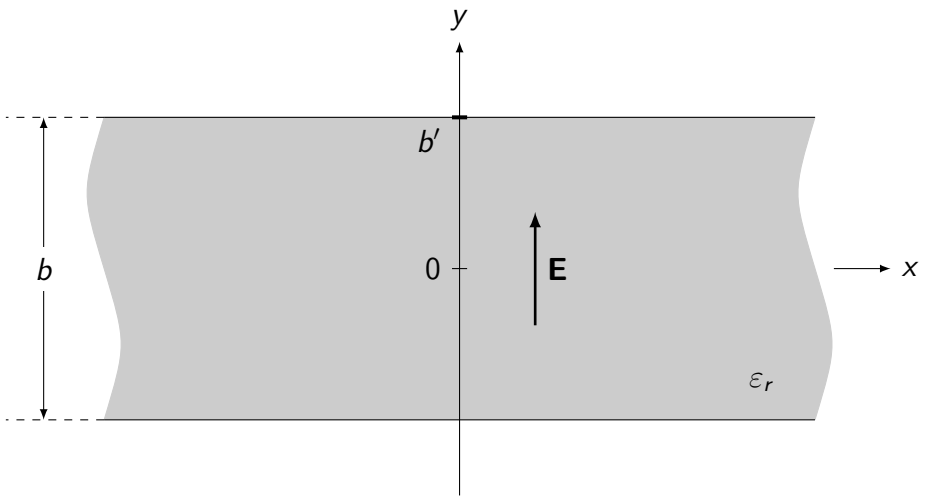

Figure 2.18: *Cross-section of the horizontal dielectric slab waveguide for* MARCATILI*'s method with thickness b*

Horizontal dielectric slab waveguide

To determine k_y, a dielectric slab waveguide stretched infinitely in the horizontal dimension is considered (*Figure 2.18*). In that case the field components are not dependent of the x -direction, $\frac{\partial}{\partial x} = 0$, and equation (2.33) then simplifies to

$$\nabla_t = \mathbf{e}_y \frac{\partial}{\partial y} \,. \tag{2.79}$$

Now the cross products of equations (2.38a) and (2.38c) will be:

$$\nabla_t \times \mathbf{e}_t = \begin{vmatrix} \mathbf{e}_x & \mathbf{e}_y & \mathbf{e}_z \\ 0 & \frac{\partial}{\partial y} & 0 \\ E_x & E_y & 0 \end{vmatrix} = -\mathbf{e}_z \frac{\partial E_x}{\partial y} \,, \tag{2.80a}$$

$$\mathbf{e}_z \times \mathbf{E}_t = \begin{vmatrix} \mathbf{e}_x & \mathbf{e}_y & \mathbf{e}_z \\ 0 & 0 & 1 \\ E_x & E_y & 0 \end{vmatrix} = -\mathbf{e}_x E_y + \mathbf{e}_y E_x \,, \tag{2.80b}$$

$$\nabla_t \times \mathbf{e}_z = \begin{vmatrix} \mathbf{e}_x & \mathbf{e}_y & \mathbf{e}_z \\ 0 & \frac{\partial}{\partial y} & 0 \\ 0 & 0 & 1 \end{vmatrix} = \mathbf{e}_x \frac{\partial}{\partial y} \,, \tag{2.80c}$$

with which the equations for the three cartesian coordinates are given as:

$$\underline{\text{x:}} \quad jk_z E_y + \frac{\partial E_z}{\partial y} = -j\omega\mu H_x \ , \tag{2.81a}$$

$$\text{y:} \quad jk_z E_x = j\omega\mu H_y \ , \tag{2.81b}$$

$$\text{z:} \quad \frac{\partial E_x}{\partial y} = j\omega\mu H_z \ . \tag{2.81c}$$

Using equation (2.30b) the other three equations are derived similarly:

$$\text{x:} \quad jk_z H_y + \frac{\partial H_z}{\partial y} = j\omega\varepsilon E_x \ , \tag{2.82a}$$

$$\underline{\text{y:}} \quad jk_z H_x = -j\omega\varepsilon E_y \ , \tag{2.82b}$$

$$\underline{\text{z:}} \quad \frac{\partial H_x}{\partial y} = -j\omega\varepsilon E_z \ . \tag{2.82c}$$

Again equations (2.81a), (2.82b) and (2.82c) involve only the three field components E_y, E_z and H_x corresponding to the set of equations for *TM* wave modes with $H_z = 0$ and equations (2.81b), (2.81c) and (2.82a) forms the set of equations for *TE* wave modes with $E_z = 0$ and E_x, H_y and H_z present. As E_y is assumed to be the main component *TM* modes are chosen and E_z and H_x are expressed through E_y.

From equation (2.82b) H_x is written as

$$H_x = -\frac{\omega\varepsilon}{jk_z} \cdot E_y \ , \tag{2.83}$$

and substituting H_x in equation (2.82c) with equation (2.83) E_z is expressed through E_y:

$$E_z = \frac{1}{k_z} \cdot \frac{\partial E_y}{\partial y} \ . \tag{2.84}$$

As for the vertical dielectric slab waveguide, it is again assumed that the E_y component is distributed cosinusoidally in the dielectric $|y| < b'$, whereas it decays

exponentially outside the dielectric $|y| > b'$:

$$E_y = \begin{cases} A \cdot \cos(k_y y) & , |y| < b' \\ B \cdot e^{-\gamma_y y} & , |y| > b' \end{cases} \tag{2.85}$$

where k_y and α_y are the wave parameters. Inserting equation (2.85) into equations (2.83) and (2.84) gives

$$H_x = \begin{cases} -\dfrac{\omega\varepsilon}{jk_z} \cdot A \cdot \cos(k_y y) & , |y| < b' \\ -\dfrac{\omega\varepsilon}{jk_z} \cdot B \cdot e^{-\gamma_y y} & , |y| > b' \end{cases} \tag{2.86}$$

and

$$E_z = \begin{cases} \dfrac{1}{k_z} \cdot A \cdot k_y \cdot \sin(k_y y) & , |y| < b' \\ \dfrac{1}{k_z} \cdot B \cdot \gamma_y \cdot e^{-\gamma_y y} & , |y| > b' \end{cases} \tag{2.87}$$

Assuming no dependence of the field distribution on the vertical x -coordinate and thus $k_x = 0$ in the dielectric $|y| < b'$, equation (2.40a) simplifies to

$$k^2 = k_y^2 + k_z^2 \,, \tag{2.88}$$

$$k_y^2 = k^2 - k_z^2 \,, \tag{2.89}$$

whereas for the wave propagation in the air-filled region $|y| > b'$ it leads to

$$k_0^2 = -\gamma_y^2 + k_z^2 \,, \tag{2.90}$$

$$\gamma_y^2 = k_z^2 - k_0^2 \,. \tag{2.91}$$

Now boundary conditions at the dielectric–air interface for the tangential field components E_z and H_x to eleminate the unknowns A and B can be applied.

Boundary condition: $\underline{H_x(b'-0) = H_x(b'+0)}$ **(dielectric–air interface)**

Similarly to the dielectric-air interface for the vertical dielectric slab waveguide, again boundary conditions for the tangential magnetic field component H_x approaching from both sides of the interface are applied:

$$-\frac{\omega\varepsilon_r\varepsilon_0}{k_z}\cdot A\cdot\cos\left(k_y b'\right) = -\frac{\omega\varepsilon_0}{k_z}\cdot B\cdot e^{-\gamma_y b'}\ , \tag{2.92}$$

$$\varepsilon_r\cdot A\cdot\cos\left(k_y b'\right) = B\cdot e^{-\gamma_y b'}\ . \tag{2.93}$$

Boundary condition: $\underline{E_z(b'-0) = E_z(b'+0)}$ **(dielectric–air interface)**

The same boundary condition again is applied to the tangential electric field component E_z at the dielectric-air interface:

$$-\frac{1}{k_z}\cdot A\cdot k_y\cdot\sin\left(k_y b'\right) = -\frac{1}{k_z}\cdot B\cdot\gamma_y e^{-\gamma_y b'}\ , \tag{2.94}$$

$$A\cdot k_y\cdot\sin\left(k_y b'\right) = \gamma_y\cdot B\cdot e^{-\gamma_y b'}\ . \tag{2.95}$$

To eliminate the unknowns A and B equation (2.93) is divided through equation (2.95):

$$\frac{\text{eq. (2.93)}}{\text{eq. (2.95)}}: \qquad \frac{\varepsilon_r\cdot A\cdot\cos\left(k_y b'\right)}{A\cdot k_y\cdot\sin\left(k_y b'\right)} = \frac{B\cdot e^{-\gamma_y b'}}{\gamma_y\cdot\varepsilon_r\cdot B\cdot e^{-\gamma_y b'}}\ , \tag{2.96}$$

$$\frac{1}{\tan\left(k_y b'\right)} = \frac{k_y}{\gamma_y\varepsilon_r}\ , \tag{2.97}$$

and using equation (2.64) the transcendental equation for the wavenumber component k_y is affiliated:

$$\tan\left(\frac{\pi}{2} - k_y b'\right) = \frac{k_y}{\gamma_y\varepsilon_r}\ , \tag{2.98}$$

$$\frac{\pi}{2} - k_y b' = \arctan\left(\frac{k_y}{\gamma_y\varepsilon_r}\right) + n\pi\ , \tag{2.99}$$

$$k_y b' = \frac{\pi}{2} - n\pi - \arctan\left(\frac{k_y}{\gamma_y\varepsilon_r}\right)\ , \tag{2.100}$$

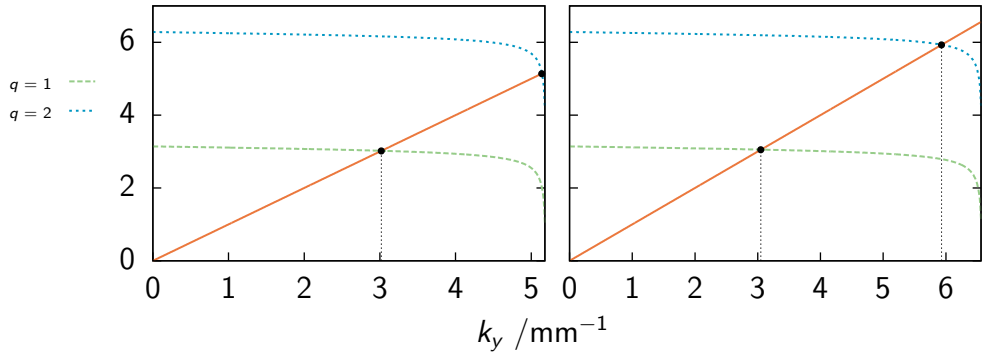

(a) $f_1 = 75$ GHz (b) $f_2 = 95$ GHz

Figure 2.19: *Graphical method to obtain the solutions for the transcendental equation (2.101) for k_y with dimensions in* mm *$a = 0.5$, $b = 1$ and $d = 1.4$; limited by $k_{yl} = k_0\sqrt{\varepsilon_r - 1}$, with $k_{yl|75\text{GHz}} = 5.19$ mm^{-1} and $k_{yl|95\text{GHz}} = 6.57$ mm^{-1}*

with $n = 0, \pm1, \pm2, \pm3, \ldots$ Substituting $b' = \frac{b}{2}$ gives

$$k_y b = q\pi - 2\arctan\left(\frac{k_y}{\gamma_y \varepsilon_r}\right) \tag{2.101}$$

with $q = \pm1, \pm3, \pm5, \ldots$. Similiarly to the transcendental equation for the wavenumber component k_x, the parameter q of equation (2.101) is assembled by adding the even and odd mode parameters:

$$q = q_e + q_o \; . \tag{2.102}$$

Propagation constant k_z

Now having obtained both k_x and k_y for a given frequency f_0 (with the wavenumber in free space k_0) with $p = q = 1$ for the E_{11}^y mode, the propagation constant k_z is then calculated by

$$k_z = \sqrt{k_0^2 \varepsilon_r - k_x^2 - k_y^2} \; . \tag{2.103}$$

In order for the wave to propagate along the structure in the z -direction, k_z has to be real, otherwise the wave will decay exponentially (called *evanescent mode*

[21]). This puts limitations to the dimensions of the NRD guide which control the wavenumber components k_x and k_y for a given frequency and therefore dictates the cut-off. The cut-off wavenumber is derived from equation (2.103) for $k_z = 0$:

$$k_c^2 = k_{c0}^2 \varepsilon_r = k_x^2 + k_y^2 \ . \tag{2.104}$$

The propagation constant k_z can be calculated quite easily with a numerical computing environment like *MATLAB* or *GNU Octave*. The `m` -file calculating the propagation constant for the NRD guide taking the dimensions a, b and d as parameters is printed in Listing B.1 on page 115. *Figures 2.20* and *2.21* display the dispersion diagram $k_z/k_0 - f$ and the guide wavelength $\lambda_g - f$ for a dielectric rod with dimensions in mm $a = 0.5$ and $b = 1$ for several values of the plate distance d. For the chosen dielectric rod it is shown that the NRD guide operates in the slow wave region with $k_z > k_0$ in the depicted frequency range from 75 to 110 GHz unless the metal plates are placed fairly close to the dielectric rod (compare the red line for $d = 0.75$ mm in *Figure 2.20* with $a = 0.5$ mm) and the NRD guide enters the fast wave region for lower frequencies, near to the cut-off. In that case leakage away from the dielectric rod occurs as described in [15]. Placing the metal plates farther apart reduces the impact of the plates on the electric field and the NRD guide approaches the characteristics of the DRW, where $d \gg a$.

The dispersion characteristics for $b = 0.6$ mm and $b = 0.7$ mm are illustrated in *Figures A.5* and *A.6* on pages 96 and 97. It can be seen that the cut-off frequency is decreasing with increasing dielectric rod width b ($a = d = const.$).

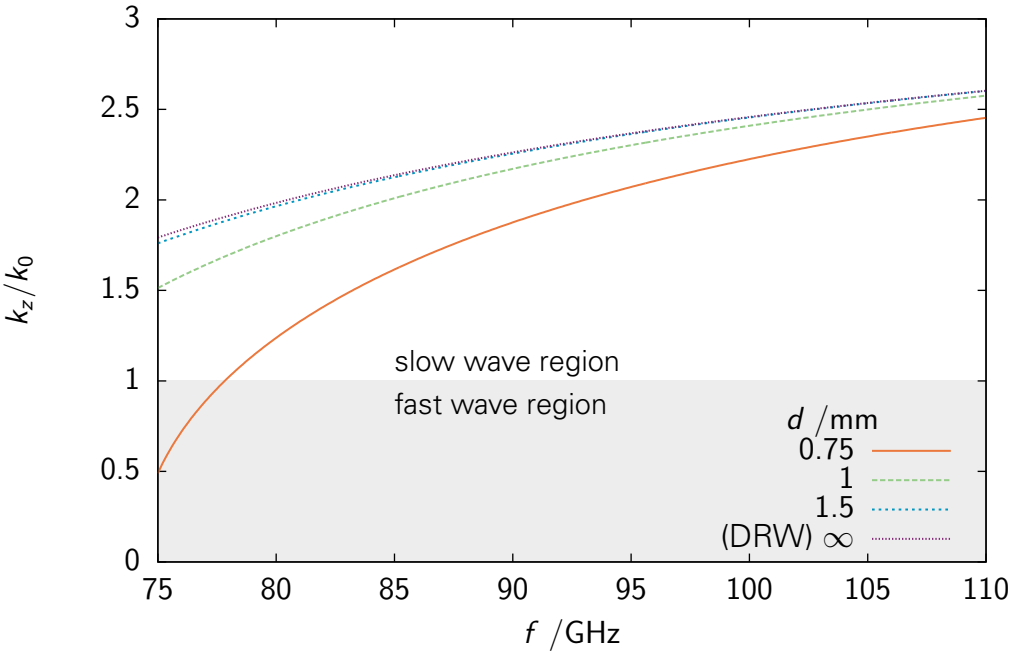

Figure 2.20: *Dispersion diagram $k_z/k_0 - f$ for the NRD guide using the developed* MARCATILI *method with dimensions in* mm *$a = 0.5$ and $b = 1$ for different values for the distance between the metal plates d and for the open dielectric rod waveguide (DRW) with $d \gg a$*

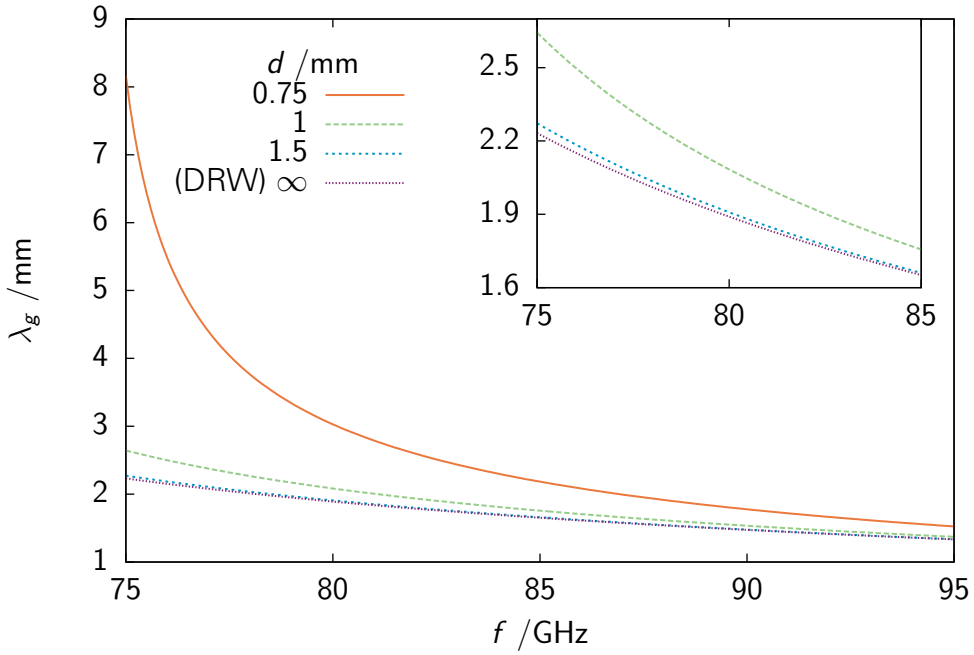

Figure 2.21: *Guide wavelength of the NRD guide using the developed* MARCATILI *method with dimensions in* mm *$a = 0.5$ and $b = 1$ for different values for the distance between the metal plates d and for the open dielectric rod waveguide (DRW) with $d \gg a$*

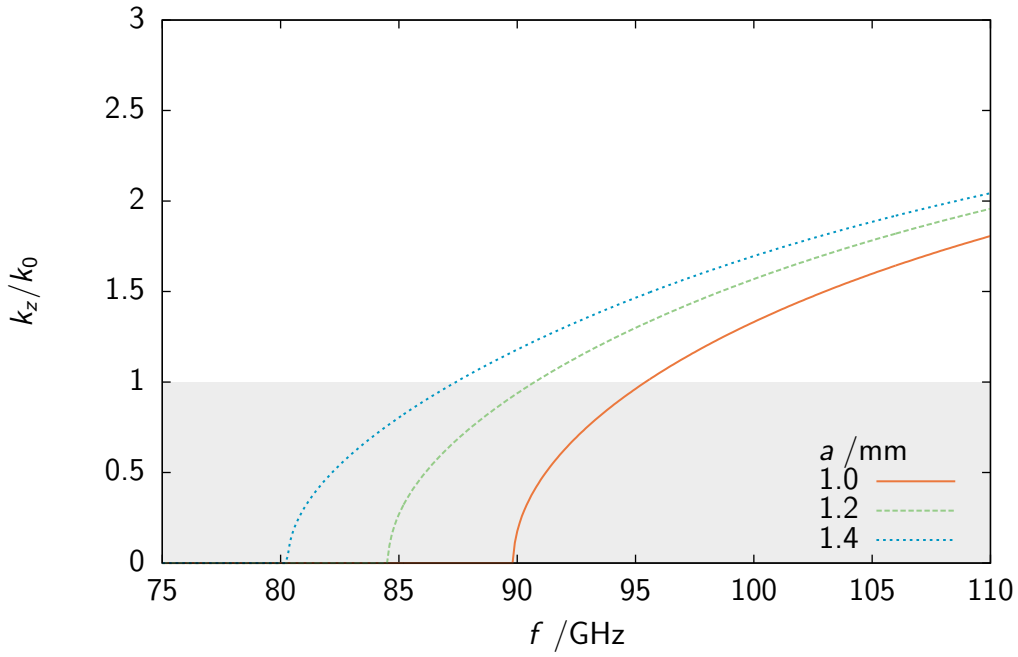

(a) $b = 0.5$ mm

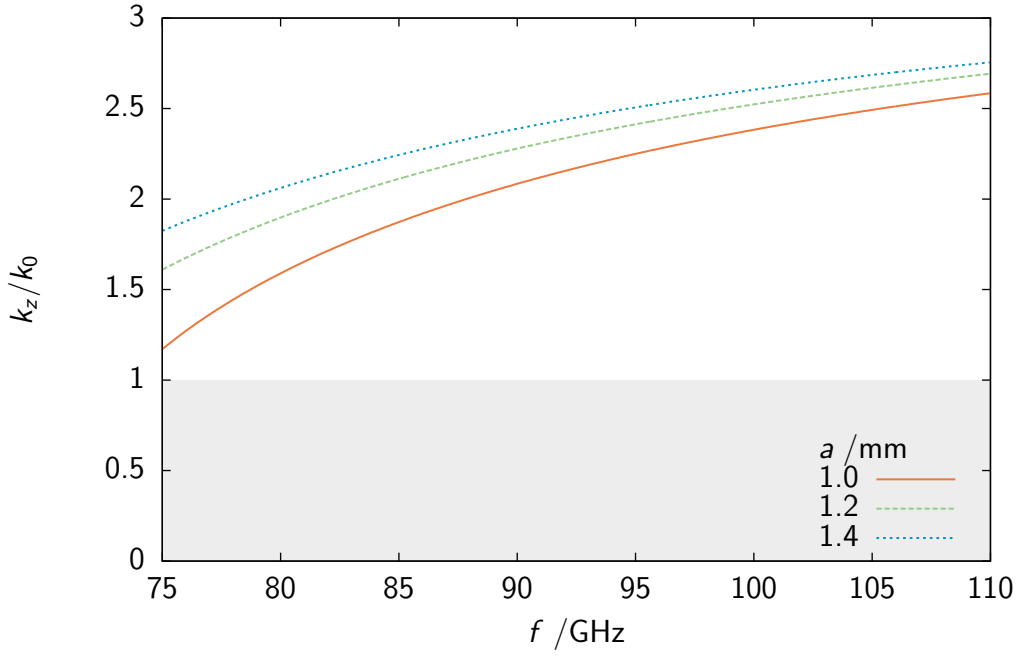

(b) $b = 0.75$ mm

Figure 2.22: *Calculated dispersion diagram $k_z/k_0 - f$ of the classical NRD guide with $a = d$*

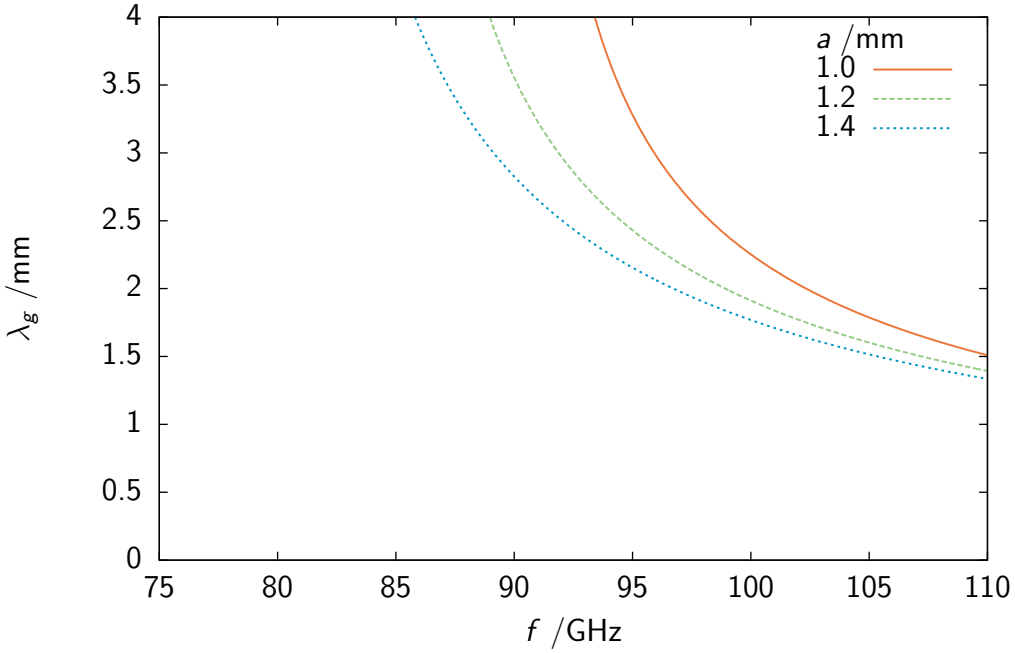

(a) $b = 0.5$ mm

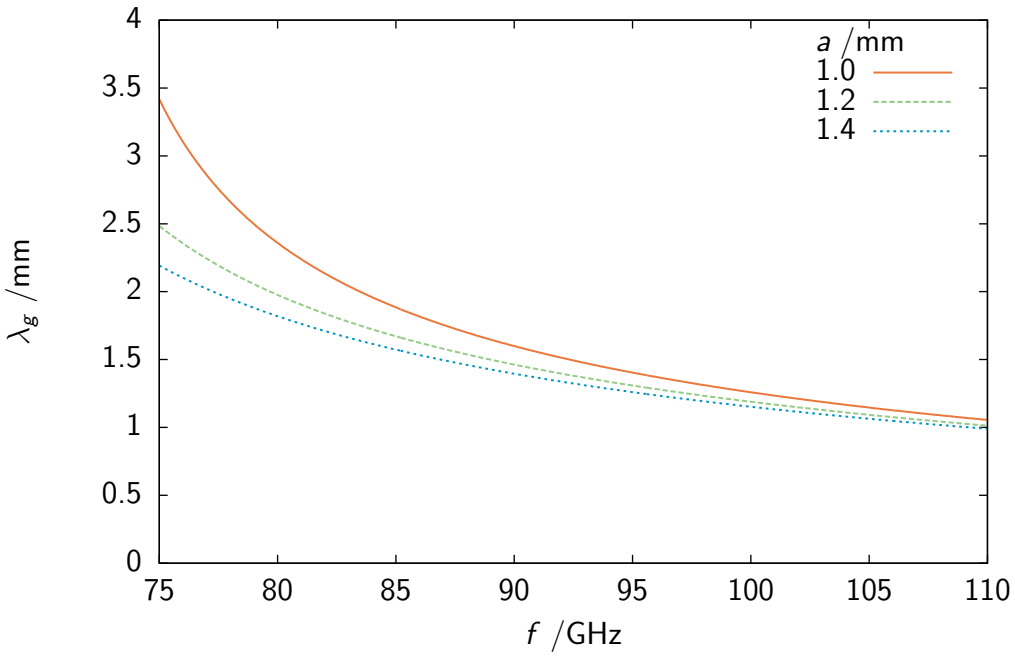

(b) $b = 0.75$ mm

Figure 2.23: *Calculated guide wavelength λ_g of the classical NRD guide with $a = d$*

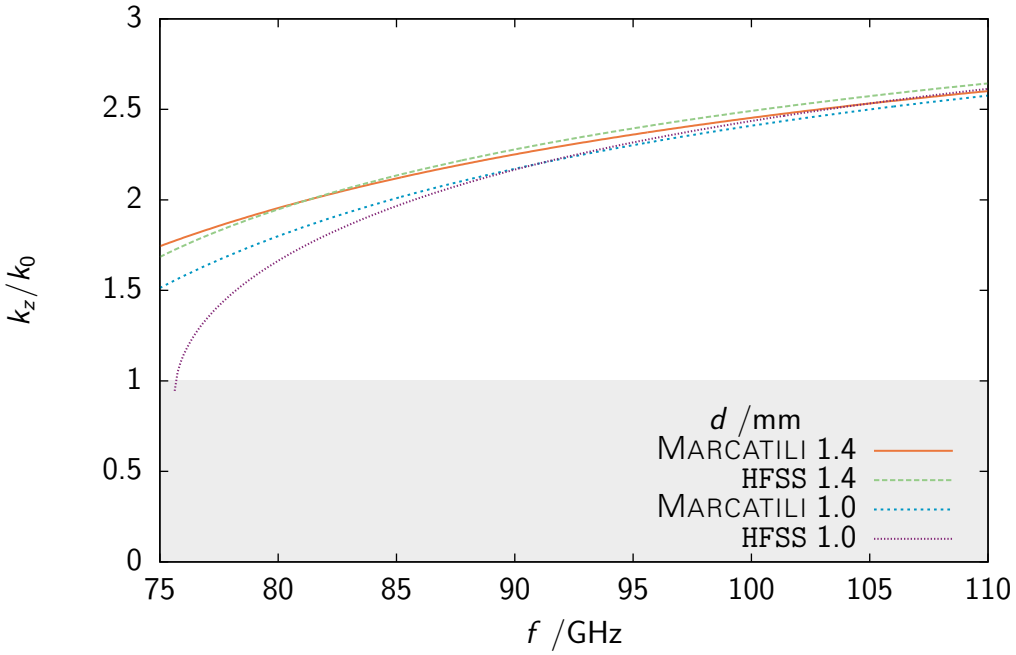

Figure 2.24: *Comparison of the calculated and the simulated results for the propagation constant of the NRD guide with dimensions in* mm $a = 0.5$, $b = 1$ *and varying plate distance* d

Comparison of the numerical simulation results and MARCATILI's approximation method

In *Figure 2.24* the simulated and calculated results of the normalized propagation constant k_z/k_0 are compared for the NRD guide with a narrow dielectric rod $a = 0.5$ mm $< d$. The MARCATILI results are lower than the simulated ones, which are considered to be numerically correct. This is because the field distributed in the shaded corner regions was not taken into account. For frequencies far higher than the cut-off this is not as prominent as for frequencies close to the cut-off [23]. There are approaches for dielectric waveguides to improve the accuracy of MARCATILI's method, such as several perturbation methods [23]. Kumar et al. for instance proposed an advancement to MARCATILI's method by also taking the fields in the shaded areas into account [24]. For our results the calculated values are higher than the simulated ones for higher frequencies. This can be due to convergence problems within the HFSS simulations.

For the classical NRD guide with $a = d$ where no neglected shaded areas as for the DRW and the NRD guide with a narrow dielectric rod exists, the compared values presented in *Figures 2.25* and *2.26* are below the simulated results,

as anticipated. This effect is also more prominent for frequencies close to the cut-off, whereas it's diminishing but not disappearing for higher frequencies. The reason for that is that it is assumed that E_y is the main field component in the *LSM* mode of the NRD guide and the E_x component was not taken into account. Even so MARCATILI's method is a suitable method to approximate the propagation constant, especially for higher frequencies far from the cut-off and if possible inaccuracies of the simulation results are considered. The comparison of the calculated and simulated attenuation constant α shown in *Figure 2.27* reveals that the developed extended MARCATILI method is not suitable to approximate the attenuation constant.

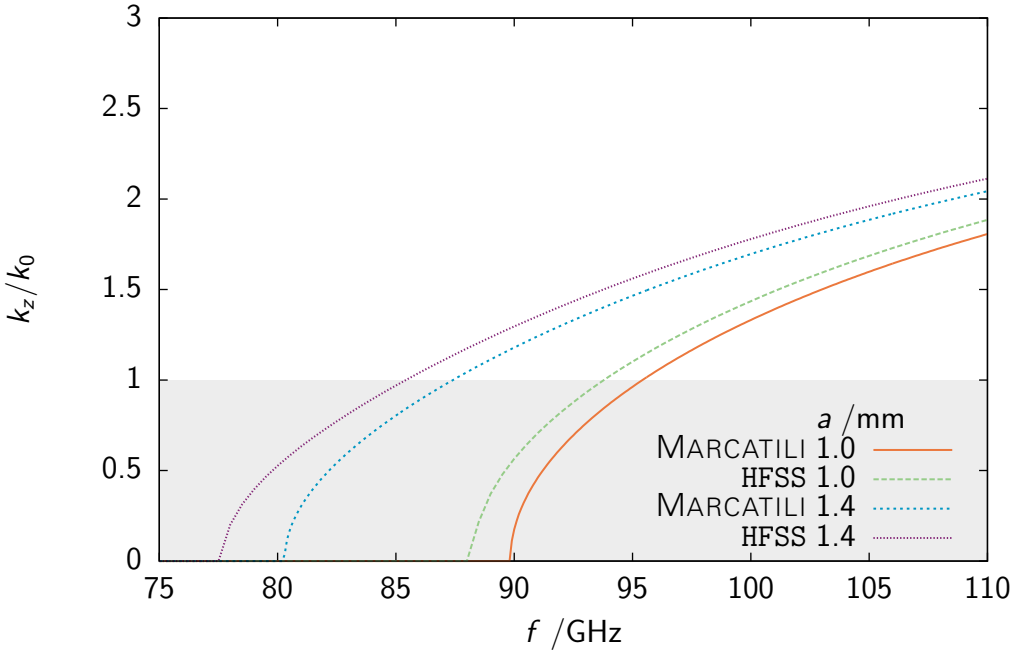

(a) $b = 0.5$ mm

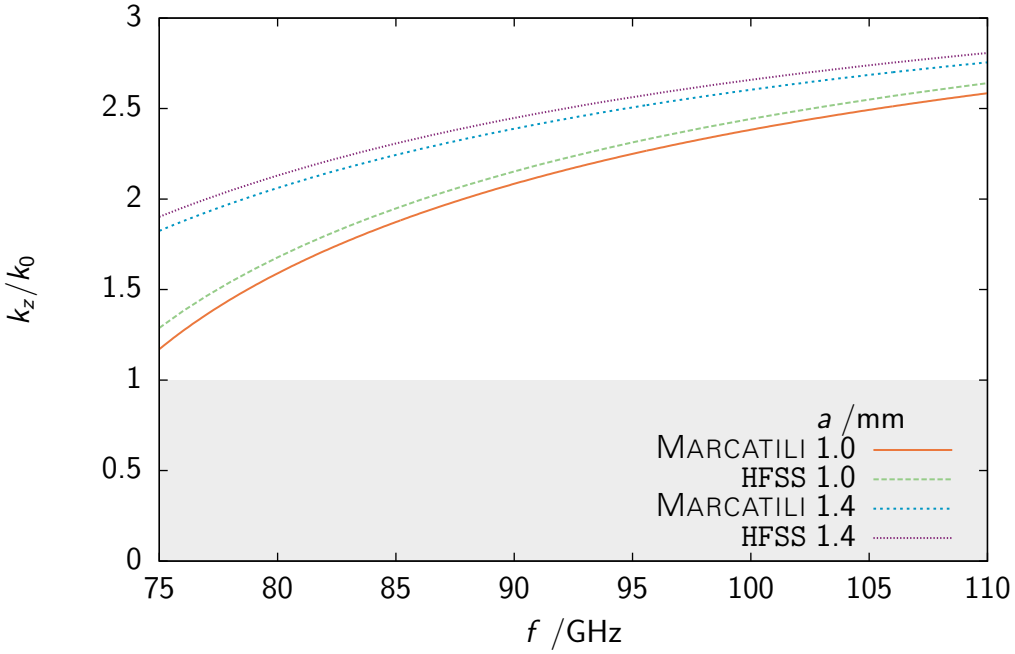

(b) $b = 0.75$ mm

Figure 2.25: *Comparison of the calculated and the simulated dispersion characteristic* $k_z/k_0 - f$

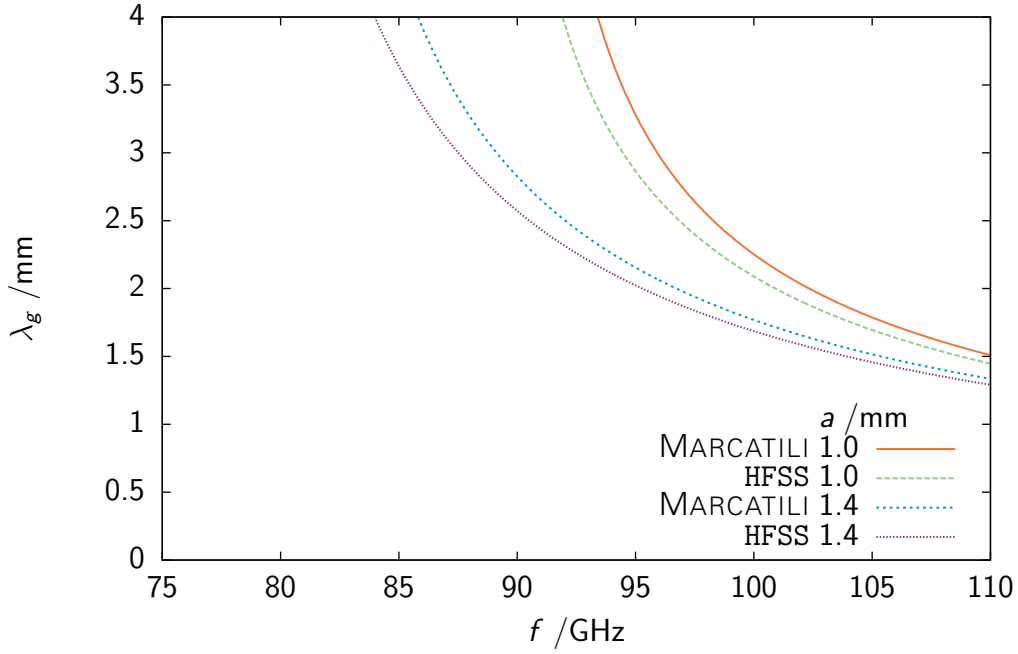

(a) $b = 0.5$ mm

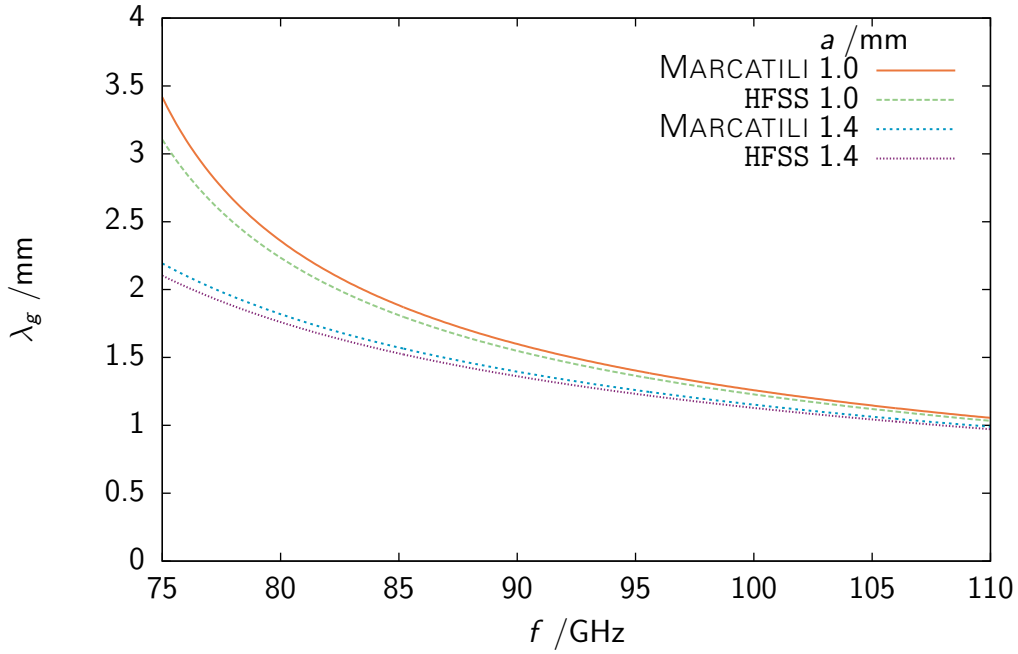

(b) $b = 0.75$ mm

Figure 2.26: *Comparison of the calculated and the simulated dispersion characteristic* $\lambda_g - f$

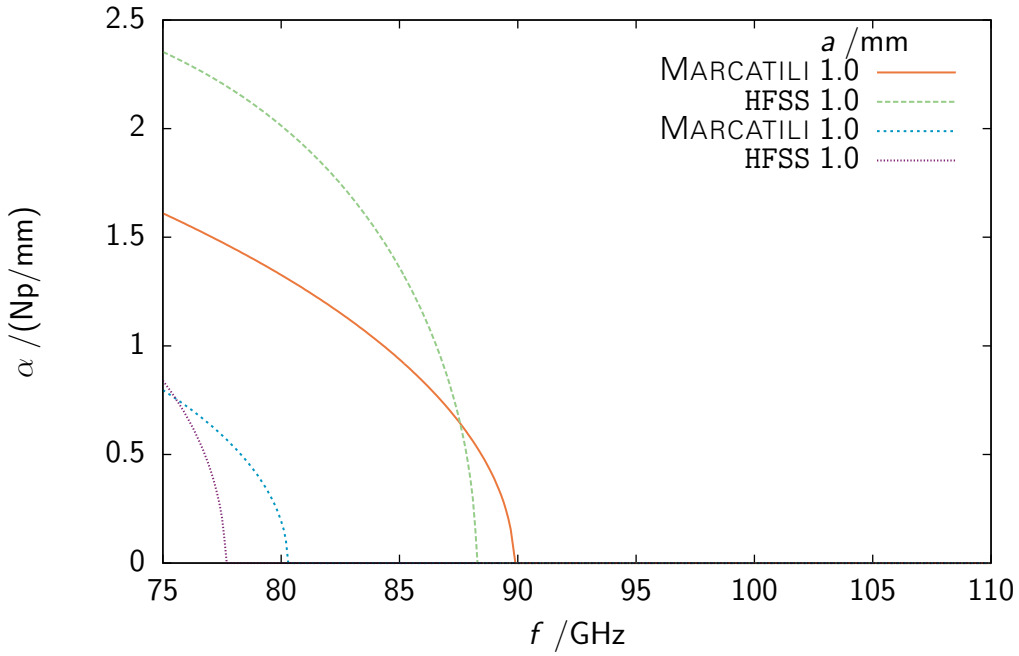

Figure 2.27: *Comparison of the calculated and the simulated attenuation constant α for the classic NRD guide with $a = d$ and $b = 0.5$ mm*

2.4 Standard metal waveguide to NRD guide transition

In order to connect a non-radiating dielectric waveguide to a standard metal waveguide, a suitable transition is needed. This transition has to show low reflection and good transmission characteristics and should be easy to manufacture. In [9] a standard metal waveguide to dielectric rod waveguide transition was developed. Based on that transition, a standard metal waveguide to NRD guide transition is presented in this Section.

As described in detail in Section 2.1.4, the desired mode of propagation for the NRD guide is the low-loss *LSM* mode with the magnetic field lines perpendicular to the parallel metal plates shown in *Figure 2.8c* on page 12. This mode can be excited by the TE_{10} mode of a rectangular waveguide. There are different approaches towards transitions from rectangular waveguide to the NRD guide, such as the rectangular waveguide to image NRD guide presented by Hattori et al. (2001) [25]. Malherbe et al. (2005) developed a transition from a rectangular to nonradiating dielectric waveguide [26]. In this Section an easy transition for the W band is studied.

2.4.1 Design

Four different kinds of transitions were studied (illustrated in *Figure 2.28*):

(I) the pyramidal transition from the standard metal waveguide sidewalls to the NRD guide sidewalls,

(II) the opening of the sidewalls of the standard metal waveguide towards the NRD guide parallel plates,

(III) the direct connection of the two waveguides with shield plates closing the parts of the aperture of the standard metal waveguide outside of the NRD guide,

(IV) the direct connection as in (III) with additional shield plates at the NRD guide aperture not attached to the standard metal waveguide.

The dimensions of the NRD guide, the rectangular waveguide (WR-10 standard for 75 to 110 GHz) and the dielectric rod taper section are given in *Figure 2.28*. The dimensions of the dielectric rod and its taper sections are taken

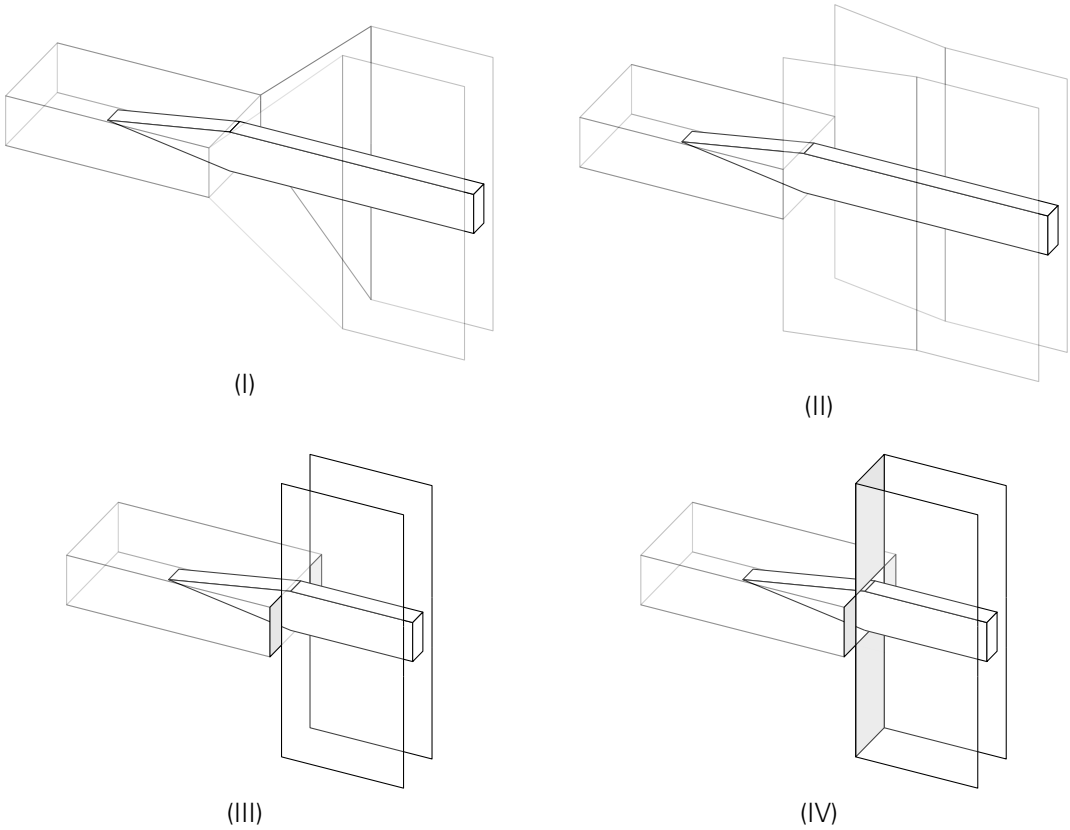

Figure 2.28: *Metal waveguide to NRD guide transition types: (I) pyramidal transition, (II) side wall opening, (III) direct connection and (IV) direct connection with additional shield plates*

from [9].

Whereas the NRD guide is attached directly to the rectangular waveguide for types (III) and (IV), a transition section with variable length is placed between the two waveguides for types (I) and (II) and the effect of the length on the reflection and transmission characteristics was studied. The NRD guide was modeled as described in Section 2.2 with a length of $l = 20$ mm. The leakage out of the NRD guide is affected by the height of the sidewalls, therefor its impact on the transmission characteristics was studied.

2.4.2 Simulation results

The cross-section of the NRD guide in the HFSS simulation models for the transition is shown in *Figure 2.12a* on page 15. To minimize simulation time and

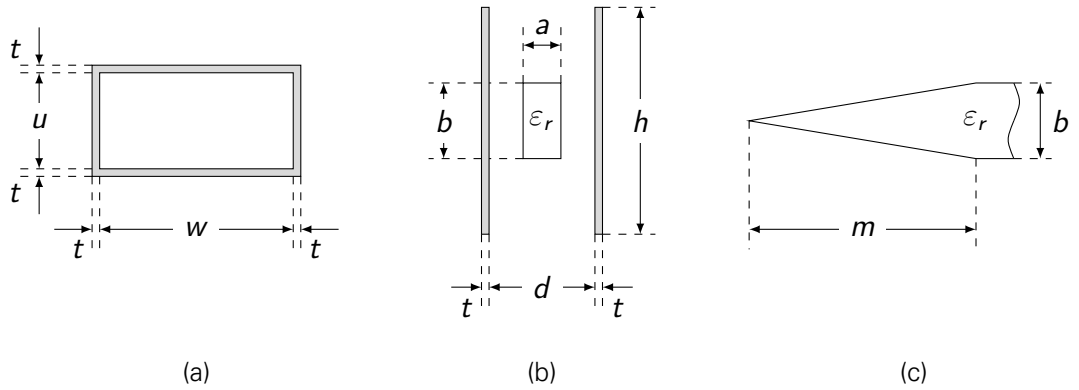

Figure 2.29: *(a) RWG cross-section, (b) NRD guide cross-section and (c) dielectric rod taper side view, with dimensions in* mm*:* $a = 0.5$, $b = 1$, $d = 1.4$, $h = 10$, $t = 0.1$, $e = 2.56$, $u = 1.27$ *and* $m = 6$ *(taper dimensions have been taken over from [9])*

computing ressources the symmetry of the structure is utilised by introducing electric and magnetic symmetry planes as described in Section 2.2.

The reflection and transmission characteristics of types (I) and (II) are shown in *Figures A.7* to *A.10* on pages 99 to 102. Although both transitions show comparable low reflection and good transmission behaviour for some of the studied configurations, their comparable complex build-up do not predestine them for integrated solutions.

The desired type of transition is type (III) which is easy to manufacture. The s -parameters obtained for transition (III) are illustrated in *Figures 2.30* and *2.31*. As for the other types of transition, the reflection coefficient $s^{\mathrm{dB}}_{11|(\mathrm{III})}$ stays well below -20 dB. For the reflection coefficient $s^{\mathrm{dB}}_{21|(\mathrm{III})}$ it is seen from *Figure 2.31* that for $h = 3$ mm leakage out of the NRD guide occurs for lower frequencies, whereas for frequencies higher than $f \approx 100$ GHz s_{21} decreases again. The reason for that is the distance of the metal plates d defined in Section 2.2, which is set to $d = 1.4$ mm with an upper frequency of $f_u \approx 100$ GHz. This effect is not that prominent for bigger values of h. The spikes appearing in the transmission diagram for frequencies higher than f_u are possibly due to resonances in the NRD guide. However, this has not been investigated explicitly in this thesis. Transition type (III) with additional shield plates at the NRD guide sidewalls as seen in *Figure 2.28IV* does not show better reflection and transmission characteristics than transition type (III), and therefore it is not studied any further.

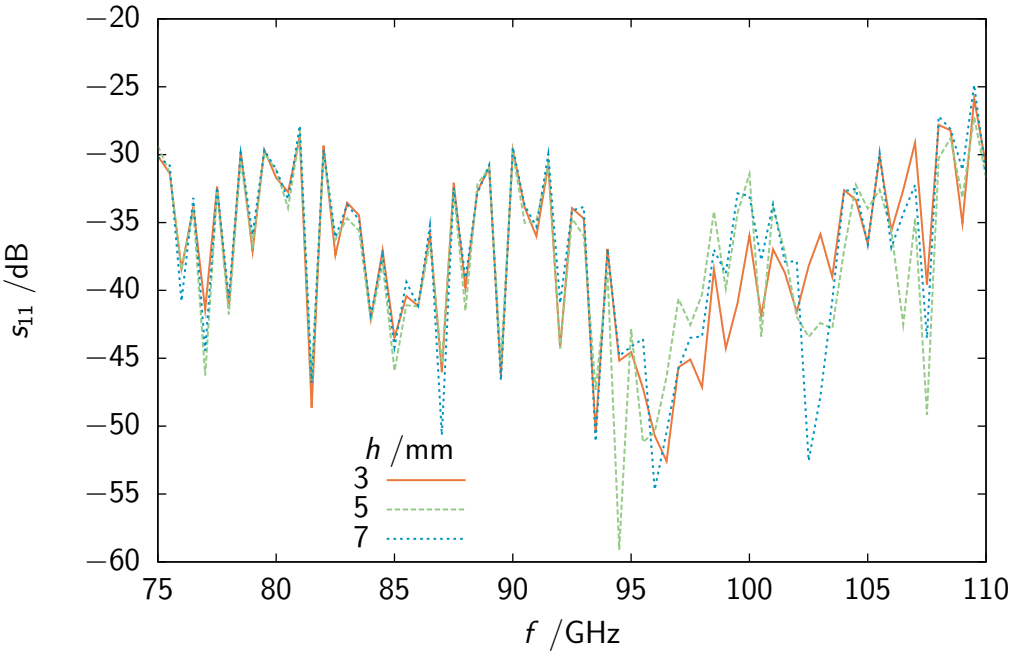

Figure 2.30: *Reflection coefficient* s_{11}^{dB} *of transition type (III) with dimensions in* mm $a = 0.5$, $b = 1$ *and* $d = 1.4$

The transition of choice is transition type (III), where the two waveguides are attached to each other directly with a tapered dielectric rod (*Figure 2.32* shows a schematic model of the NRD guide with two transitions). Looking at the reflection coefficient $s_{11|(III)}^{\mathrm{dB}}$ for the classical NRD guide with $a = d = 1.4$ mm in *Figure 2.33* spikes of high reflection at $f_1 \approx 95$ GHz and $f_2 \approx 104$ GHz can be seen, caused at the transition and decreasing the transmission characeristic for that frequencies.

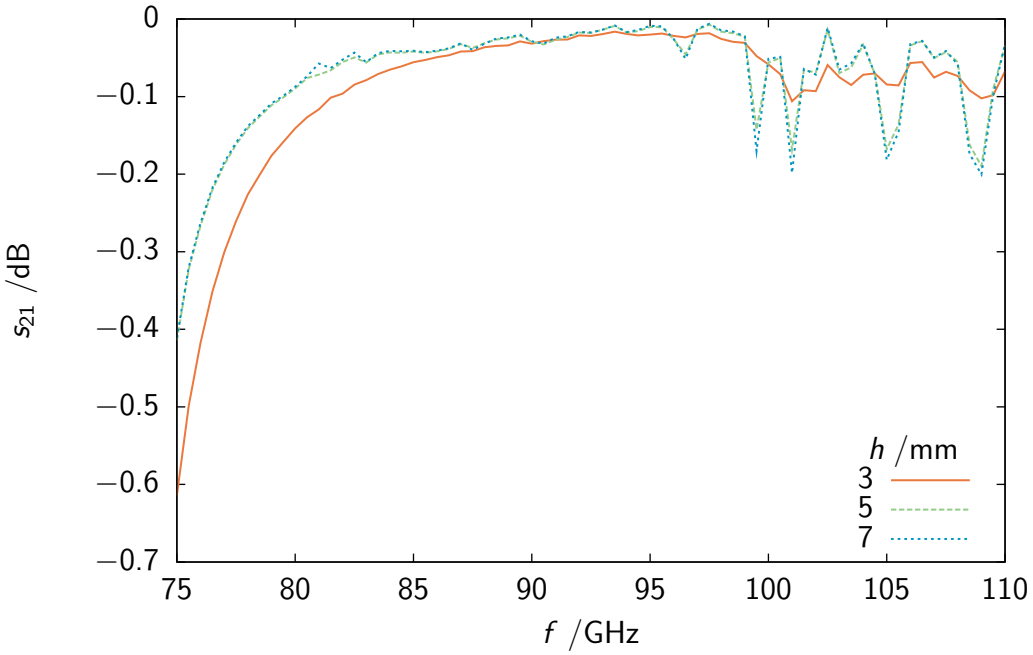

Figure 2.31: *Transmission coefficient* s_{21}^{dB} *of transition type (III) with dimensions in* mm $a = 0.5$, $b = 1$ *and* $d = 1.4$

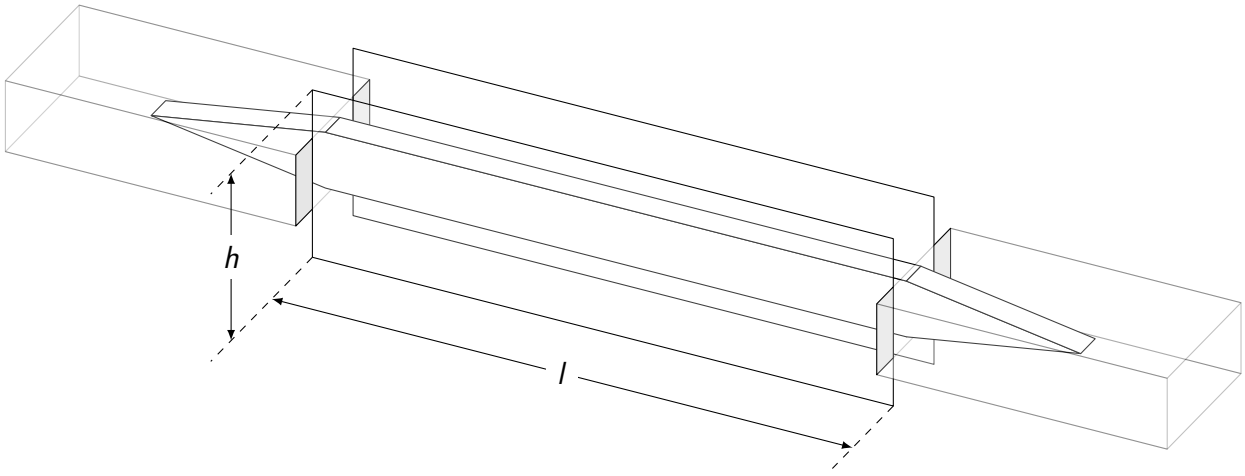

Figure 2.32: *HFSS simulation model of the chosen NRD guide with transitions of type (III) with* $l = 20$ mm

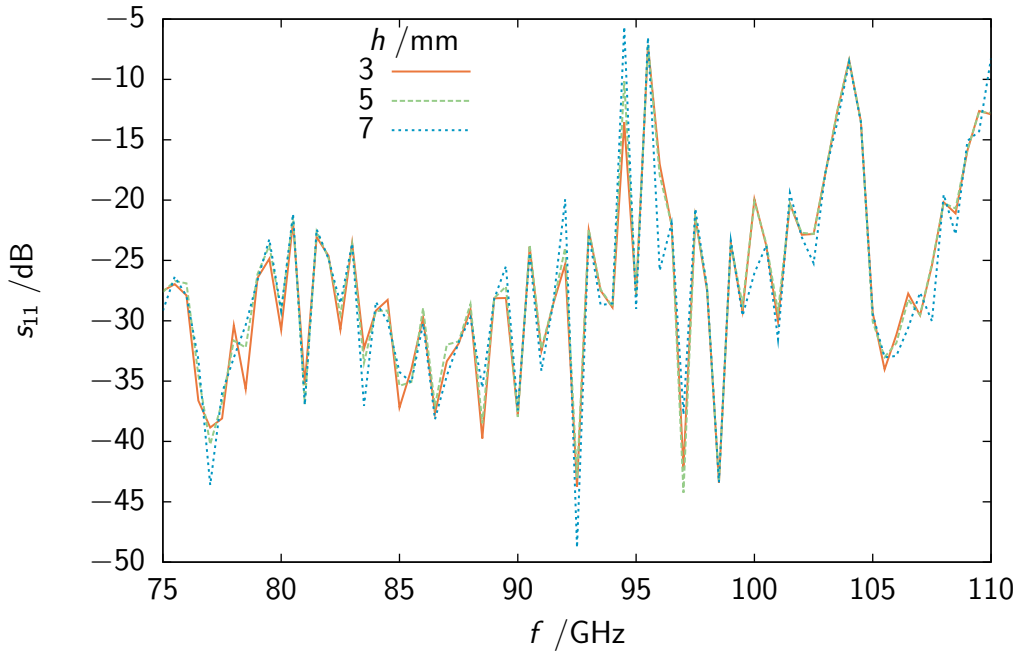

Figure 2.33: *Reflection coefficient* s_{11}^{dB} *of transition type (III) for* $a = d$ *and* $b = 0.75$ mm

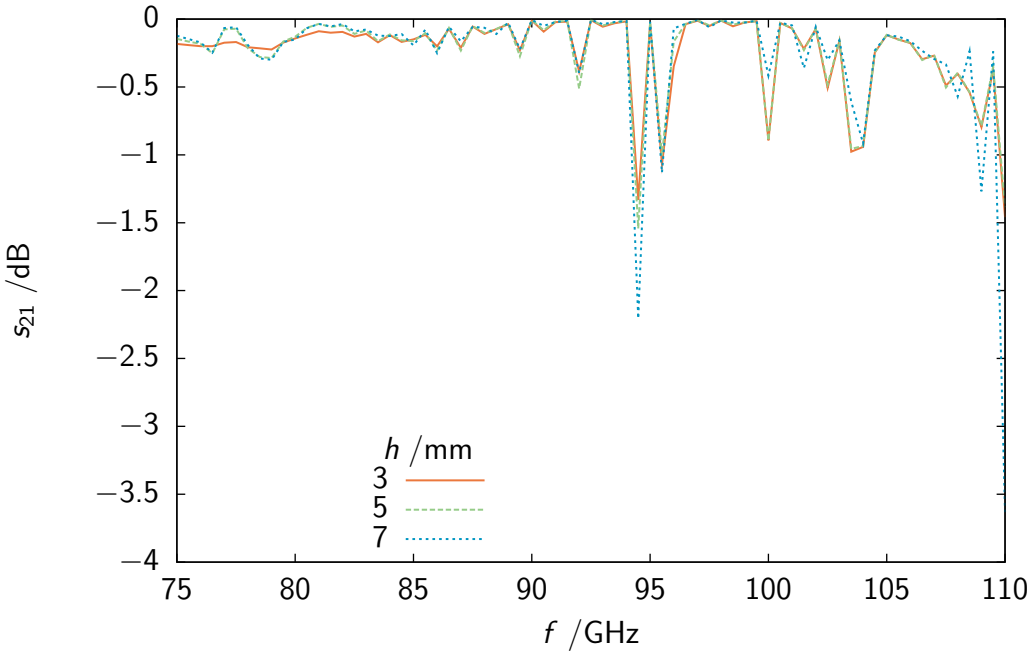

Figure 2.34: *Transmission coefficient* s_{21}^{dB} *of transition type (III) for* $a = d$ *and* $b = 0.75$ mm

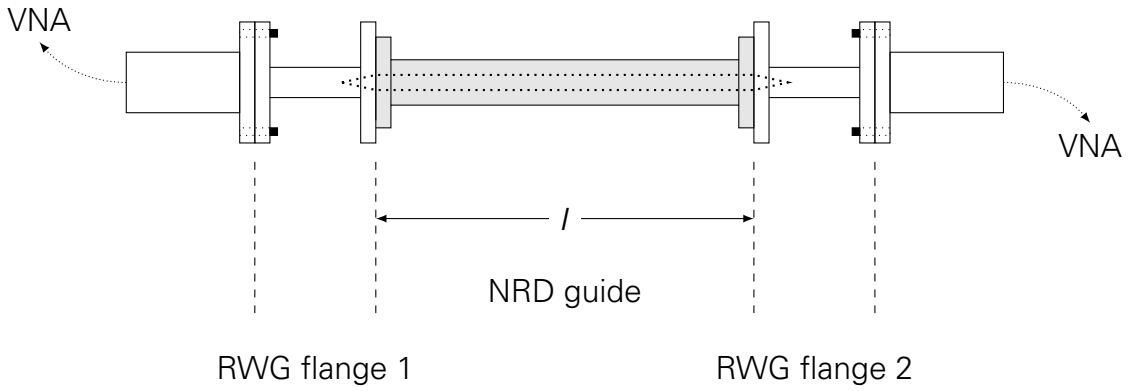

Figure 2.35: *Metal waveguide to NRD guide transition measurement setup with* $l = 32$ mm

2.4.3 Measurement results

The measurement setup is illustrated schematically in *Figure 2.35*. For the experimental verification of the simulation results of the transition, two aluminium sidewalls with appropriate connectors for the standard metal waveguide segments were fabricated. The dielectric rod was placed symmetrically between the sidewalls, adjusted and hold by styrofoam spacers and the sidewalls were screwed to metal waveguide flanges. The cross-section and the top-view schematics of the experimental NRD guide are shown in *Figures 2.36* and *2.37* on page 50. This setup formed the device under test (DUT) attached to the test port connectors of the HP8530A *vector network analyzer* (VNA). *Figure 2.38* shows a picture of the DUT in the test measurement setup.

The NVA delivers the reflection and the transmission coefficient as a complex number $s_{x1} = \mathrm{Re}(s_{x1}) + j \cdot \mathrm{Im}(s_{x1})$ which can be transformed into the polar form $s_{x1} = \mathrm{mag}(s_{x1}) \cdot e^{j\varphi}$ to get the magnitude and the phase of the complex reflection or transmission coefficient in the post-processing. Often the reflection coefficient is expressed in dB and refered to as *return loss* [27]

$$s_{11}^{\mathrm{dB}} = L_{\mathrm{return}} = -20 \cdot \log |s_{11}| \ \mathrm{dB} \ , \tag{2.105}$$

and for the transmission coefficient s_{21} the *gain*:

$$s_{21}^{\mathrm{dB}} = G = 20 \cdot \log |s_{21}| \ \mathrm{dB} \ . \tag{2.106}$$

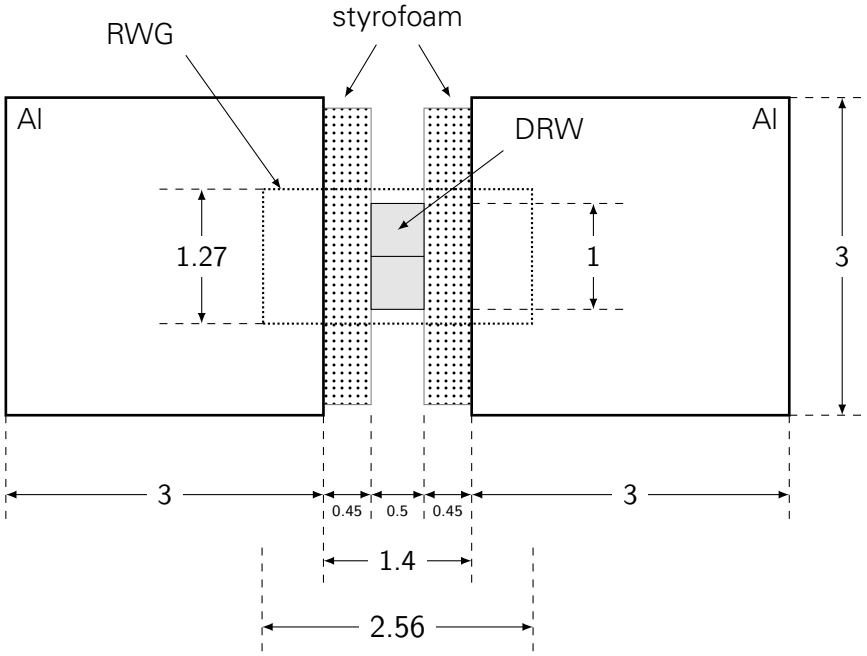

Figure 2.36: *Cross-section of the transition measurement setup with dimensions in* mm

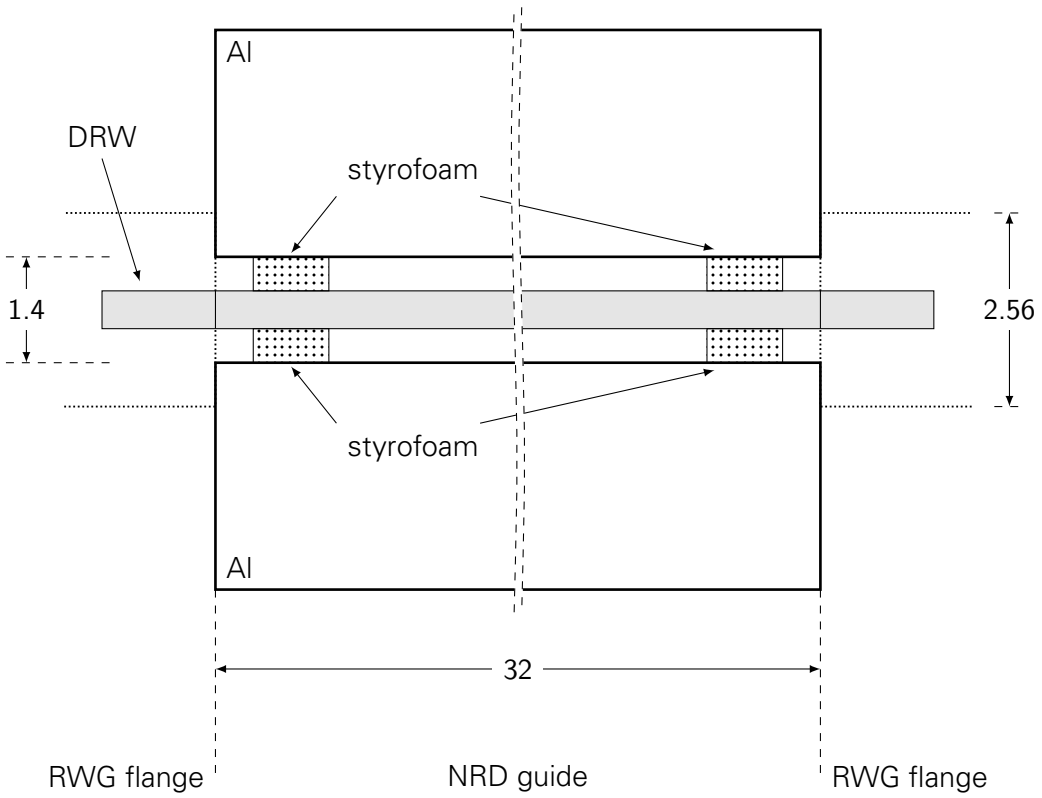

Figure 2.37: *Top view of the transition measurement setup with dimensions in* mm

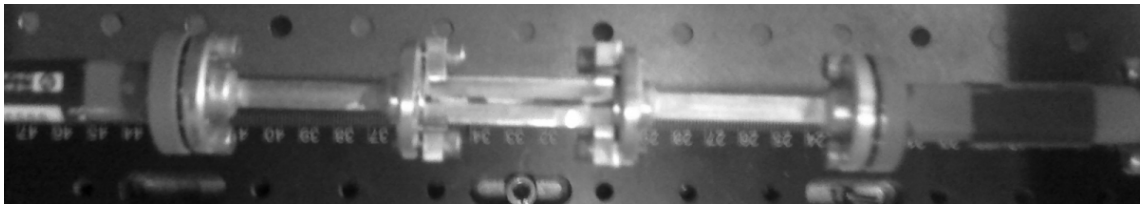

Figure 2.38: *Picture of the measurement setup showing the experimental NRD guide attached to two metal waveguide sections connected to the VNA*

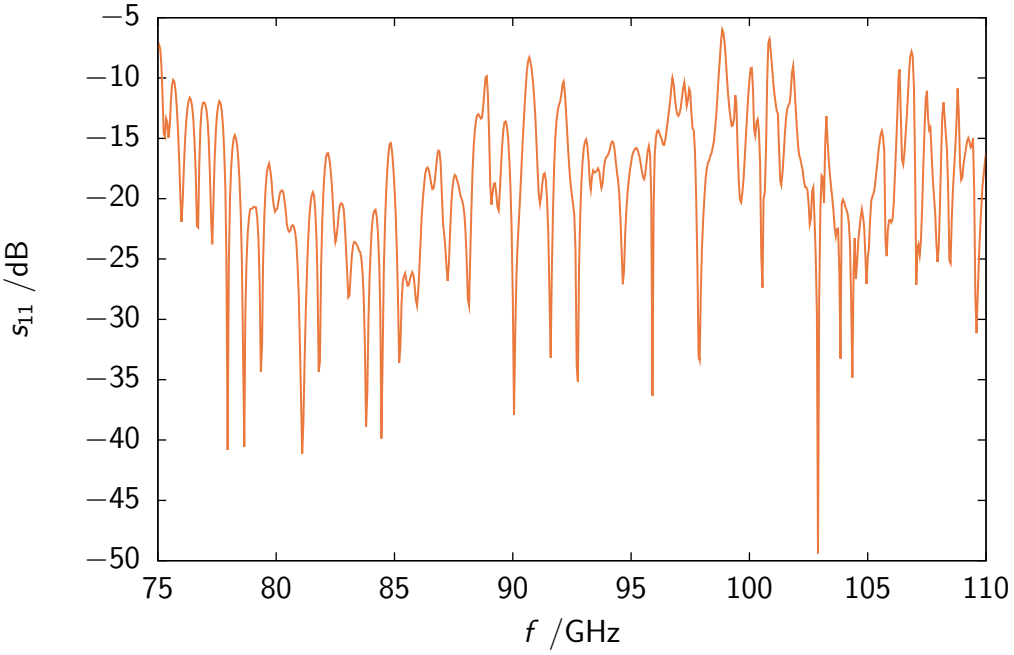

Figure 2.39: *Measured reflection coefficient s_{11}^{dB} of the experimental transition*

As the setup consisted of a very experimental NRD guide with a narrow dielectric rod, it can be seen from the cross-section and the top view that the correct symmetric placement of the NRD guide sidewalls to the RWG flanges and the dielectric rod between the sidewalls and the metal waveguide by hand was challenging. Also the correct position of the dielectric rod could not be ultimately verified. Furthermore the used RWG flanges placed between the NRD guide and the VNA port connectors introduced further sources of error.

The measured reflection coefficient s_{11} in dB is shown in *Figure 2.39*. The beforementioned difficulties with the experimental setup caused higher reflections in certain frequency areas compared to the simulation results. The simulated

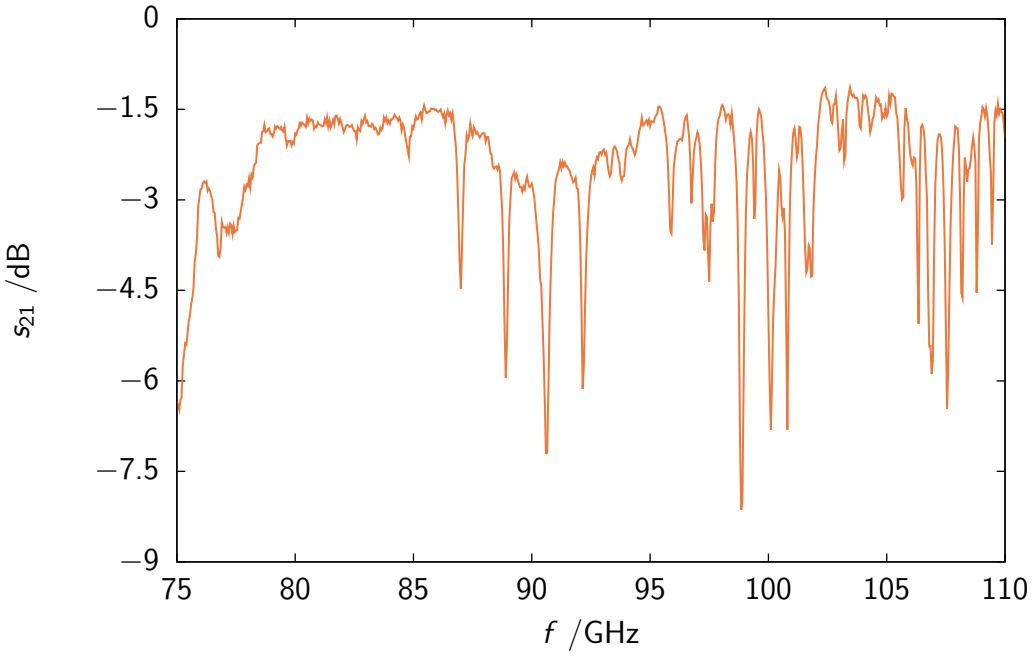

Figure 2.40: *Measured transmission coefficient s_{11}^{dB} of the experimental transition*

reflection coefficient stayed well below -20 dB for the whole frequency range from 75 to 110 GHz, whereas the measured results only shows good reflection characteristics with $s_{11} < -15$ dB for the frequency range between 80 and 95 GHz (with spikes occuring around 90 GHz). Analyzing the transmission coefficient s_{21} in *Figure 2.40* shows the poor transmission characteristics of the assembled NRD guide for frequencies below $\sim$ 80 GHz. However, above that frequency the investigated NRD guide with the transitions demonstrates comparable good transmission characteristics having the experimental nature of the studied NRD guide in mind, besides the spikes caused by unwanted reflections. The design of the NRD guide was set to have a distance of the metal plates $d = 1.4\ \mathrm{mm} < \lambda_{0|100\ \mathrm{GHz}}$ and thus its non-radiating attitude was limited to 100 GHz, which explains the decrease of the transmission properties for frequencies above 100 GHz (refer to the simulation model of the NRD guide in Section 2.2). For a better evaluation a different setup would be needed, where the placement of the dielect rod at the transition can be fine-tuned. With a more precisely manufactured waveguide (especially for the classical NRD guide with $a = d$) the metal waveguide to NRD guide transition is supposed to demonstrate a significantly improved reflection and transmission characteristic compared to the experimental one presented in this Section.

3 NON-RADIATING DIELECTRIC WAVEGUIDE ANTENNAS

The non-radiating properties of the NRD guide offers interesting applications of this waveguide for antenna purposes. In this chapter two different NRD guide antennas are presented. Based on the NRD guide developed in Chapter 2 and on the concept of a DRW antenna proposed in [9], an NRD guide end-fire antenna was designed, simulated and verified experimentally. Introducing discontinuities along the guiding structure of the NRD guide and modifying the metal plates, it is possible to alter the propagation properties to make the antenna structure leaky. The metal plates can either be foreshortened, enabling radiation out of the waveguide permanently, or the properties of the metal plates are changed by applying a special texture on its surface and thus making them high impedance surfaces which allows to controll the radiation. A concept of periodic leaky-wave antennas using NRD guides with HIS is presented in this Chapter.

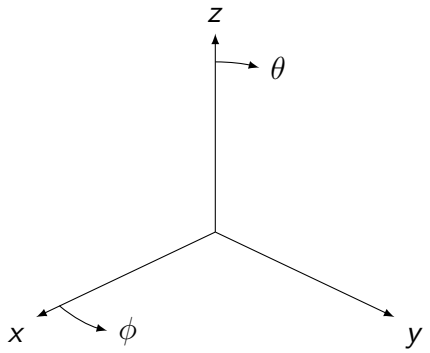

Figure 3.1: *Spherical coordinate system used for antenna parameter computations*

3.1 Basic principles

3.1.1 Antenna parameters

For antenna characteristics a spherical coordinate system as illustrated in *Figure 3.1* is used. Per definition the principal direction of propagation of the simulated antenna structures is set to be the *y* -direction.

Principal radiation patterns

Very often the performance characteristics of linearly polarized antennas are described in terms of their **E** - and **H** -plane far-field radiation patterns, refering to the plane containing the **E** or **H** field in the direction of maximum gain [28] as shown in *Figure 3.2* for a vertical polarized antenna: the electric field lies in the elavation plane with $\phi = \frac{\pi}{2}$ and the magnetic field in the azimuthal plane with $\theta = \frac{\pi}{2}$.

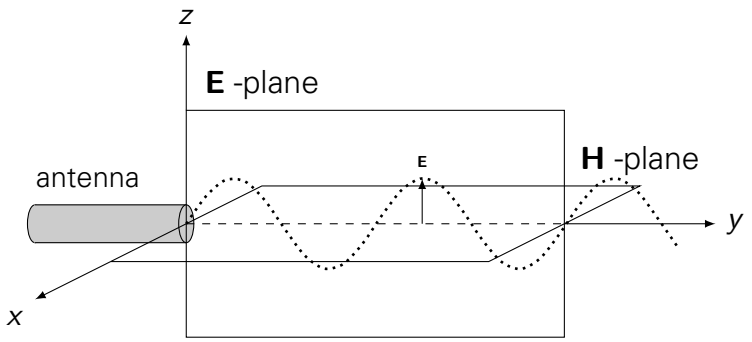

Figure 3.2: *Definition of the* **E** *- and* **H** *-plane of a vertical polarized antenna*

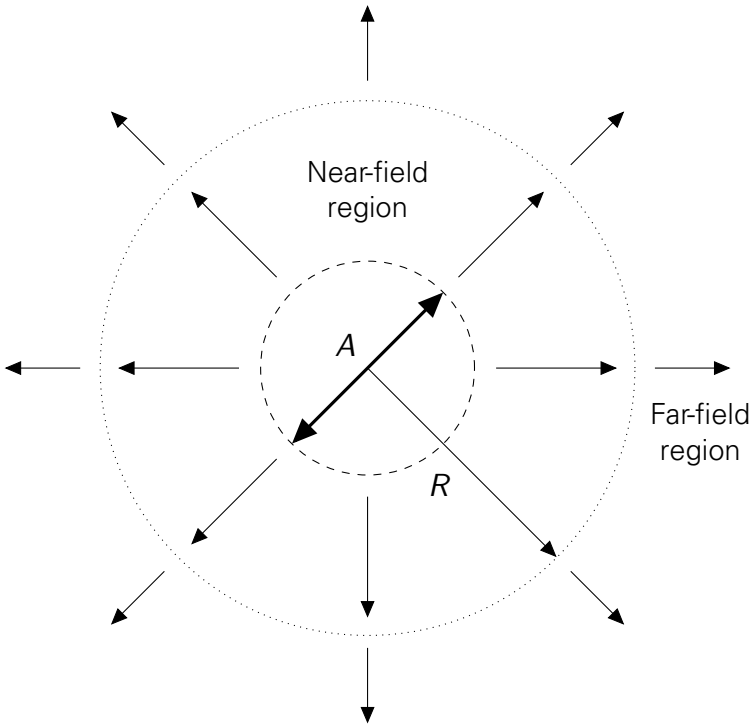

Figure 3.3: *Near-field and far-field region surrounding an antenna with diameter D [30]*

Field Regions

Usually the space an antenna is enlosed to is classified into two regions: the near-field (NF) and the far-field (FF) region – also refered to as FRAUNHOFER region – shown in *Figure 3.3*, whereat the near-field region is subdivided into the *reactive* and the *radiating* near-field (FRESNEL) region [28]. The boundary between the NF and the FF range is defined by the FRAUNHOFER distance [29]

$$R = \frac{2A^2}{\lambda} \tag{3.1}$$

where A is the antenna diameter and λ the free space wavelength of the radiated electromagnetic wave [28]. The far-field describes that region compared to an antenna where the angular field distribution is independent from the distance to the antenna [28].

Directivity, gain and radiation efficiency

Directivity

$$D(\phi,\theta) = \frac{P(\phi,\theta)}{P_{\text{isotropy}}} \tag{3.2}$$

$$D_0 = D(\phi,\theta)\,|_{\text{max}} \tag{3.3}$$

antenna radiation efficiency

$$e = e_{cd} = e_c e_d \tag{3.4}$$

with e_c being the conductive and e_d the dielectric efficiency. Because e_c and e_d are very difficult to compute, they are usually determined experimentally [28]. From the definition of the radiated power

$$P_{\text{rad}} = eP_{\text{in}} \tag{3.5}$$

it is possible to describe the antenna radiation efficiency with

$$e = e_{cd} = \frac{P_{\text{rad}}}{P_{\text{in}}}\,. \tag{3.6}$$

Compared to the directivity, the gain of an antenna also takes losses into account which occur in the antenna structure, namely conductive and dielectric losses, but not losses due to mismatching and is related to the directivity by the antenna radiation efficiency:

$$G(\phi,\theta) = eD(\phi,\theta) \tag{3.7}$$

and in a similar way the maximum gain is interrelated with the maximum directivity:

$$G_0 = G(\phi,\theta)\,|_{\text{max}} = e_{cd} D(\phi,\theta)\,|_{\text{max}} \tag{3.8}$$

$$G_0 = eD_0\,. \tag{3.9}$$

3.1.2 Leaky-wave antennas

Uniform leaky-wave antennas

The physical structure of a uniform leaky-wave antenna consists of a waveguide of a certain length L at which the leakage occurs through a proper leakage mechanism. The oldest concept of a leaky-wave antenna is a rectangular waveguide with a continuous slit along its sidewall [31]. In order to be suitable as a uniform leaky-wave antenna, the dominant mode has to operate in the fast-wave region ($v_{ph} > c$) and therefor its phase constant β has to fullfill the condition

$$\frac{\beta}{k_0} < 1 \tag{3.10}$$

where k_0 is the wavenumber in free space. After deriving the phase constant β and the attenuation constant α of the guiding structure, the beam angle θ_m and the beam width $\Delta\theta$ can then be calculated by the simple equations

$$\sin(\theta_m) \approx \frac{\beta}{k_0} \tag{3.11}$$

$$\Delta\theta \approx \frac{1}{(L/\lambda_0)\cos(\theta_m)} \tag{3.12}$$

where θ is measured perpenticular to the direction of propagation inside the guiding structure (*Figure 2.2* on page 6 illustrates the used coordinate system with the wave traveling along the z-axis in the waveguide).

The conventional NRD guide can be modified to make it leaky. One way is to foreshorten the parallel plates at the top, which prevend the waveguide to radiate. However, this only works if the phase constant of the dominant propagation mode operates in the fast-wave region and fullfills equation (3.10). The concept is illustrated in *Figure 3.4*. The parameter d indicating the distance the parallel plates are continued above the dielectric then controls the leakage of the antenna. An overview of uniform NRD guide leaky-wave antennas is given in [32].

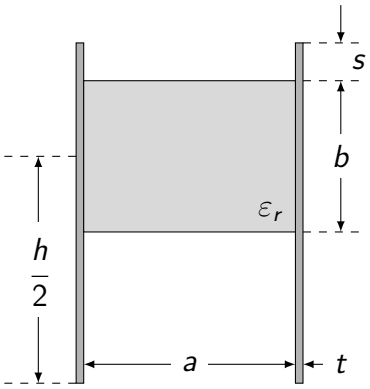

Figure 3.4: *Foreshortened-top leaky-wave NRD guide antenna developed by Sanchez and Oliner [33]. The leakage of the antenna is controlled by the stub length s.*

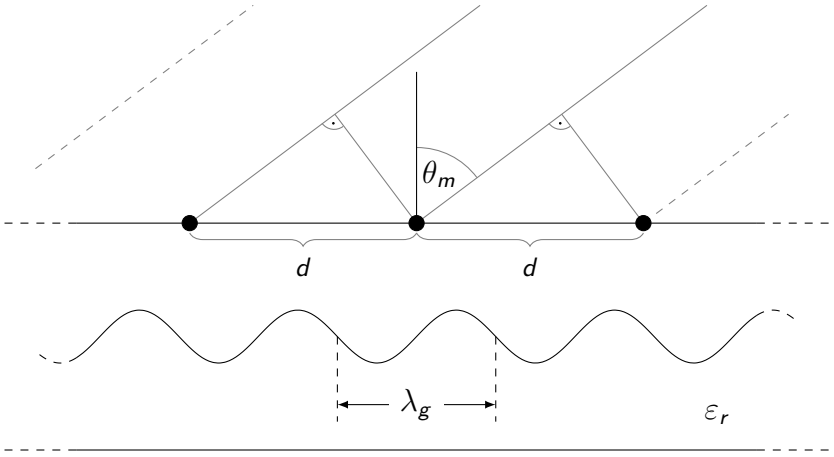

Figure 3.5: *Principle of operation of a periodic leaky-wave antenna with disconinuities separated by periodic distance d. The beam angle θ_m is counted from the perpendicular direction of the guiding structure.*

Periodic leaky-wave antennas

In the case that the dominant mode of propagation operates in the slow-wave region its phase constant β_0 is greater than the wavenumber in free space k_0:

$$\frac{\beta_0}{k_0} > 1 \, . \tag{3.13}$$

Therefore the dominant mode is purely bound to the guiding structure. Adding discontinuities introduces an infinity number of spatial harmonics [34] that can modulate the phase constant in a way that it fullfills equation (3.10). The resulting phase constant β_n is related to the phase constant β_0 of the dominant mode with

$$\beta_n d = \beta_0 d + 2n\pi, \quad -\infty \leqslant n \leqslant \infty \tag{3.14}$$

where d is the periodic distance between two subsequent discontinuities (compare *Figure 3.5*) and n is the order of a given space harmonic. Thereby $n = 0$ stands for the basic wave. Equation (3.14) can be rewritten in the following form

$$\frac{\beta_n}{k_0} = \frac{\beta_0}{k_0} + \frac{2\pi n}{k_0 d} = \frac{\beta_0}{k_0} + \frac{n\lambda_0}{d}\,, \tag{3.15}$$

$$\frac{\beta_n}{k_0} = \frac{\lambda_0}{\lambda_g} + \frac{n\lambda_0}{d}\,. \tag{3.16}$$

Introducing discontinuities along the guiding structure means introducing small radiation sources, which together form an antenna array. Explained otherwise, in a periodic structure formed by discontinuities, Floquet spatial harmonics appear, and some of them can be in the fast-wave region.

As the waveguide mode is operating in the slow wave region fulfilling equation (3.13), it can easily been seen from equation (3.16) that $\frac{\beta_n}{k_0}$ can be less than unity if $n < 0$ is considered. Therefore only negative spatial harmonics were observed. Substituting $\frac{\beta}{k_0}$ in equation (3.10) with $\frac{\beta_n}{k_0}$ from equation (3.15) leads to

$$\left|\frac{\beta_n}{k_0}\right| = \left|\frac{\beta_0}{k_0} + \frac{n\lambda_0}{d}\right| < 1\,. \tag{3.17}$$

Compared to uniform leaky-wave antennas it is possible to have backward radiation at periodic leaky-wave antennas if

$$-1 < \frac{\beta_0}{k_0} + \frac{n\lambda_0}{d} < 0\,. \tag{3.18}$$

In order to cause leakage radiation for a given free space wavelength λ_0, period d is limited to the range (derived from equation (3.17)):

$$\frac{-n\lambda_0}{\beta_0/k_0 + 1} < d < \frac{-n\lambda_0}{\beta_0/k_0 - 1} \tag{3.19}$$

$\underline{n = -1:}$

$$\frac{\lambda_0}{\beta_0/k_0 + 1} < d < \frac{\lambda_0}{\beta_0/k_0 - 1}\,. \tag{3.20}$$

The distance d of two subsequent discontinuities is also limited by the fact that it

Figure 3.6: *Cross-section of a Sievenpiper high impedance surface structure [37]*

is not desirable to have more than one lobe, which means the phase constant β_{-2} of the second spatial harmonic should in the ideal case not fullfill equation (3.10) and therefore:

$$\frac{\beta_{-2}}{k_0} < -1 \tag{3.21}$$

$$\frac{\beta_0}{k_0} - \frac{2\lambda_0}{d} < -1 \tag{3.22}$$

$$d < \frac{2\lambda_0}{\beta_0/k_0 + 1}\,. \tag{3.23}$$

The spatial harmonics are caused by reflection of the incident wave at the discontinuities. The phase difference between two consecutive strips is [35]

$$\Delta\phi = \beta_n d = \beta_0 d = \left(\beta_{-1} + \frac{2\pi}{d}\right) d = \beta_{-1} d + 2\pi\,. \tag{3.24}$$

The phase difference is $\Delta\phi = 2\pi$ for broadband radiation ($\theta_m = 0$) with $\beta_{-1} = 0$, which means that the reflected waves are in phase. This causes strong reflection for the given broadband radiation frequency and a strong attenuation of the propagating wave in that stop band. This behaviour can be reduced by using double-strips instead of single-strips for strip discontinuities [35].

3.1.3 High impedance surfaces

A *perfect magnetic conductor* (PMC) reflects the electromagnetic wave without changing the phase of the electric field (reflection coefficient $R = 1$), compared to a phase change of 180° at the reflection at perfect electric conductors (corresponding to a reflection coefficient of $R = -1$) [36]. In real life no perfect magnetic conductor exits. However, some artificial surfaces can achieve nearly the same behaviour for a specific frequency.

It is possible to alter the radiofrequency surface properties of a conductor

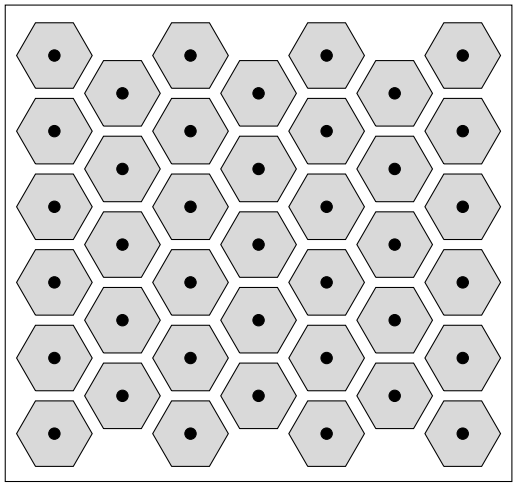

Figure 3.7: *Top view of a Sievenpiper high impedance surface structure [37]*

by adding a special texture onto it. If the period of the surface texture defining the unit cell is much smaller than the wavelength of the desired frequency, the structure can be described by its surface impedance [38]. Sievenpiper presented in [37] an easy to manufacture mushroom-like structure with its cross-section illustrated in *Figure 3.6* and its top-view in *Figure 3.7*. For the design frequency HIS behave like a PMC. In electromagnetic simulation tools HIS can be modeled as perfect magnetic conductors and thus there is no necessity to simulate the whole surface structure.

The original Sievenpiper HIS is set as a frequency selective surface (FSS) for a special frequency by design. The size of the unit cell defines the frequency for which it acts as a high impedance surface. Chicherin et al. (2008) introduced a voltage controlled high impedance surface for the **W** frequency band [39]. The proposed HIS consists of an array of electrically small MEMS capacitors placed atop of a ground plane and coupled to each other. The resonant frequency of the FSS is

$$f_{res} = \frac{1}{2\pi\sqrt{L_{eff}\,C_{eff}}}\,. \tag{3.25}$$

Applying a control voltage to the MEMS capacitors changes their capacitance and therefore the resonant frequency for which the texture acts as a HIS and the phase shift it creates. In [39] different applications for this tuneable HIS are discussed. Furthermore, with this approach the HIS can be seen as *switchable*.

3.2 NRD guide end-fire antenna

If a DRW with both ends attached to a metal waveguide is considered, an end-fire antenna can be easily implemented by letting one end open instead of matching it with a transition. The DRW with the taper section left open then works as an end-fire antenna. HFSS simulation results for this antenna are presented in simulation results in Appendix E. Based on that antenna introduced in [9], an NRD guide end-fire antenna with the NRD guide designed in Section 2.2 was developed (the schematic of this antenna is shown in *Figure 3.8*).

3.2.1 Design

The design of the antenna is identical to the NRD guide studied in Chapter 2. One end is attached to a metal waveguide, whereas the other is left open and the taper section acts as the radiating end. The antenna structure is sketched in *Figure 3.8*. The antenna consists of a silicon dielectric rod with two taper section at each end with the dimensions given in *Figure 2.29* and with length l, which is placed symmetrically between two metal plates. For the simulation model l was set to 20 mm, whereas for the measurement setup the same dielectric rod as in Section 2.4.3 with $l = 32$ mm was used.

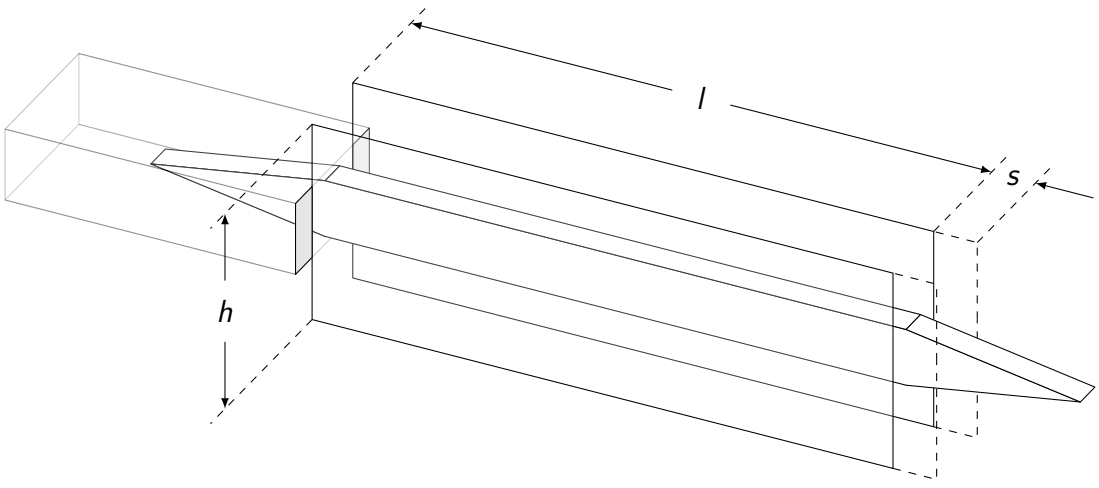

Figure 3.8: *NRD guide end-fire antenna model with prepended metal waveguide to NRD guide transition*

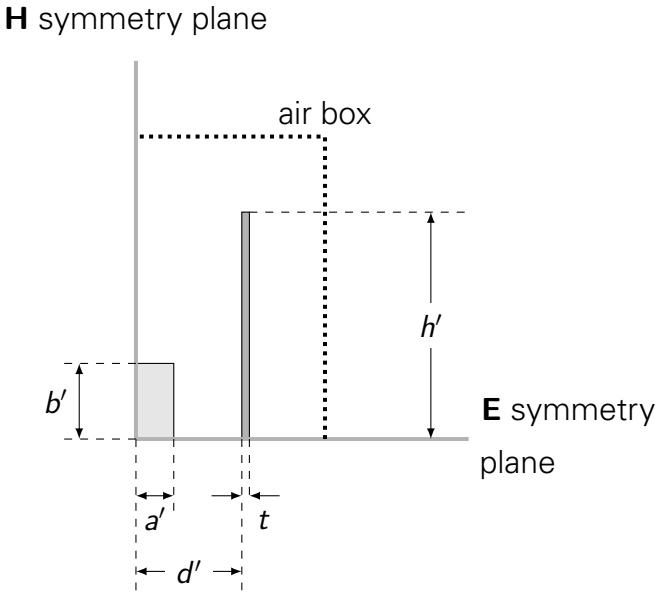

Figure 3.9: *Cross-sectional view of the NRD guide HFSS simulation model for the end-fire antenna with* **E** *and* **H** *symmetry planes with dimensions in* mm $a = 2a' = 0.5$, $b = 2b' = 1$, $d = 2d' = 1.4$, $t = 0.1$ *and* $h = 2h'$

3.2.2 Simulation results

Similarly to the simulated NRD guide model in Section 2.2, it is possible to reduce the simulation time of the simulation model by taking advantage of the electric and magnetic symmetry of the NRD guide. The cross-section of the HFSS simulation model with dimensions is shown in *Figure 3.9*. As the height of the metal plates has an influence on the radiation patterns, the variation of the height from 3 to 9 mm with a step size of 2 mm was investigated. As in this research only a conceptual model of the NRD guide end-fire antenna is presented, the radiation efficiency of the antenna was not studied and the dielectric rod was considered to be loss-less. The radiation characteristics of the NRD guide end-fire antenna were studied for $f_1 = 75$ GHz, $f_2 = 85$ GHz and $f_3 = 95$ GHz and the results for the **E** - and **H** -plane are presented in *Figure 3.11*. For illustration purposes the gain range was set from -10 to 10 dB. *Figure 3.12* displays the tridimensional radiation patterns of the NRD guide end-fire antenna with $s = 0$ (*Figures 3.12a* to *3.12c*) and $s = 3$ mm (*Figures 3.12d* to *3.12f*) with the same gain range.

The maximum gain G_0 listed in *Table 3.1* varies with the height of the metal plates and with frequency. For $h_3 = 7$ mm the effect of extending the metal plates half way over the radiating taper end, $s = 3$ mm, was studied. Interestingly thereby the maximum gain for higher frequencies f_2 and f_3 was increased,

Table 3.1: Maximum gain G_0^{dB} of the NRD guide and the DRW end-fire antenna

f /GHz	$h\|s$ /mm	G_0 /dB					
		3|0	5|0	7|0	7|3	9|0	DRWA
75		7.92	8.32	8.70	6.79	9.42	8.65
85		8.95	9.13	8.68	9.38	8.66	8.12
95		7.64	7.39	8.11	9.68	8.31	8.54

whereas decreased for f_1 compared to $s = 0$.

Looking at the plot of the maximum gain G_0 in respect to frequency in *Figure 3.10* the effect of the height of the metal plates can be seen. For $h = 9$ mm the antenna offers stable maximum gain $G_0 \approx 9.5$ dB for all three studied frequencies. For $h < 9$ mm and $s = 0$ the peak of the maximum gain appears for $f_2 = 85$ GHz.

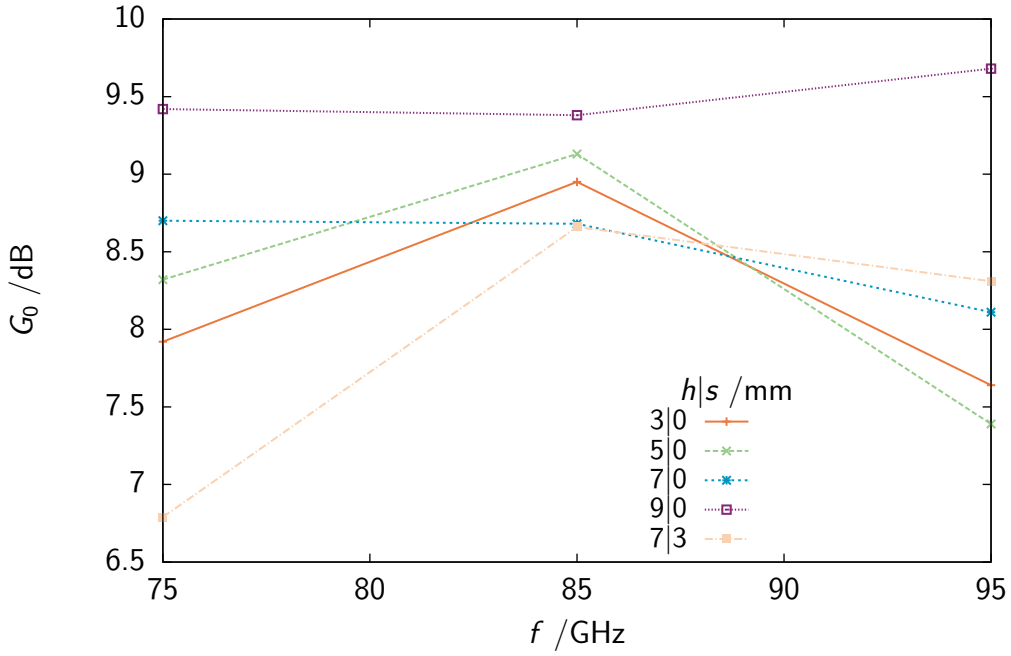

Figure 3.10: *Maximum gain G_0^{dB} (refer to Table 3.1)*

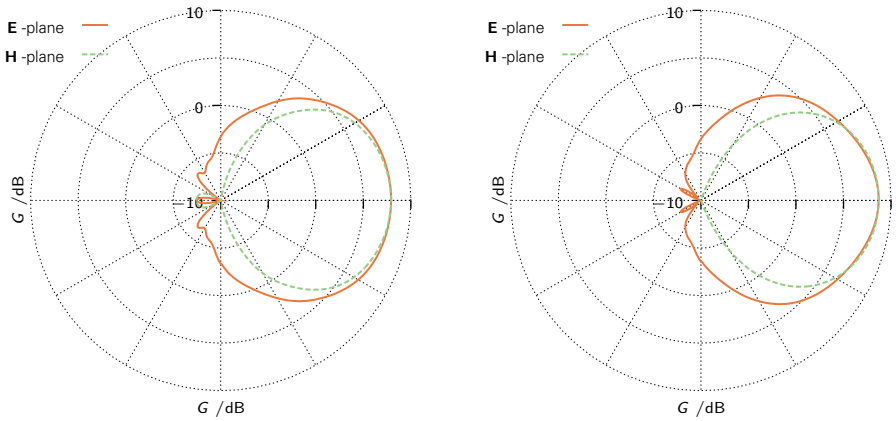

(a) $h_1 = 3$ mm , $f_1 = 75$ GHz

(b) $h_3 = 7$ mm , $f_1 = 75$ GHz

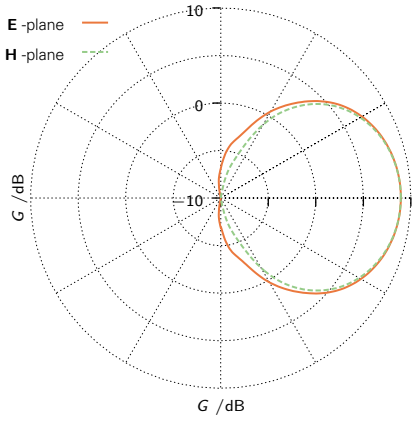

(c) $h_1 = 3$ mm , $f_2 = 85$ GHz

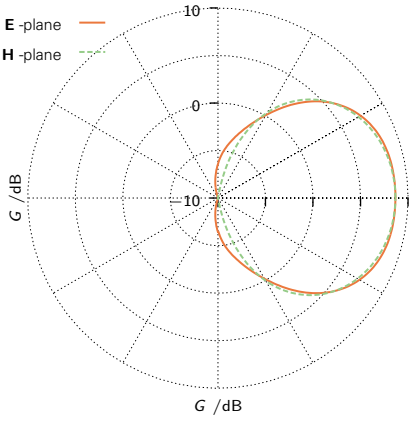

(d) $h_3 = 7$ mm , $f_2 = 85$ GHz

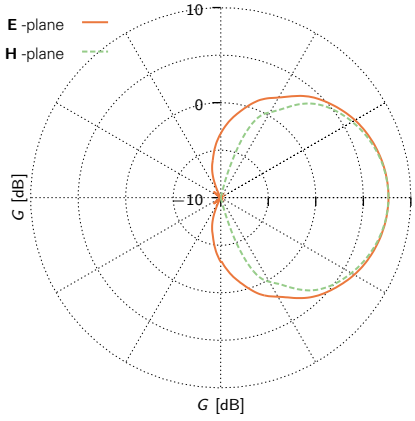

(e) $h_1 = 3$ mm , $f_3 = 95$ GHz

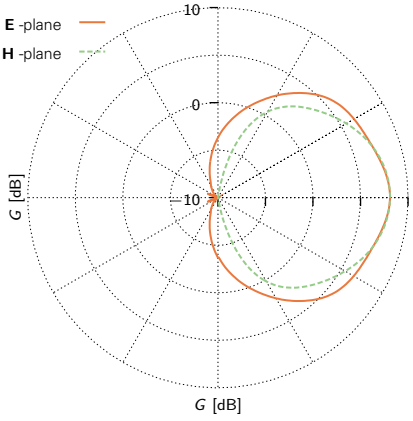

(f) $h_3 = 7$ mm , $f_3 = 95$ GHz

Figure 3.11: *Radiation patterns of the NRD guide end-fire antenna*

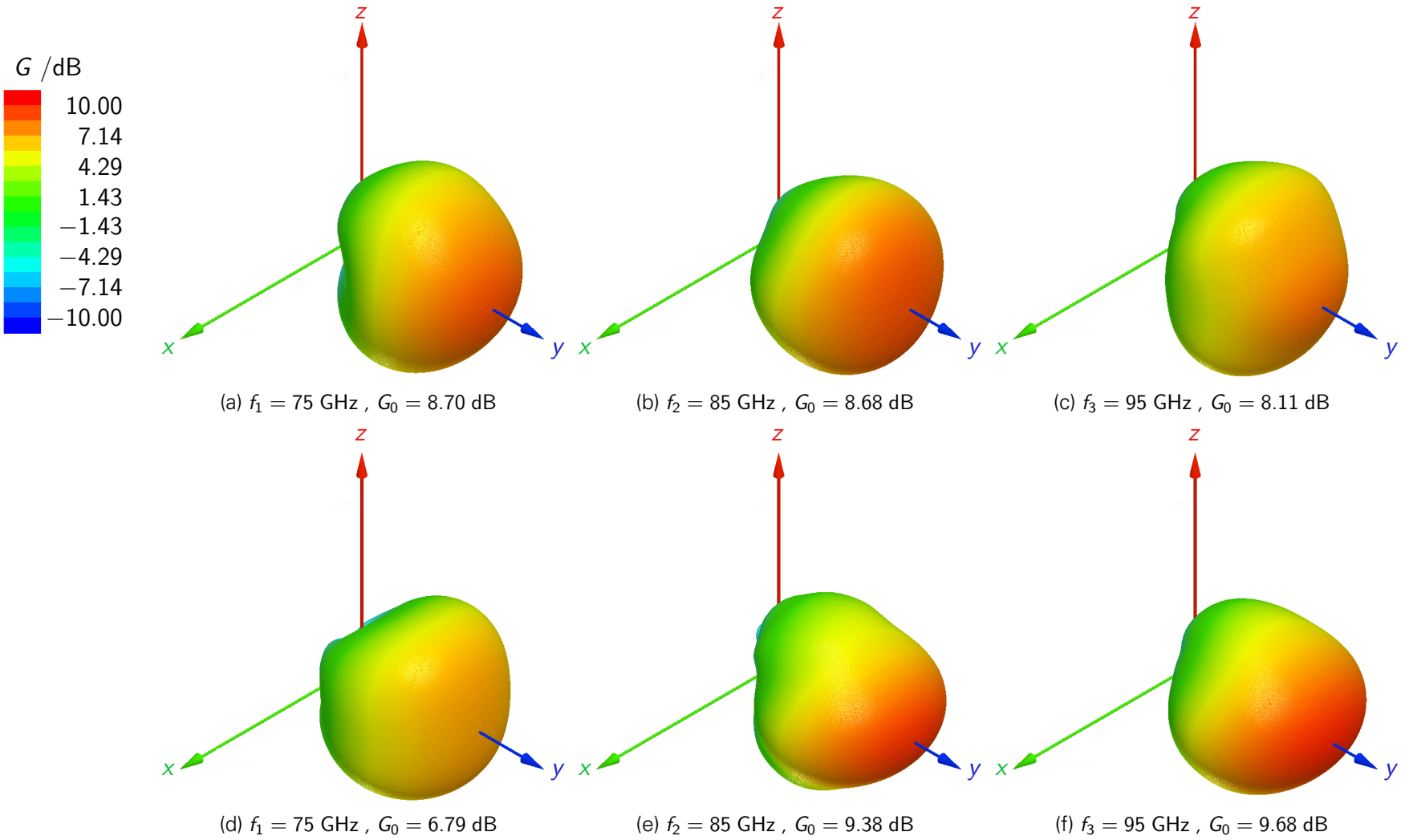

(a) $f_1 = 75$ GHz , $G_0 = 8.70$ dB (b) $f_2 = 85$ GHz , $G_0 = 8.68$ dB (c) $f_3 = 95$ GHz , $G_0 = 8.11$ dB

(d) $f_1 = 75$ GHz , $G_0 = 6.79$ dB (e) $f_2 = 85$ GHz , $G_0 = 9.38$ dB (f) $f_3 = 95$ GHz , $G_0 = 9.68$ dB

Figure 3.12: *HFSS 3D polar radiation plot of gain G^{dB} for the NRD guide end-fire antenna (a) – (c) without ($s = 0$) and (d) – (f) with extended metal plates ($s = 1.5$ mm), $h = 7$ mm*

Comparison to DRW end-fire antenna

The non-radiating behaviour of the NRD guide and the shielding effect of the metal plates improves the radiation characteristics compared to that of the DRW end-fire antenna presented in [9]. *Figure 3.13* shows the comparison between the NRD guide end-fire antenna with metal plate height $h = 3$ mm and $h = 7$ mm and the DRW end-fire antenna discussed in Appendix E for $f_1 = 75$ GHz. The comparison of the radiation patterns for $f_2 = 85$ GHz and $f_3 = 95$ GHz are illustrated in *Figures A.18* and Figure A.19 on page 109 and 110 respectively. As can be seen from the figures, the radiation patterns are smoothed by the introduction of the parallel metal plates canceling out the ripples of the DRW antenna in the range from -90° to 90°. Therefore, the proposed NRD guide end-fire antenna improves the radiation characteristics compared to the DRW end-fire antenna.

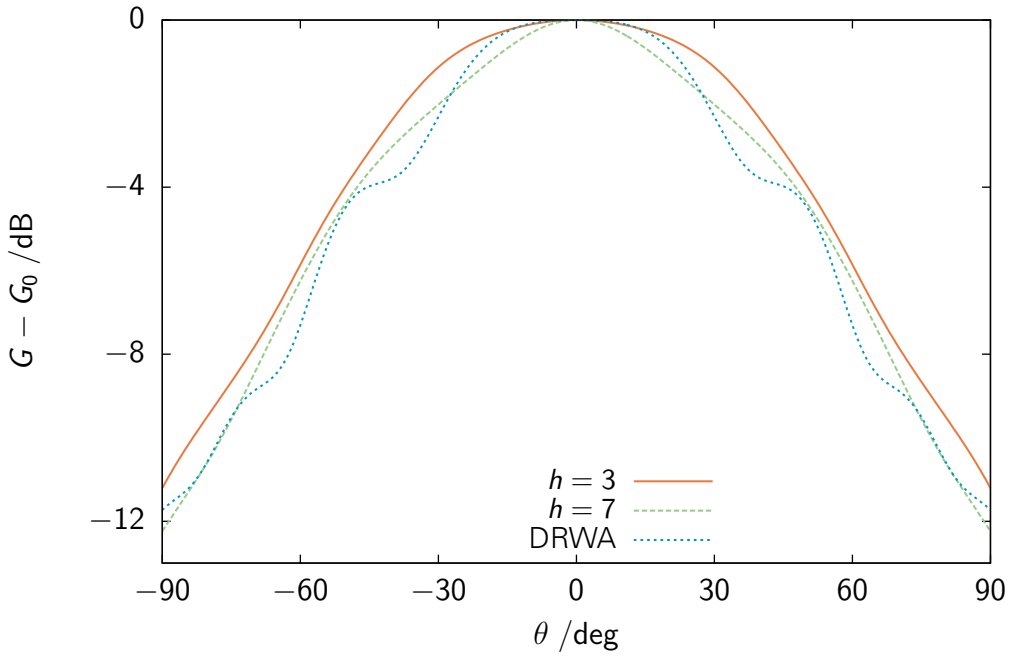

(a) **E** − *plane* , $f_1 = 75$ GHz

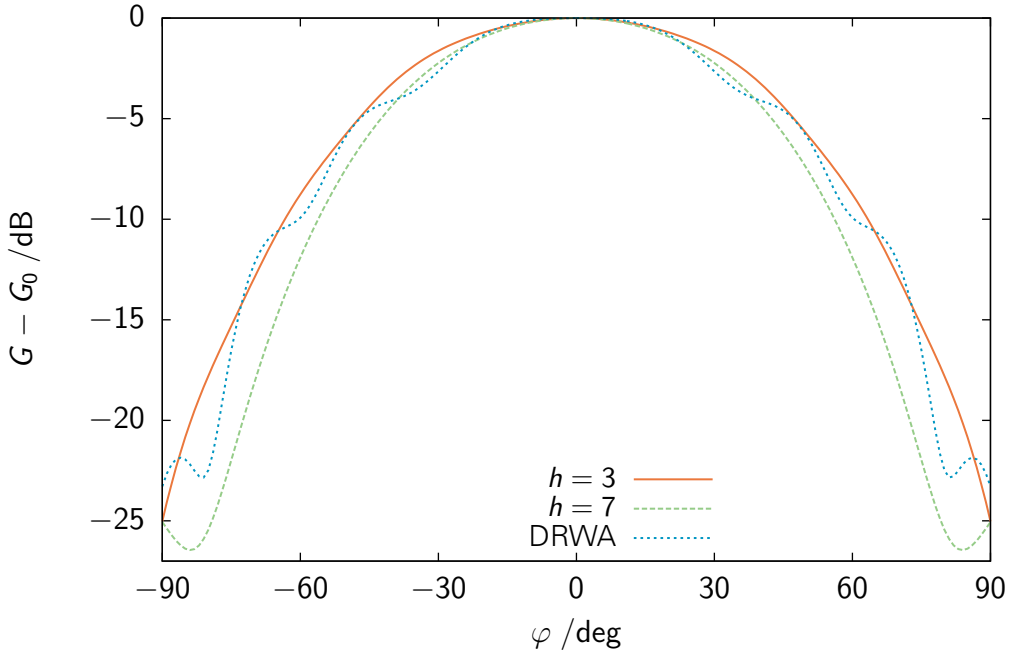

(b) **H** − *plane* , $f_1 = 75$ GHz

Figure 3.13: *Comparison of the radiation patterns of the NRD guide and the DRW end-fire antenna for different values of the plate height* h *in* mm *for* $f_1 = 75$ GHz

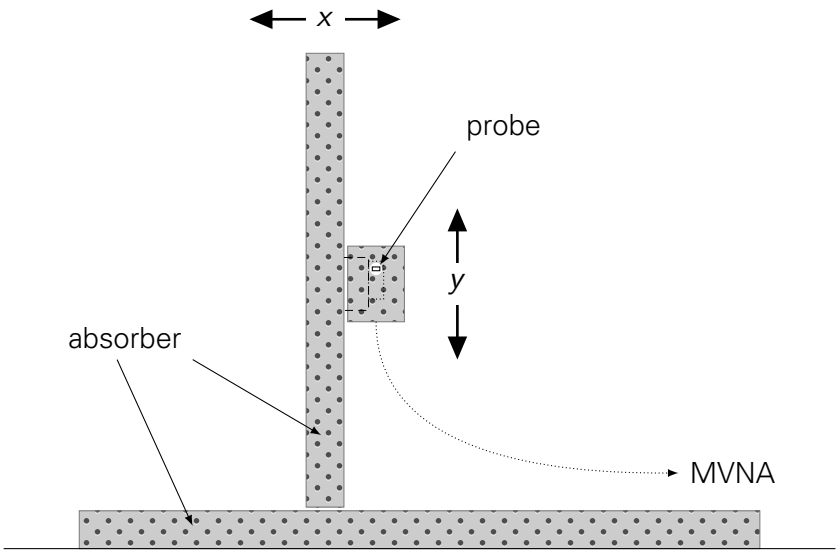

Figure 3.14: *Front view of the NSI planar scanner*

3.2.3 Measurement results

To measure the far-field radiation patterns of the NRD guide end-fire antenna a planar scanner from *Nearfield Systems Inc.*[1] (NSI) was used. The front view of the scanner is shown schematically in *Figure 3.14*. The probe consisting of an open rectangular waveguide is placed on the scanning unit and can be moved in the horizontal x - and vertical y -direction to scan the radiation patterns in two dimensions. The equipment of the planar scanner is shielded with absorbers to prevent undesired reflections. The measurement setup is sketched in *Figures 3.15* and *3.16* on page 70 and was set up in a temperature and humidity controlled anechoic chamber. Both the antenna under test (AUT) and the probe were connected to a millimeter vector network analyzer (MVNA) from *AB Millimetre*[2]. The MVNA-8-350 system[3] is capable of covering a frequency range from 8 to 350 GHz. The measurement procedure and the record of the radiation patterns were controlled by a computer with the NSI2000[4] antenna measurement software. With that software it is possible to program the scanner to scan a predefined area with a possible step size of $\Delta s = 1$ mm. The AUT was placed at a distance of $d_m = 15$ cm away from the probe. Due to setup limitations the maximum scanning angles in the vertical and horizontal plane were limited from the movement of the scanning unit.

[1] http://www.nearfield.com/
[2] http://www.abmillimetre.com/
[3] http://www.abmillimetre.com/Products.htm
[4] http://www.nearfield.com/sales/software.htm

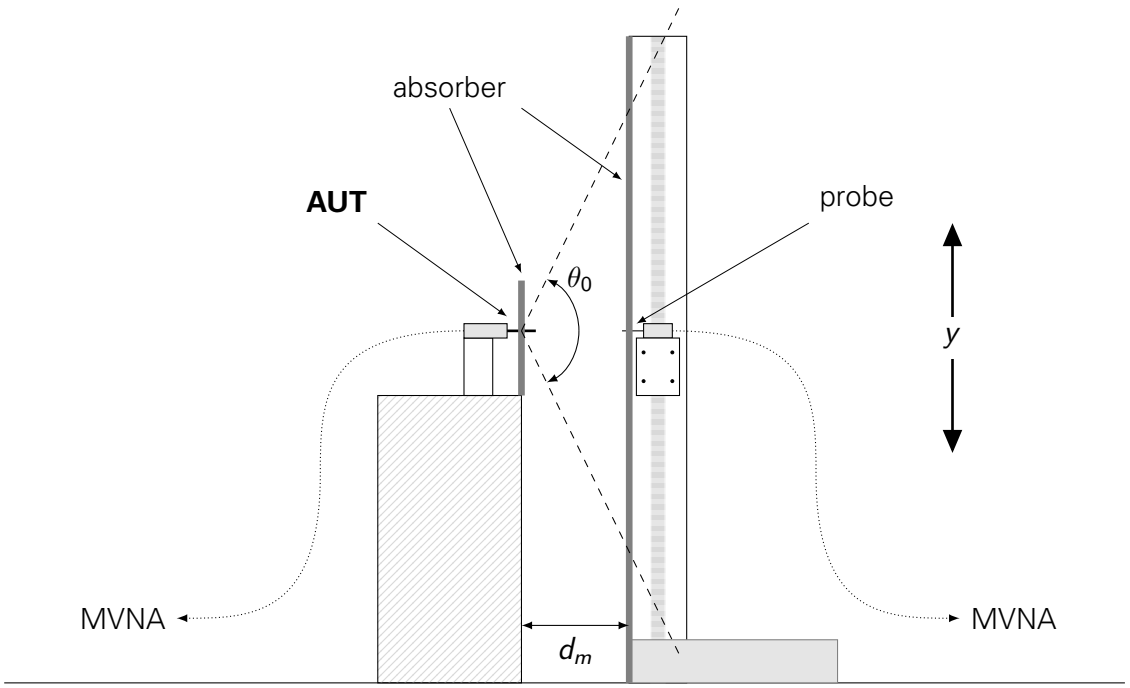

Figure 3.15: *Side view of the end-fire antenna measurement setup with $\theta_0 = \theta_{max}$ indicating the maximum vertical scanning angle in the* **E** *-plane due to setup limitations*

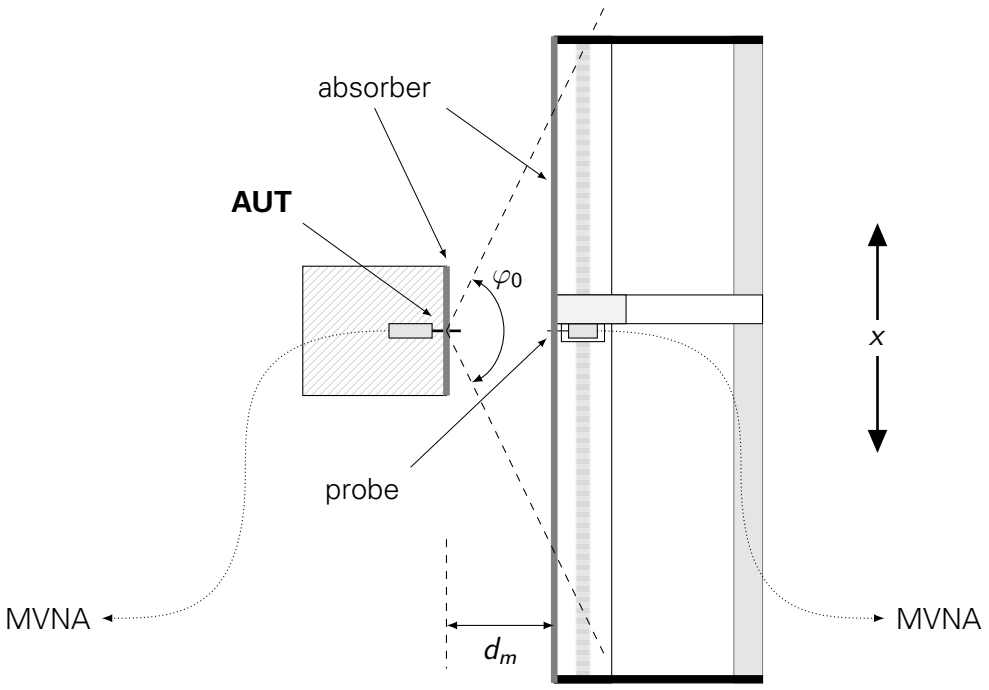

Figure 3.16: *Top view of the end-fire antenna measurement setup with $\varphi_0 = \varphi_{max}$ indicating the maximum horizontal scanning angle in the* **H** *-plane due to setup limitations*

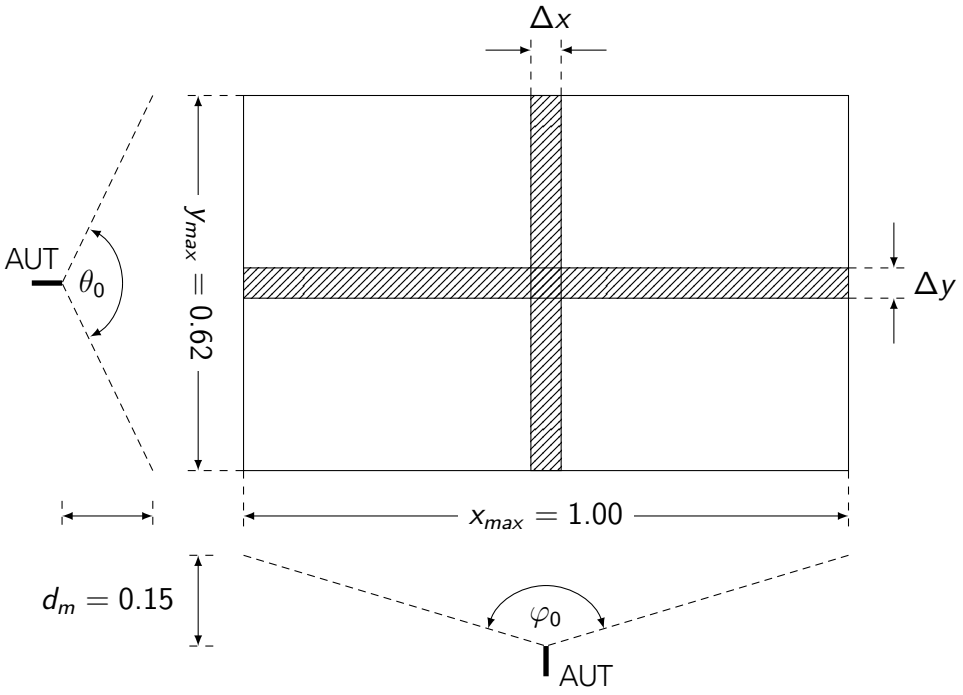

Figure 3.17: *Scanning area with dimensions in* m

The limitations for the horizontal and vertical movement of the scanning unit were $x_{max} = 1.00$ m and $y_{max} = 0.62$ m. Therefore the maximum scanning angles are

$$\theta_0 = \theta_{max} = 2 \cdot \arctan\left(\frac{0.50\ \text{m}}{0.15\ \text{m}}\right) = 2 \cdot 73.3^\circ = 146.6^\circ\ . \tag{3.26}$$

and

$$\varphi_0 = \varphi_{max} = 2 \cdot \arctan\left(\frac{0.31\ \text{m}}{0.15\ \text{m}}\right) = 2 \cdot 64.2^\circ = 128.4^\circ\ . \tag{3.27}$$

The end-fire antenna assembled and presented in this section was the same experimental NRD guide with a silicon dielectric rod with tapered ends studied in Section 2.4.3, besides that only one end was attached to a metal waveguide forming the transition with the other end left open acting as the radiating end of the antenna. The radiation patterns for four different frequencies were recorded: $f_1 = 75$ GHz, $f_2 = 85$ GHz, $f_3 = 95$ GHz and $f_4 = 105$ GHz. The scanning area is shown in *Figure 3.17*. The correct placement of the dielectric rod inside the waveguide could not be verified due to the experimental assembly

of the NRD guide.Therefore the center position was estimated and the scanning unit was programmed to scan the area $\pm$15mm from the center position ($\Delta x = \Delta y = 30$ mm) with a step size of $\Delta s = 3$ mm for both the **E** - and the **H** -plane measurement. For $f_3 = 85$ GHz a complete scan of the whole scanning area $x_{max} \times y_{max} = 1.00$ m $\times$ 0.62 m with the step size $\Delta s = \Delta s_x = \Delta s_y = 3$ mm was produced. The NSI2000 software delivers the data in cartesian coordinates which where later transformed into polar data in the post-processing. To get the correct radiation patterns of the NRD guide end-fire antenna, the characteristics of the open-ended rectangular waveguide acting as the probe also needed to be taken into account. Therefore the radiation patterns of a similar probe than the one used on the scanning unit were recorded.

To correct the uncompensated far-field patterns the *gain transfer method* was used. Thereby the unknown gain of the AUT is compared to a reference probe [40]. Two open-ended rectangular waveguides are considered to have the same radiation characteristic and therefore the radiation pattern of the probe was derived by measuring the radiation pattern of one using the second as the probe. The measured gain is the multiplied gain of both the receiving and the transceiving antenna, corresponding to the sum of the gains in dB [41]:

$$G_m^{\mathrm{dB}} = G_r^{\mathrm{dB}} + G_t^{\mathrm{dB}} \ , \tag{3.28}$$

with G_m being the measured gain, G_r the gain of the receiving antenna and G_t the gain of the transmitting antenna in dB. If both probes are considered to have the same radiation pattern with $G_{\mathrm{probe}} = G_r = G_t$, the probe gain can be calculated by

$$G_{\mathrm{probe}} = 0.5 \cdot G_{m|\mathrm{probe}} \ . \tag{3.29}$$

Now having obtained the gain of the probe, the AUT was calculated similarly:

$$G_{\mathrm{AUT}} = G_{m|\mathrm{AUT}} - 0.5 \cdot G_{m|\mathrm{probe}} \ . \tag{3.30}$$

Due to inaccuracies introduced by the measurement setup and the probes itself, the reference radiation pattern of the probe had to be post-processed in order to get feasible results. Therefore the mean value of $n = \pm 5$ consecutive values were taken to smoothen the radiation pattern. The effect can exemplarily

be seen in *Figure A.21* on page 112.

The comparison of the simulated and measured radiation patterns for $f_1 = 75$ GHz and $f_3 = 75$ GHz are illustrated in *Figures 3.18* and *3.19* (the radiation patterns for $f_4 = 105$ GHz are shown in *Figure A.20* on page 111). Before plotting the comparison figures, the raw measured data was processed in order to smooth the radiation pattern. Thereby the mean value of $n = \pm 5$ consecutive values was taken. The effect of smoothing can be seen in *Figure A.21* on page 112 for the probe radation pattern.

Evaluating the **H** -plane radiation pattern in *Figure 3.18*, corresponding to the horizontal movement of the scanning unit in the x -direction, reveals the asymmetric placement of the dielectric rod in the NRD guide. In spite of this bad excitation the measured antenna radiation patterns did not show ripples even with the discussed measurement inaccuracies. The comparison of the **E** -plane radiation pattern in *Figure 3.19* also shows the asymmetric position of the dielectric rod and the NRD guide as a whole. However the measured data for the **E** -plane shown in the figure is more deformed than for the **H** -plane. This could be caused by the assembly of the experimental NRD guide and inaccuracies of the measurement setup. The contour plot of the whole scanning area for $f_2 = 85$ GHz is plotted in *Figure 3.20*. From this plot the asymmetryic placement with bad excitation can be seen as well, compared to the tridimensional plot in *Figure 3.12b*.

Other causes of error than the ones discussed in Section 2.4.3 for the experimental NRD guide are possible reflections due to non-optimal arrangement of the absorbers around the AUT and the measurement probe and the error introduced by the gain transfer method (the two reference probes were not exactly the same).

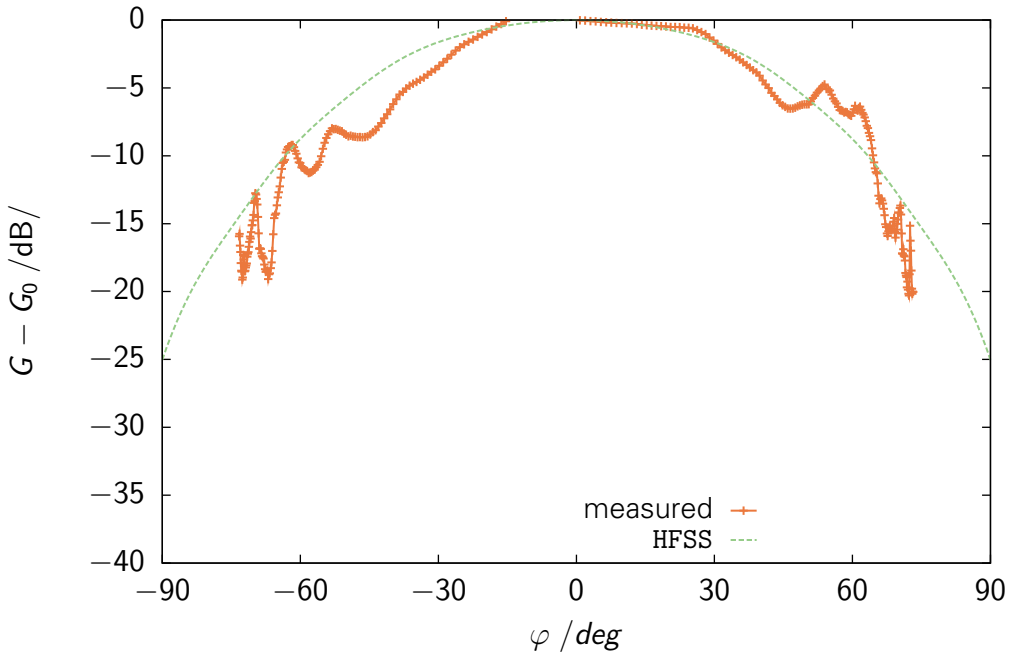

(a) $f_1 = 75$ GHz

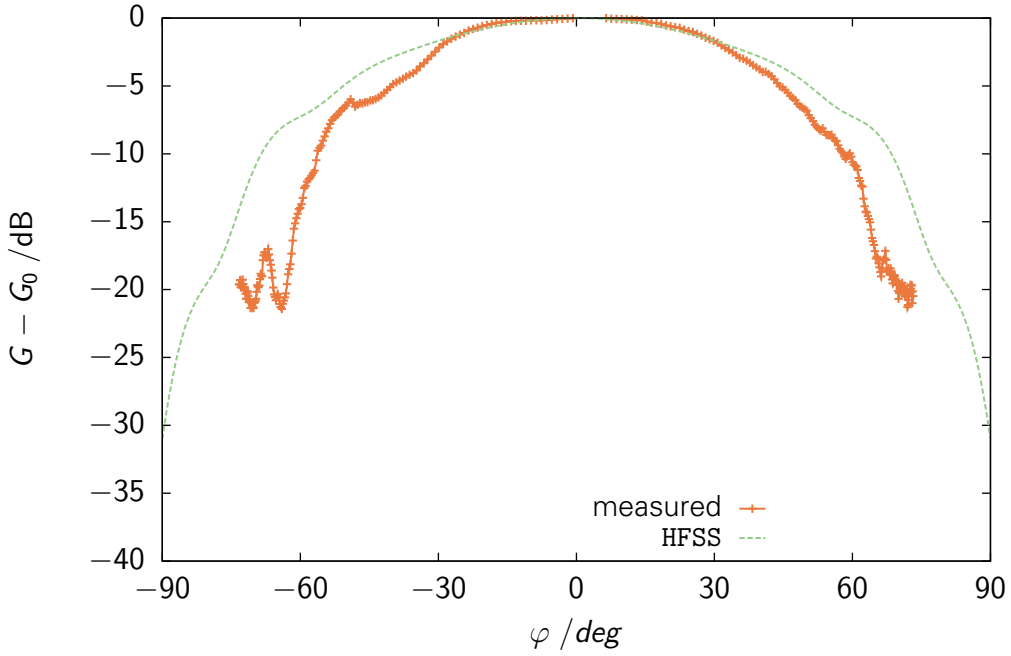

(b) $f_3 = 95$ GHz

Figure 3.18: *Comparison of the simulated and measured far-field* **H** *-plane radiation patterns of the AUT*

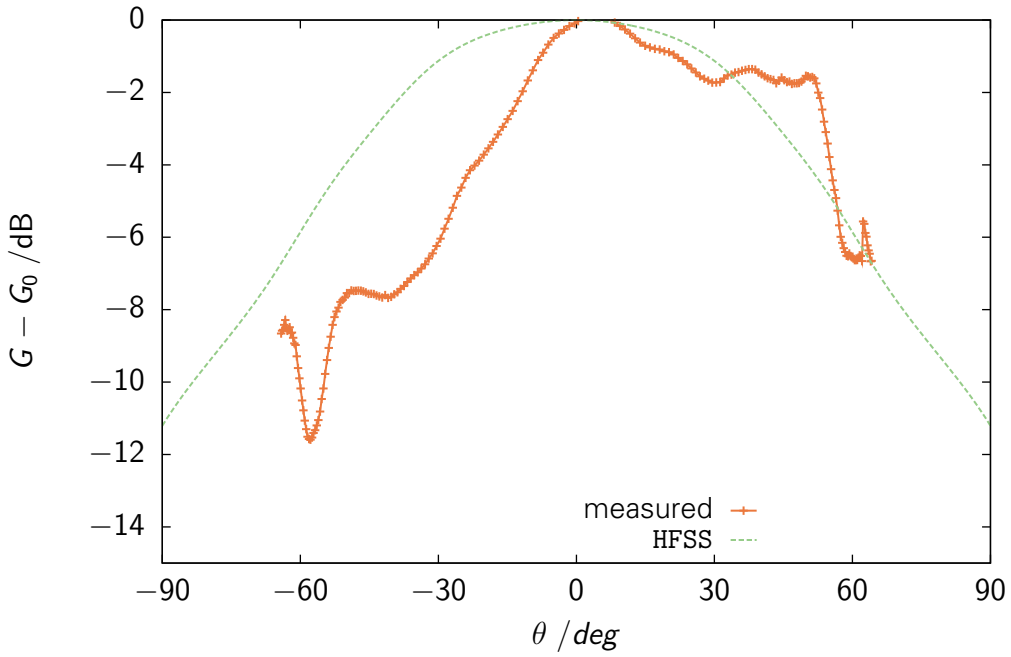

(a) $f_1 = 75$ GHz

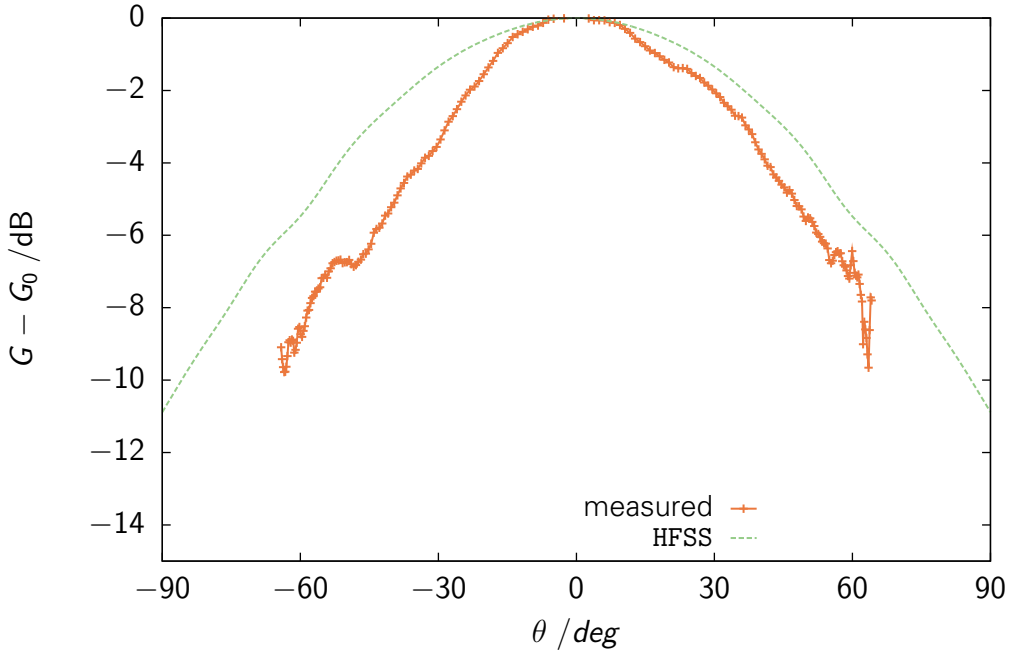

(b) $f_3 = 95$ GHz

Figure 3.19: *Comparison of the simulated and measured far-field* **E** *-plane radiation patterns of the AUT*

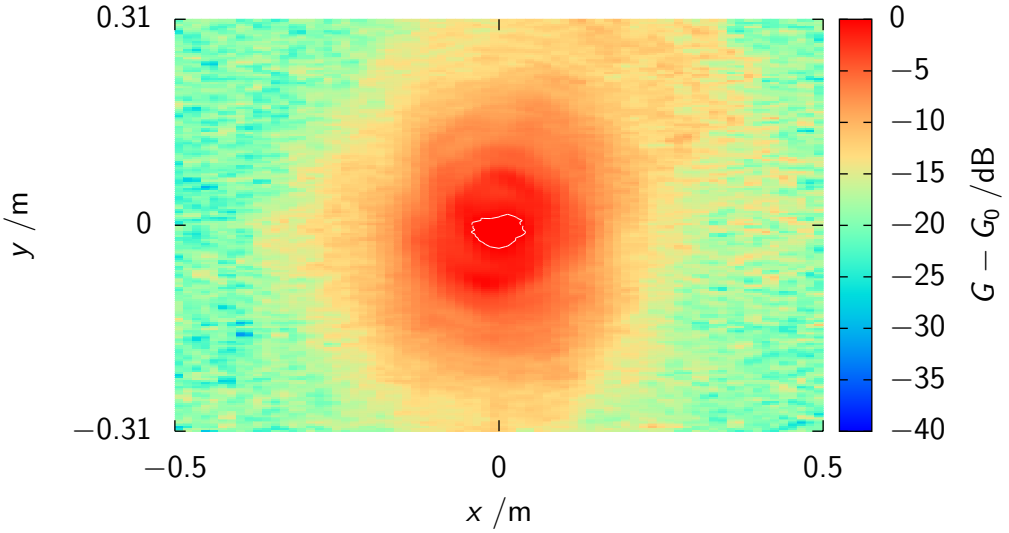

Figure 3.20: *2D contour plot of the measured radiation pattern for* $f_2 = 85$ GHz

3.3 NRD guide leaky-wave antennas

There have been different approaches on uniform leaky-wave antennas based on NRD guides. However, this thesis is focused on NRD guides working in the slow-wave region and therefore only periodic leaky-wave antennas were studied.

One method is to introduce periodic strips on the dielectric rod [42]. As described in Section 3.1.2, these discontinuities change the propagation characteristic to make the NRD guide leaky. Due to the non-radiating property of the area between the metal plates above the dielectric rod, the height of these metal plates need to be reduced in order to let the leaked wave propagate. Another method is to alter the properties of the sidewalls by adding a special texture onto it to turn it into a high impedance surface (see Section 3.1.3). Thus electromagnetic waves are able to propagate away from the dielectric rod. In this Section a concept for NRD guide period leaky-wave antennas using high impedance surfaces is presented. HIS developed in [39] can be modulated by an external voltage and therefor the antenna can be switched *on* and *off* for different frequencies.

3.3.1 Design

To make the NRD guide end-fire antenna discussed in the previous Section leaky, discontinuities were placed along the waveguide. For this concept of a leaky-wave antenna two kinds of discontinuities shown in *Figure 3.21* were chosen: (a) PEC strips and (a) PEC stubs placed periodically on top of the dielectric rod. The discontinuities were modeled as flat PEC planes placed on top of the dielectric rod. In order to radiate out of the waveguide along the structure, the parallel metal plates needed to be modified to let the electromagnetic wave propagate in that region. The HIS structure is modeled in the HFSS simulation as PMC. The design of the original concept is shown in *Figure 3.22*. The schematic simulation model of the conceptual leaky-wave antenna is illustrated in *Figure 3.23*. Thereby PEC elements are positioned periodically above the dielectric rod. However, in this concept the PEC elements are *hanging in the air* above the dielectric, which is difficult to manufacture. It would be easier to realize this concept by putting the PEC elements directly on top of the dielectric rod, with the offset parameter o equal to zero.

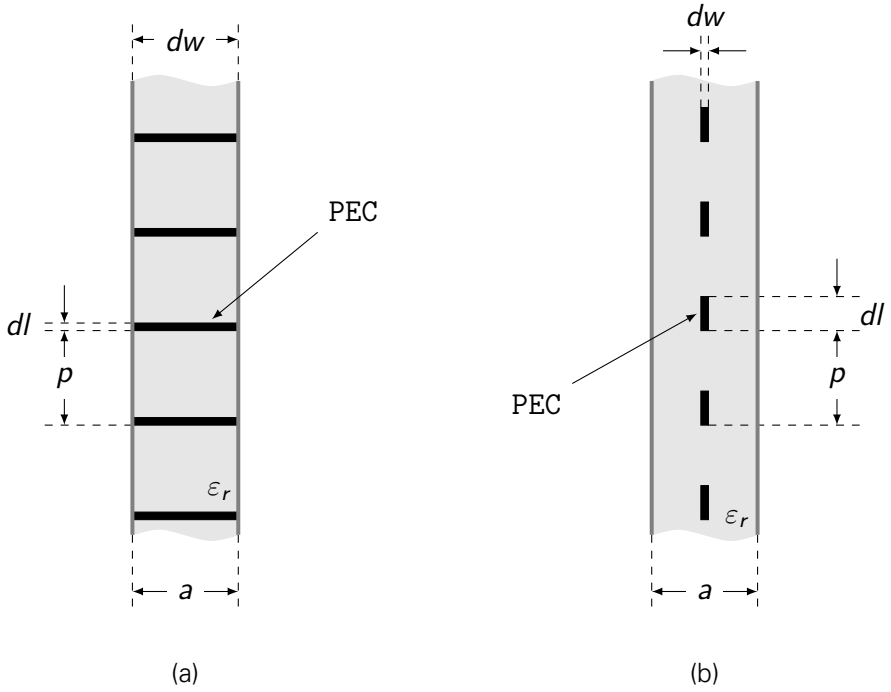

Figure 3.21: *Top view of the NRD guide with discontinuities separated by period* p *on top of the dielectric: (a) printed strips with* $dw = a$ *and (b) printed stubs with* $dw < a$

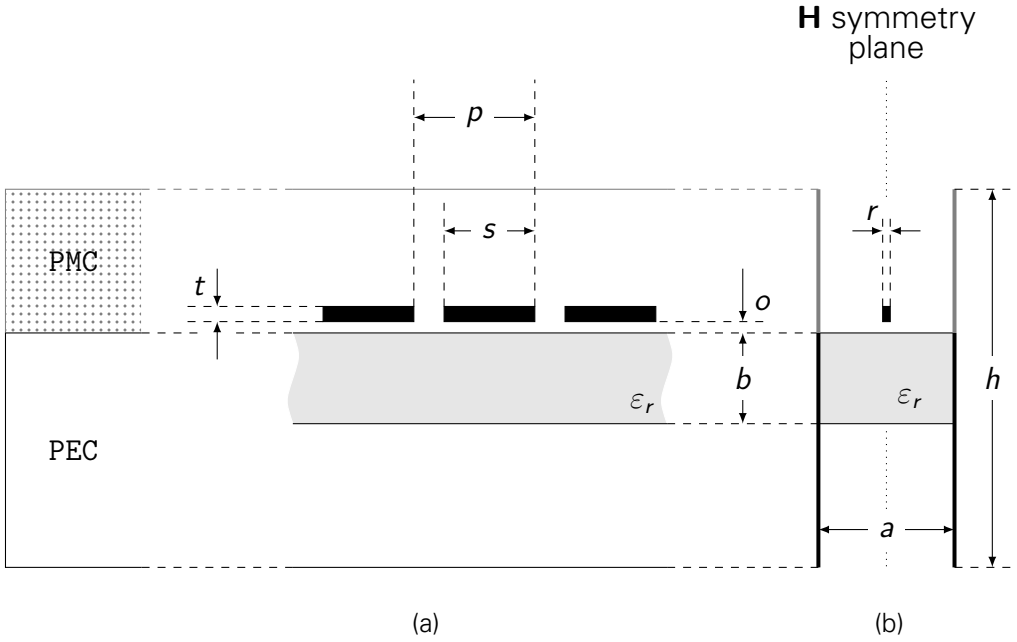

Figure 3.22: *Concept of NRD guide leaky-wave antenna: (a) side view and (b) cross-section with dimensions in* mm $a = 1.4$, $b = 0.5$, $s = 1.6$, $t = 0.25$, $p = 2$, $r = 0.01$ *and* $o = 0.3$

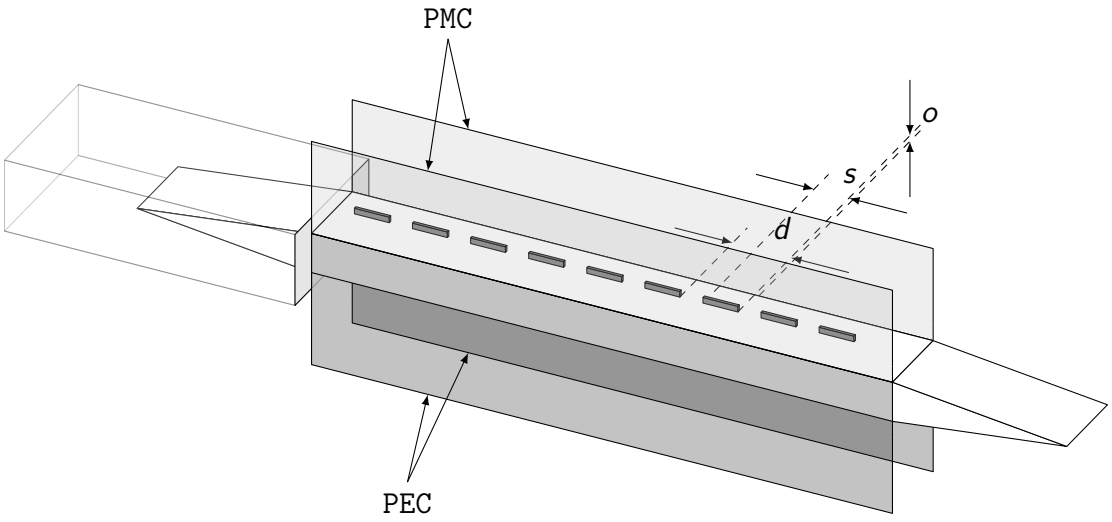

Figure 3.23: *Concept of periodic leaky-wave NRD guide antennas with PEC discontinuities loaded on the dielectric rod separated by distance p*

To study the concept for a leaky-wave antenna based on the studied NRD guide with HIS surfaces on the inside of the metal plates, the period $p = 2$ mm was chosen as the length of the unit cell of the leaky-wave antenna. The height of the parallel plates was set to be $h = 10$ mm, whereby PMC boundary conditions were applied to the plates above the dielectric rod on the side were the discontinuities were placed. The length of the NRD guide appointed to be $l = 20$ mm, corresponding to $n = l/p - 1 = 9$ placed discontinuities. The dispersion characteristic $|\beta_{-1}/k_0| - f$ is shown in *Figure 3.24*. The center frequency at which broadside radiation occurs ($\beta_{-1|c} = 0$) for $p = 2$ mm then is $f_c \approx 96.7$ GHz. The antenna structure is leaky in the frequency range from $\sim$ 85 to 110 GHz with $|\beta_{-1}| < k_0$. For $f < f_c$ the antenna has backfire radiation $\theta_m < 0°$, whereas for $f > f_c$ the beam angle is $\theta_m > 0°$.

[43]

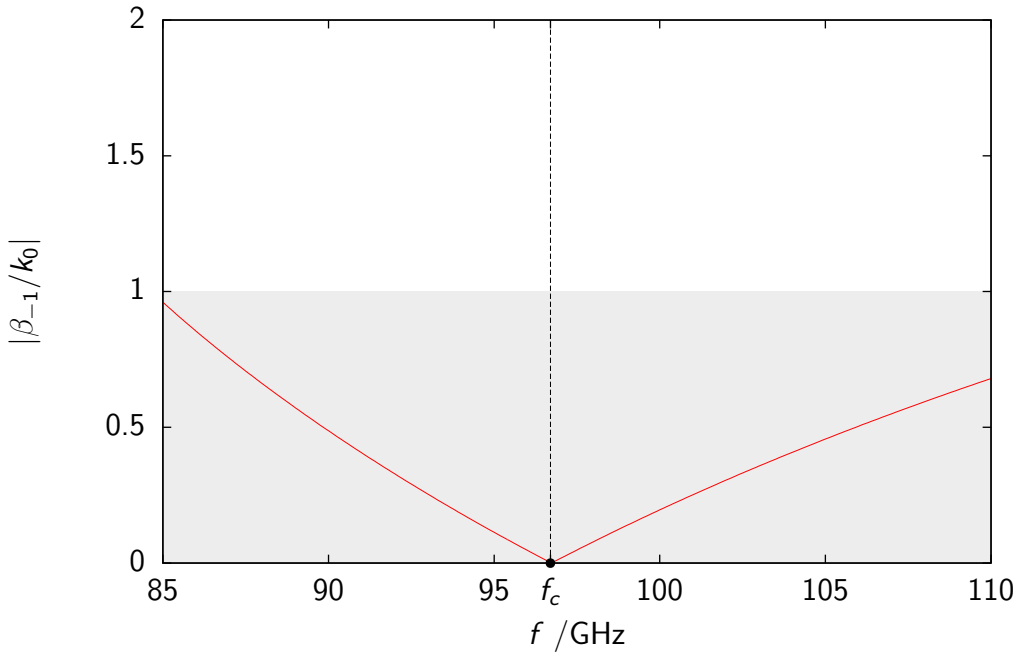

Figure 3.24: *Calculated dispersion characteristics $\beta_{-1}/k_0 - f$ of the classical NRD guide with $a = d$ and dimensions in* mm $a = 1.4$ *and* $b = 0.5$, $f_c \approx 96.7$ GHz

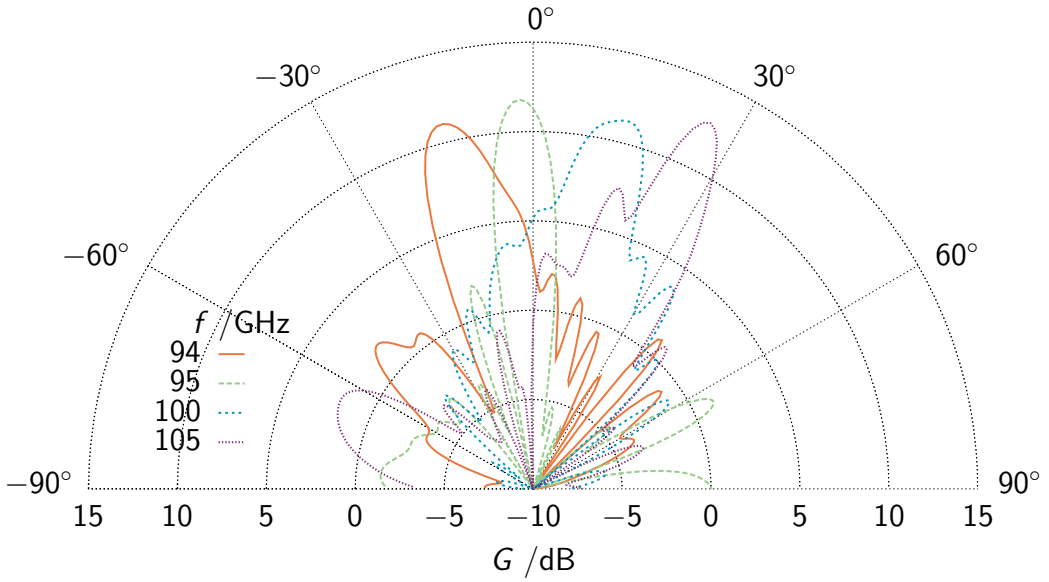

Figure 3.25: E *-plane radiation pattern of an NRD guide leaky-wave antenna with discontinuities of type (b) shown in Figure 3.21b with dimensions in* mm $a = 1.4$, $b = 0.5$, $p = 2$, $dl = 0.5$ *and* $dw = 0.1$

3.3.2 Simulation results

The **E** -plane radiation pattern for the original leaky-wave antenna concept is illustrated in *Figure A.22* (with dimensions of the discontinuities given in *Figure 3.22*). This concept shows good radiation characteristics for the frequency range from 85 to 110 GHz with the gain of the side lobes being at least 10 dB less than the gain of the main lobe. However, as mentioned before, this concept is not easy to assemble with discontinuities *hanging in the air*. Placing the PEC elements directly on the dielectric rod, $o = 0$, while leaving the other dimensions untouched, did not deliver feasable radiation characteristics. Shortening the length of the stubs to $s = 0.5$ mm leads to the **E** -plane radiation pattern given in *Figure A.23*. The beam angle θ_m of the main lobe is shifted compared to the aforementioned setup and the beam form is distorted. Overall, the concept of placing these discontinuities directly on the dielectric rod did not prove to be a a good method for leaky-wave antennas based on the NRD guide.

Modeling the discontinuities not as PEC elements as described in *Figure 3.22*, but as flat PEC surfaces on top of the dielectric (considered as *printed* on the dielectric material, with dimensions in mm $a = 1.4$, $b = 0.5$, $p = 2$, $dl = 0.5$ and $dw = 0.1$), delivers the **E** -plane radiation pattern illustrated in *Figure 3.25* with good radiation characteristics in the frequency range from 95 to 105 GHz. This

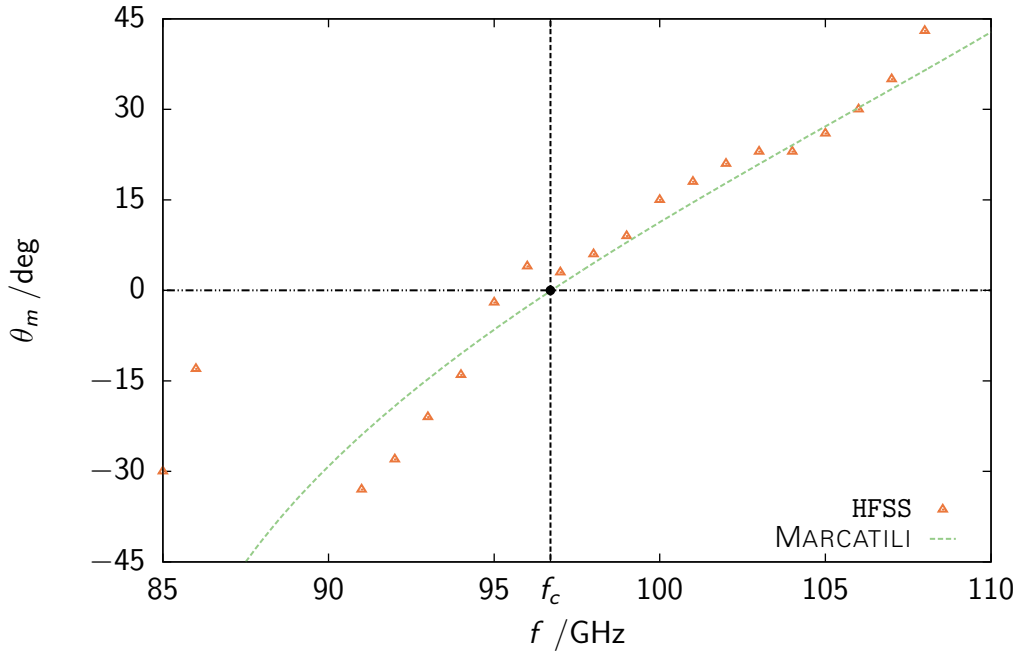

Figure 3.26: *beam angle θ_m of an NRD guide leaky-wave antenna with discontinuities of type (b) shown in Figure 3.21b on page 78 with dimensions in* mm *$a = 1.4$, $b = 0.5$, $p = 2$, $dl = 0.5$ and $dw = 0.1$*

method proved to be more suitable for a leaky-wave antenna than the aforementioned method with PEC elements. In *Figure 3.26* the beam angle θ_m of the simulation results is compared to the calculated beam angle. The calculated beam angle was based on MARCATILI's method extended in Section 2.3, which was not completely matching the simulation results. This, and the change of the propagation characteristics of the NRD guide by the discontinuities, explains the shift of the beam angle. The maximum gain G_0^{dB} of the main lobe is shown in *Figure 3.27* However, within this concept the size and shape of the discontinuities is crucial. For dimensions in mm $dw = 0.1$ and 0.5 the developed leaky-wave antenna offers interesting radiation characteristics. Changing the size of the stubs as in *Figure A.25*, the resulting radiation pattern for some values makes the concept unfeasible. The effect of the stubs (or strips) shape and size on the radiating behaviour still needs to be investigated. The tridimensional radiation pattern of the stub loaded NRD guide leaky-wave antenna in the frequency range from 92 to 109 GHz are shown in *Figures 3.28* to *3.30*.

There are approaches to avoid the high reflections (the reflection coefficient s_{11}^{dB} for the discussed leaky-wave antenna is shown in *Figure A.24*) in the frequency range close to broadside radiation by introducing *double strips* [35]. It

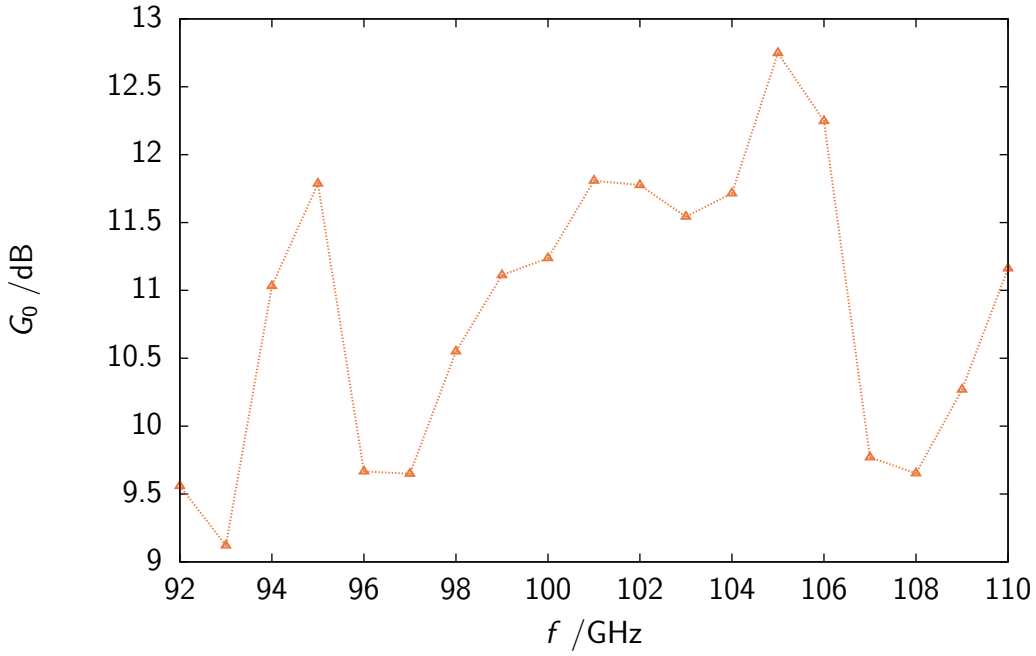

Figure 3.27: *Maximum gain G_0^{dB} of the main lobe of an NRD guide leaky-wave antenna with discontinuities of type (b) shown in Figure 3.21b on page 78 with dimensions in* mm *$a = 1.4$, $b = 0.5$, $p = 2$, $dl = 0.5$ and $dw = 0.1$*

has to be studied if this is also applicable for this kind of leaky-wave antenna.

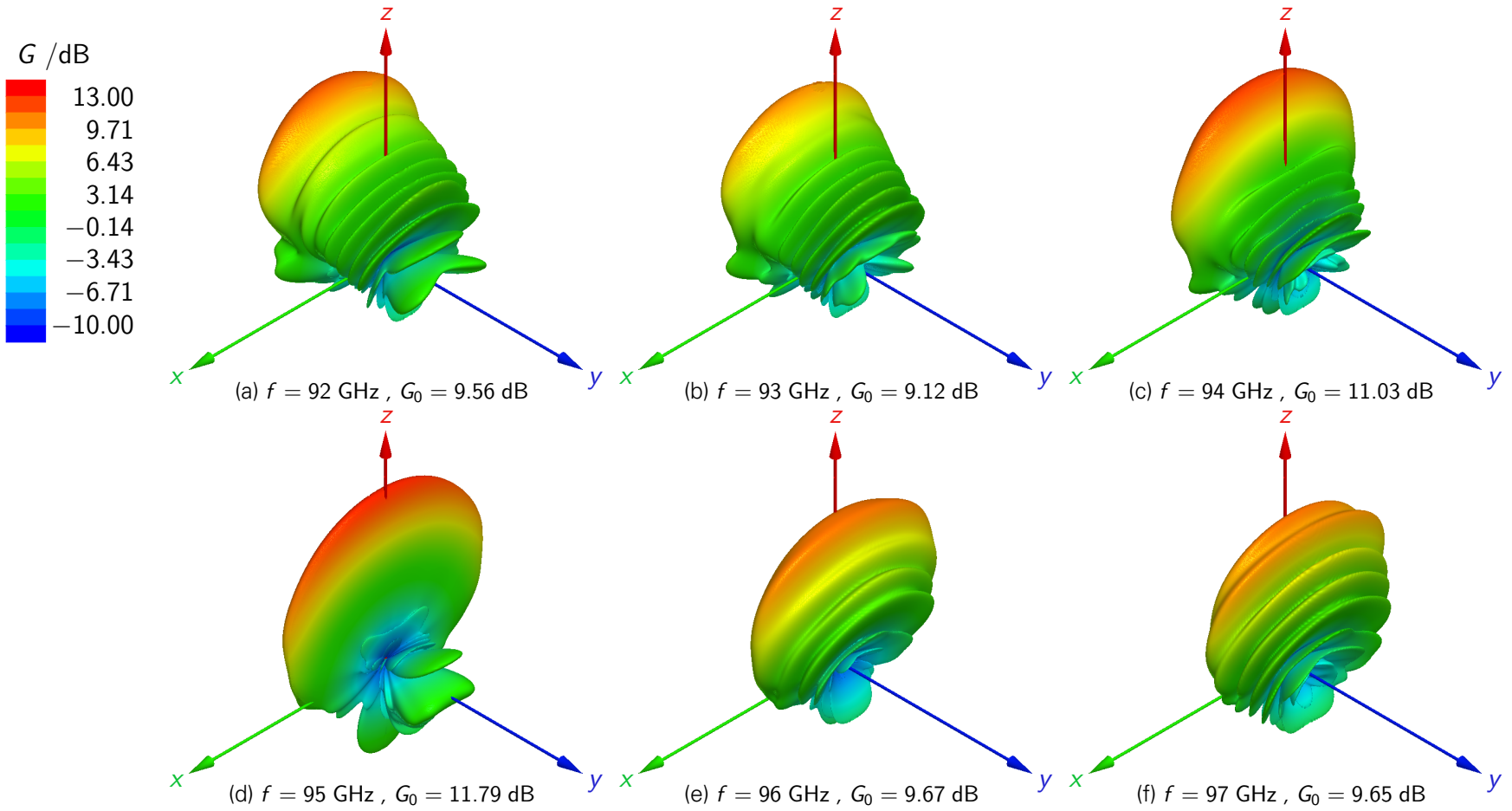

Figure 3.28: *Tridimensional radiation pattern of the NRD guide leaky-wave antenna with discontinuities shown in* Figure 3.21b *for the frequency range from (a)* 92 *to (f)* 97 GHz *with dimensions in* mm $a = 1.4$, $b = 0.5$, $p = 2$, $dl = 0.5$ *and* $dw = 0.1$

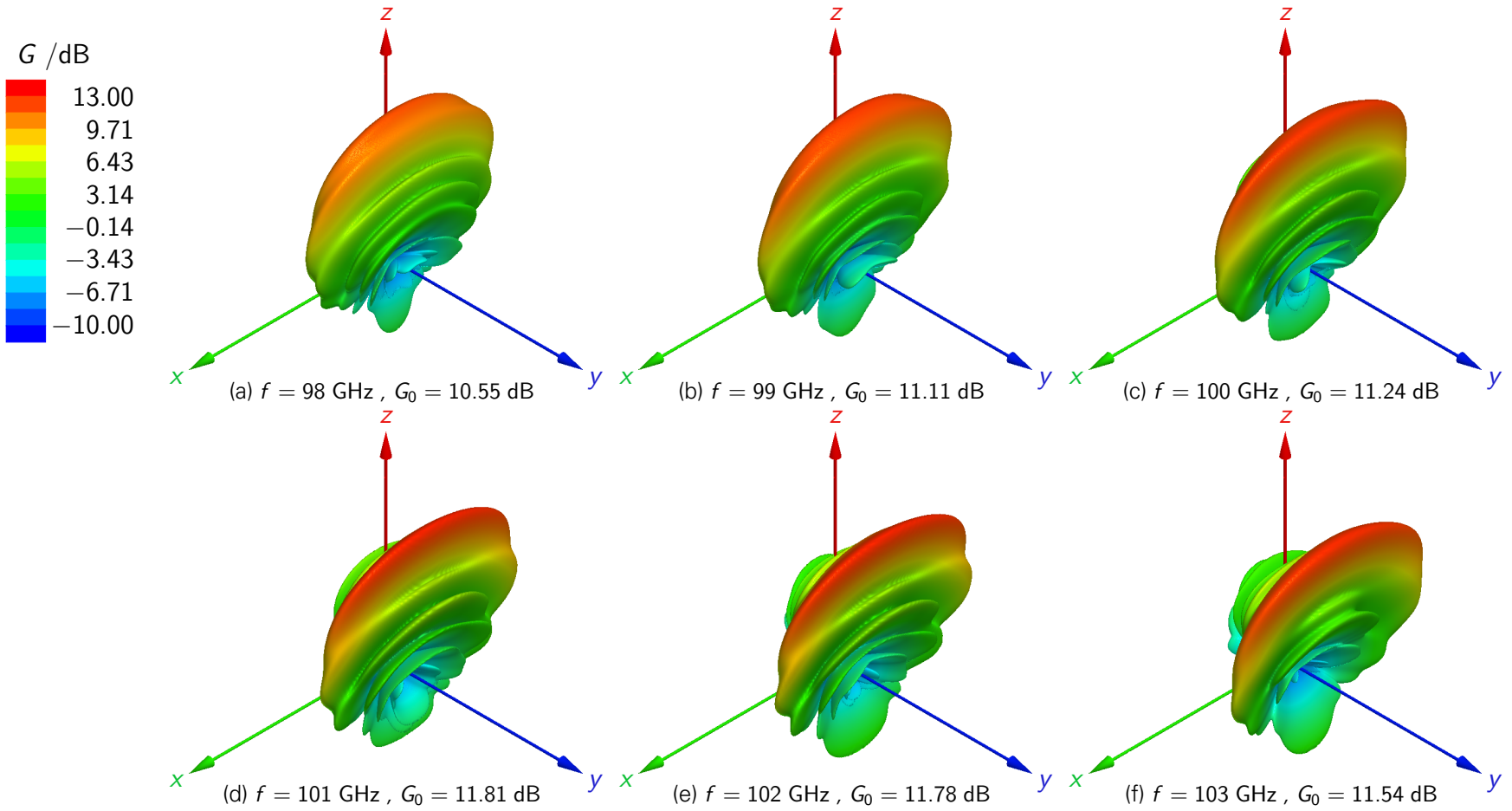

Figure 3.29: *Tridimensional radiation pattern of the NRD guide leaky-wave antenna with discontinuities shown in* Figure 3.21b *for the frequency range from (a)* 98 *to (f)* 103 GHz *with dimensions in* mm $a = 1.4$, $b = 0.5$, $p = 2$, $dl = 0.5$ *and* $dw = 0.1$

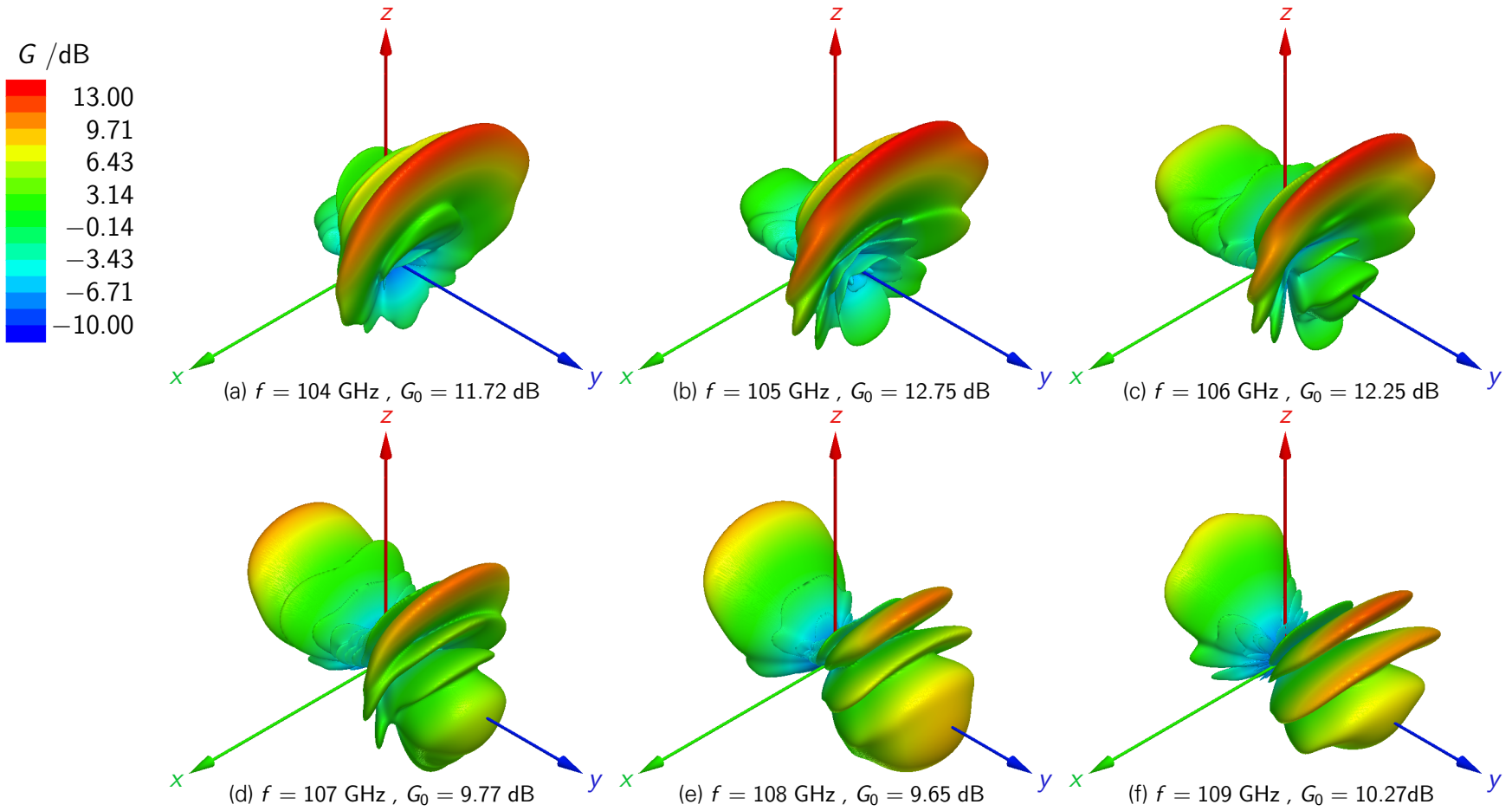

Figure 3.30: *Tridimensional radiation pattern of the NRD guide leaky-wave antenna with discontinuities shown in* Figure 3.21b *for the frequency range from (a)* 104 *to (f)* 109 GHz *with dimensions in* mm $a = 1.4$, $b = 0.5$, $p = 2$, $dl = 0.5$ *and* $dw = 0.1$

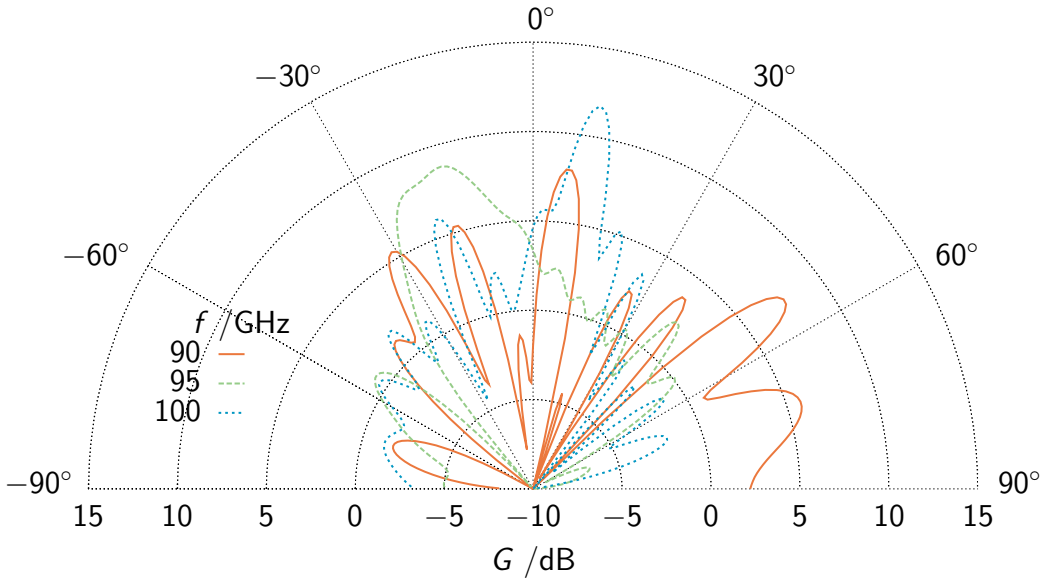

Figure 3.31: **E** *-plane radiation pattern of an NRD guide leaky-wave antenna with strip discontinuities of type (a) as shown in Figure 3.21a having the dimensions in* mm $a = d = 1.4$, $b = 0.5$, $dl = 0.1$ *and* $p = 2$

The **E** -plane radiation pattern for the NRD guide leaky-wave antenna with strips as discontinuities as shown in *Figure 3.21a* is illustrated in *Figure 3.31* for in GHz $f_1 = 90$, $f_2 = 95$ and $f_3 = 100$. It can be seen that for the chosen parameters this type of discontinuities is not delivering appropriate radiation characteristics. However, the effect of the dimension of the strip width *dl* needs to be studied more thoroughly in order to judge about the feasibility of this kind of discontinuity for the proposed leaky-wave antenna concept.

4 CONCLUSIONS

The extension of MARCATILI's method to be used to analyze the propagation constant of the primary *LSM* mode of the NRD guide developed in this thesis offers an easy way to study the propagation characteristics of the NRD guide. Its suitability for the design of periodic leaky-wave antennas based on NRD guides was proven. However, considering the simulation results to be numerically correct, unlike for dielectric waveguides the calculated propagation constant does not converge totally to the one obtained from simulating the structure but stays below that, depending on the geometry of the dielectric rod. The reason for that, except of a possible error introduced for instance by converging problems occuring within the simulation, is the assumption that the main electric field component is the E_y component and the E_x field component is neglected.

The presented transition from standard metal waveguide to NRD guide marks a suitable and easy to manufacture way to connect both waveguide types. Aside from the difficulties at the measurement setup to verify the suitability of the transition, the measurement of the experimental NRD guide showed its potential to be used within integrated circuits. Though, in order to achieve both better reflection and transmission characteristics the NRD guide needs to be assembled more thoroughly. Especially the position of the dielectric rod between the metal plates and the placement of the taper section in the standard metal waveguide has to be optimized in order to get more reliable measurement results. As the same prototype as for the transition was used for the NRD guide end-fire antenna, the same problems due to the experimental setup occured for the measurement of the radiation pattern. However, the developed end-fire antenna offers interesting applications withing the millimeter wave area.

As the studied NRD guide is operating in the slow-wave region, introducing discontinuities along the dielectric rod causes the antenna to become leaky. The

presented concept of an NRD guide, where PMC boundary conditions were assigned to the inner surface of the parallel plates and PEC discontinuities were placed above the dielectric rod, describes a promising design for NRD guide periodic leaky-wave antennas. As the simulation results obtained, certainly not every type of discontinuity is suitable for this kind of leaky-wave antenna.

5 OUTLOOK

In order to verify the suitability of the presented transition more accurately, a more precise prototype needs to be manufactured and measured. A way has to be found to place the rod exactly in the right position, which is difficult to achieve by assembling the prototype by hand. A possible way is to prefabricate proper spacers so that the dielectric rod is both placed symmetrical between the metal plates and exactly in the right position inside the metal waveguide. For the classical NRD guide, where the dielectric rod is placed and attached directly between the metal plates, a prototype with two tapered sections of the dielectric rod can be microfabricated in an easy way to prove the capabilities of the studied transition. As the developed NRD guide end-fire antenna is based on the developed transition, the same arrangements apply for the more accurate verification process of its radiating characteristics. Furthermore the measurement setup has to be enhanced and probes with known radiation characteristics have to be used.

The developed extended MARCATILI's method proved to be a suitable method to estimate the propagation constant of the NRD guide mode of interest in order to realize the proposed NRD guide leaky-wave antennas. The HIS used to model PMC in real appliactions can be easily placed on the inner surface of the metal plates. To verify the presented concept the prototype has to be microfabricated as whole, with the discontinuities placed on top of the dielectric rod. Considering the effect the discontinuities have on the propagation characteristics and therefore the radiation characteristics, further research on feasible discontinuities design needs to be done.

A FIGURES

A.1 NON-RADIATING DIELECTRIC WAVEGUIDES

A.1.1 NRD guide model

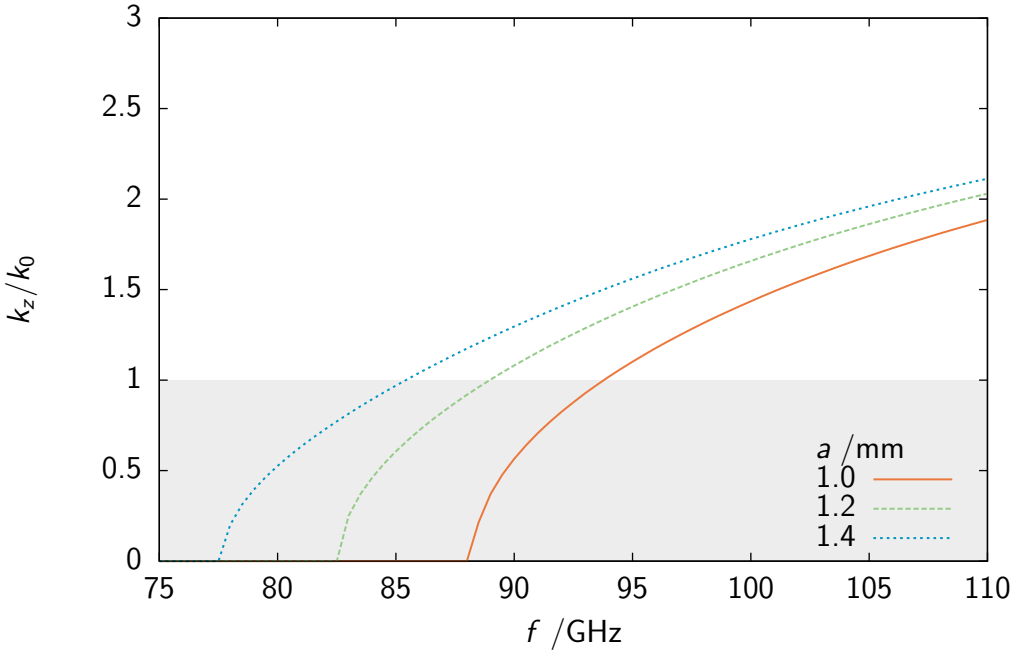

(a) $b = 0.6$ mm

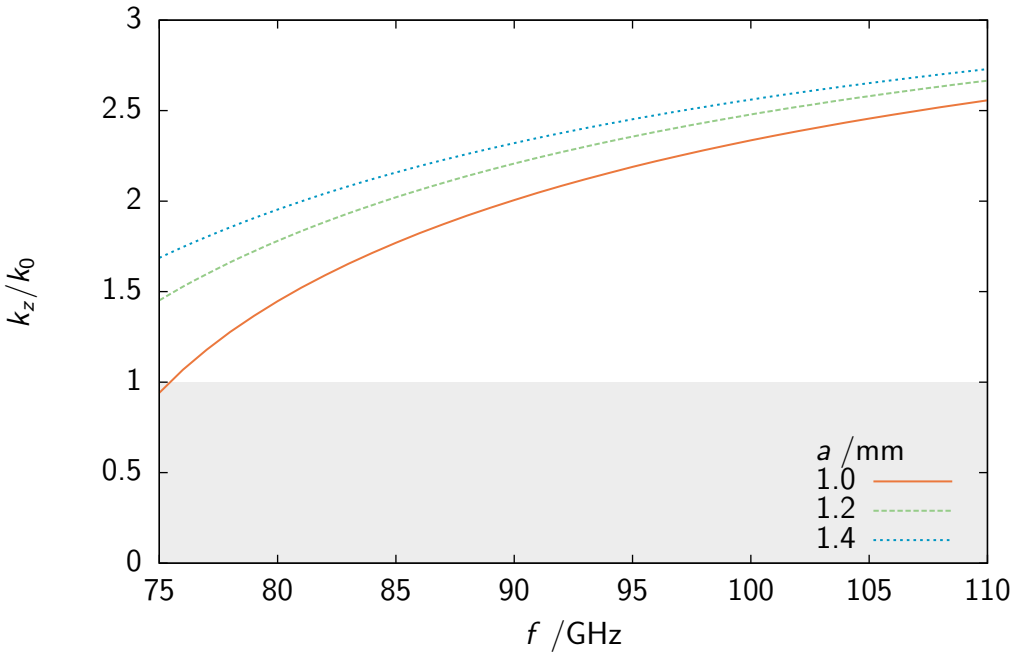

(b) $b = 0.7$ mm

Figure A.1: *Simulation results of k_z/k_0 of the classical NRD guide with $a = d$*

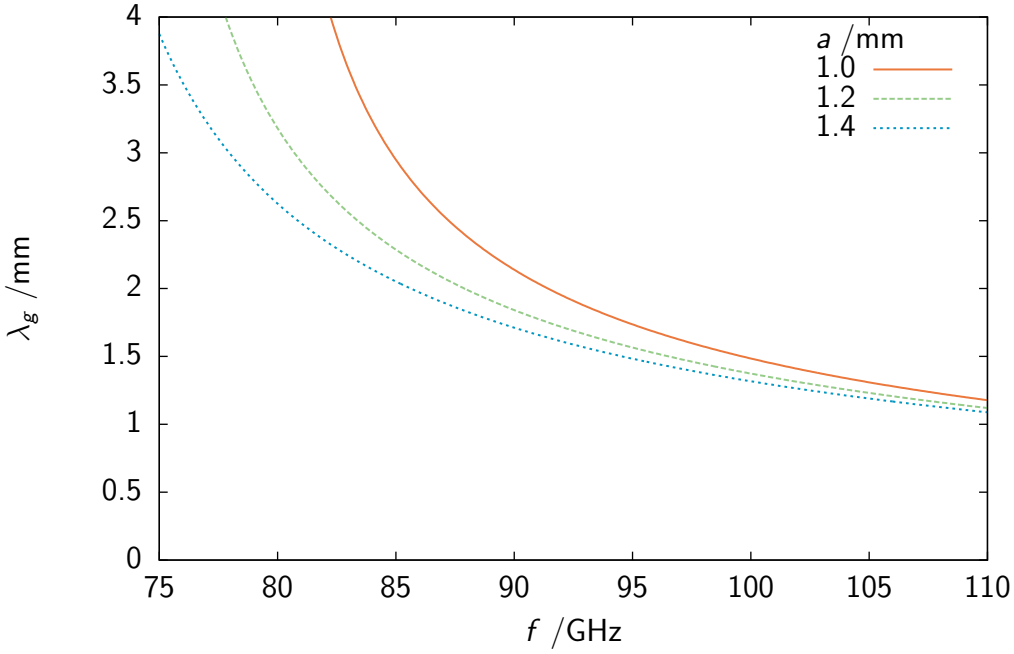

(a) $b = 0.6$ mm

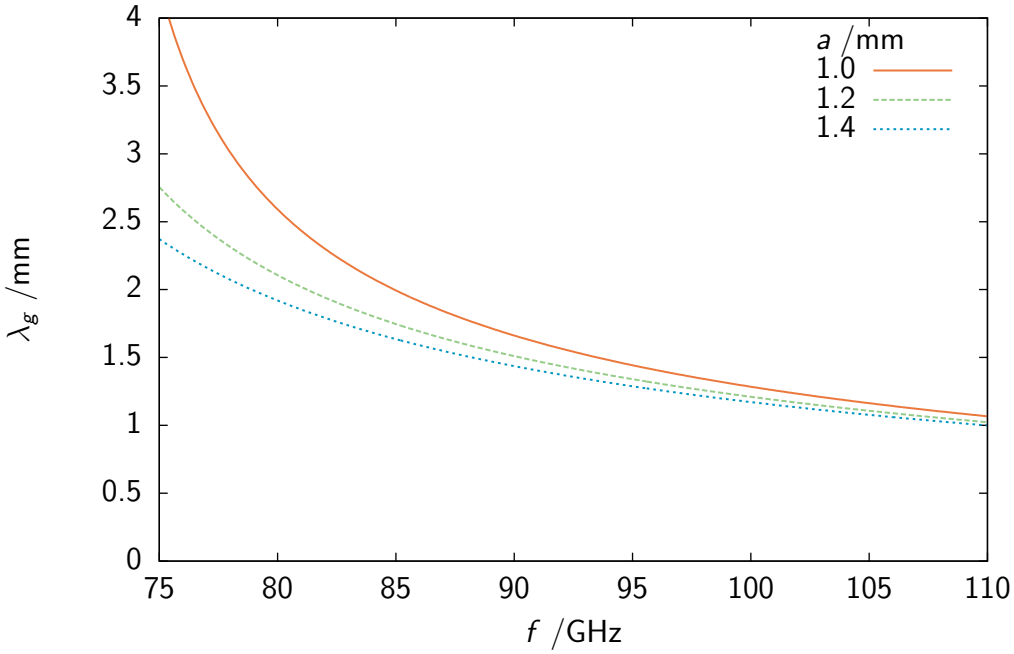

(b) $b = 0.7$ mm

Figure A.2: *Simulation results of the guide wavelength λ_g of the classical NRD guide $a = d$*

A.1.2 MARCATILI's method for non-radiating dielectric waveguides

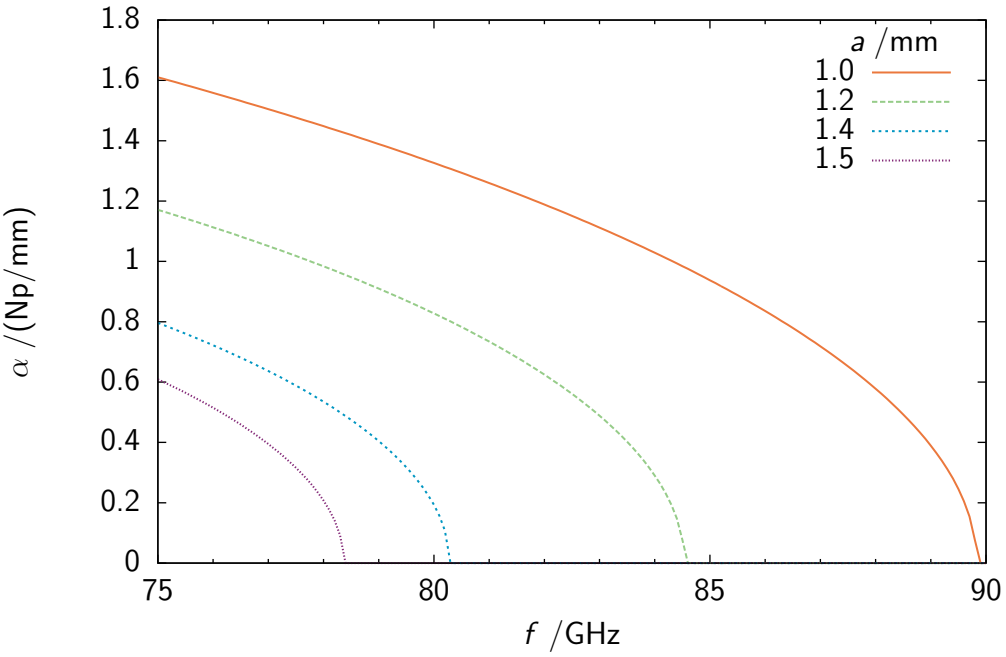

Figure A.3: *Calculated attenuation constant α of the classical NRD guide with $a = d$ for $b = 0.5$ mm*

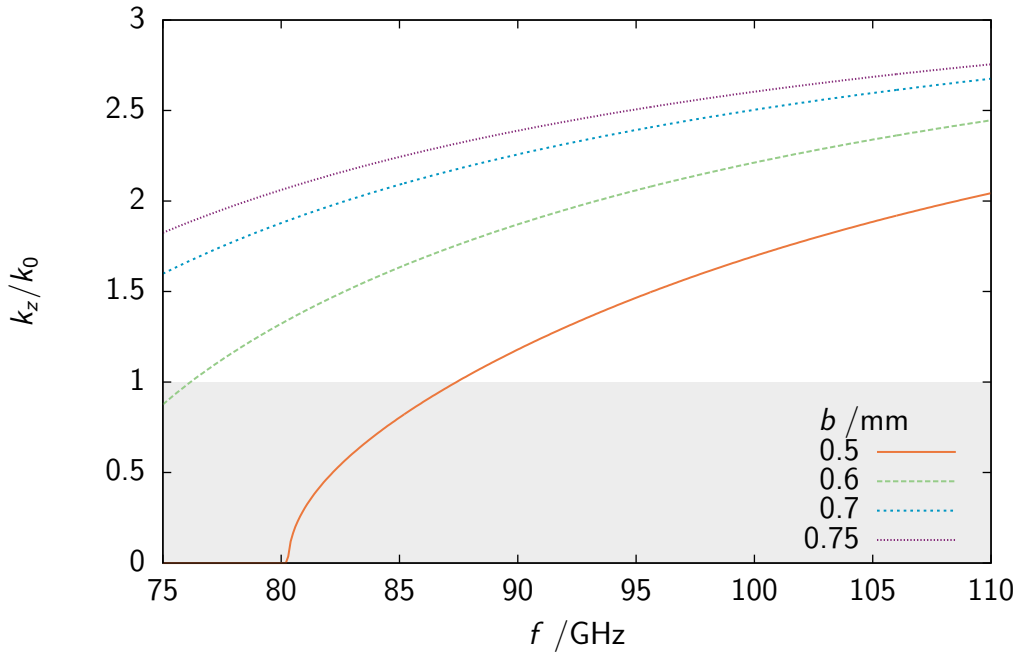

Figure A.4: *Calculated dispersion diagram $k_z/k_0 - f$ of the classical NRD guide with $a = d = 1.4$ mm for different values of the height of the dielectric rod b*

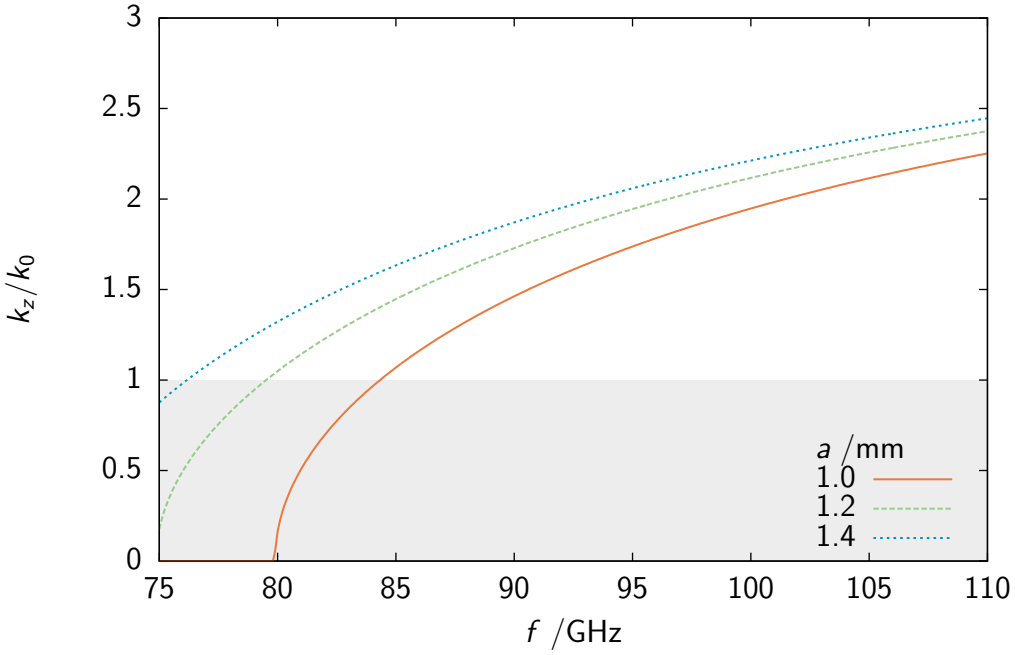

(a) $b = 0.6$ mm

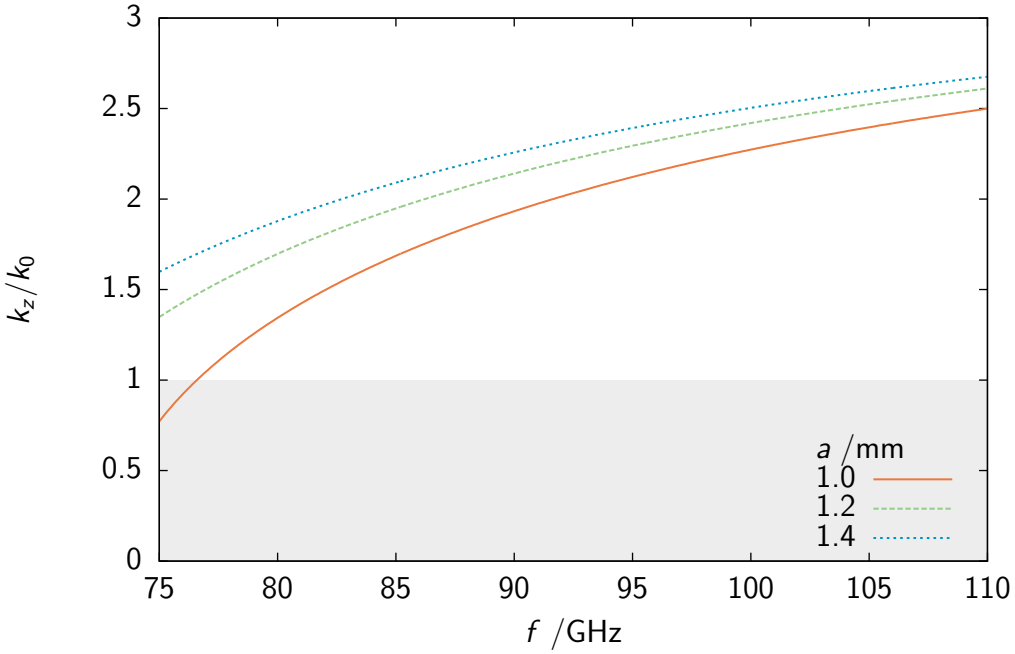

(b) $b = 0.7$ mm

Figure A.5: *Calculated dispersion diagram $k_z/k_0 - f$ of the classical NRD guide with $a = d$*

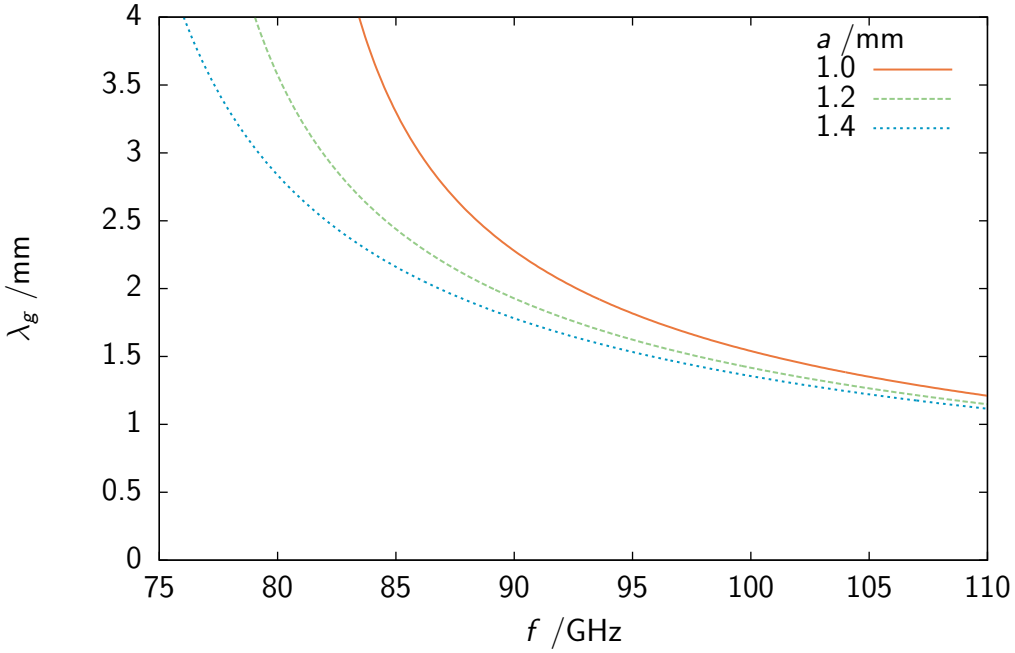

(a) $b = 0.6$ mm

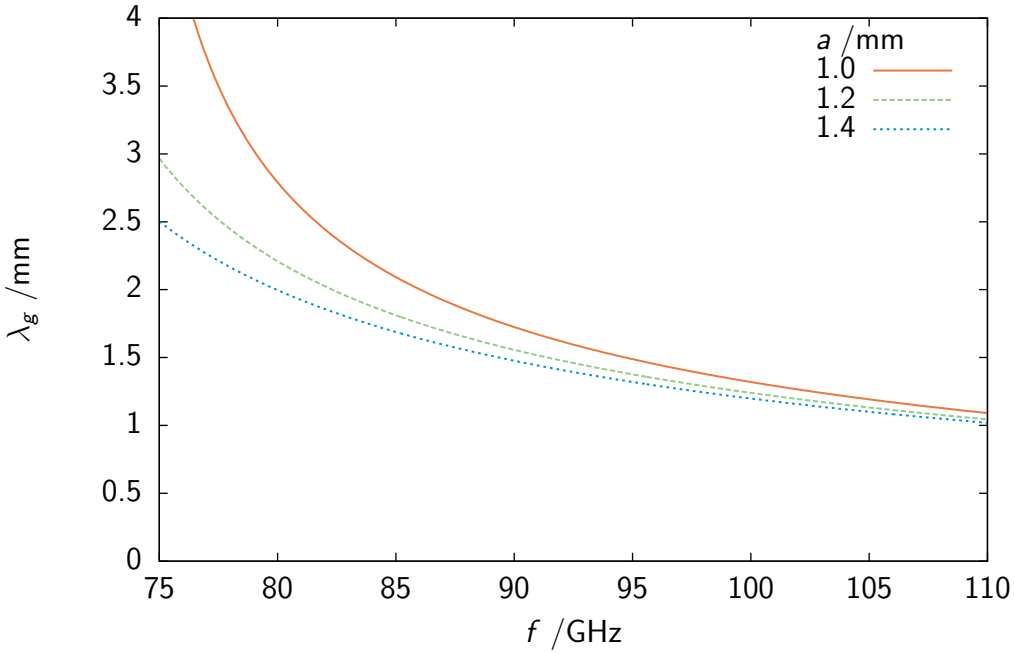

(b) $b = 0.7$ mm

Figure A.6: *Calculated guide wavelength λ_g of the classical NRD guide with $a = d$*

A.1.3 Standard metal waveguide to NRD guide transition

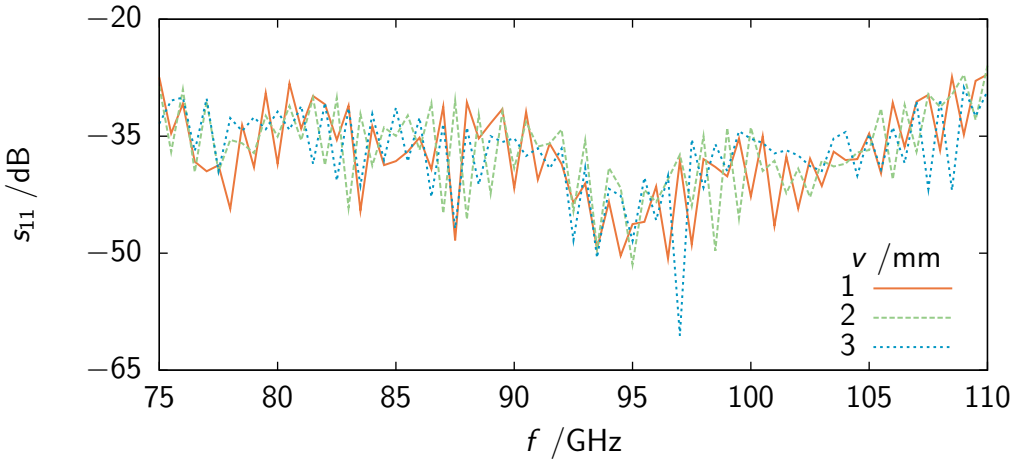

(a) $h = 3$ mm

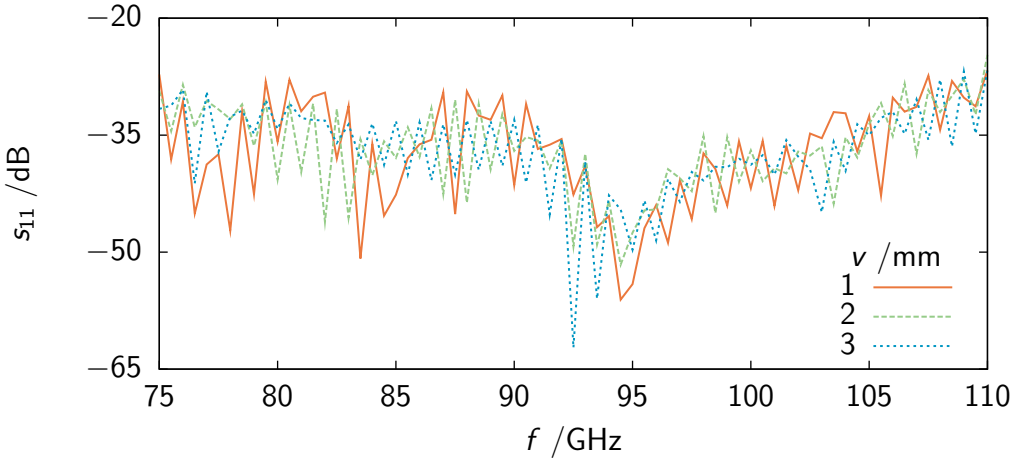

(b) $h = 5$ mm

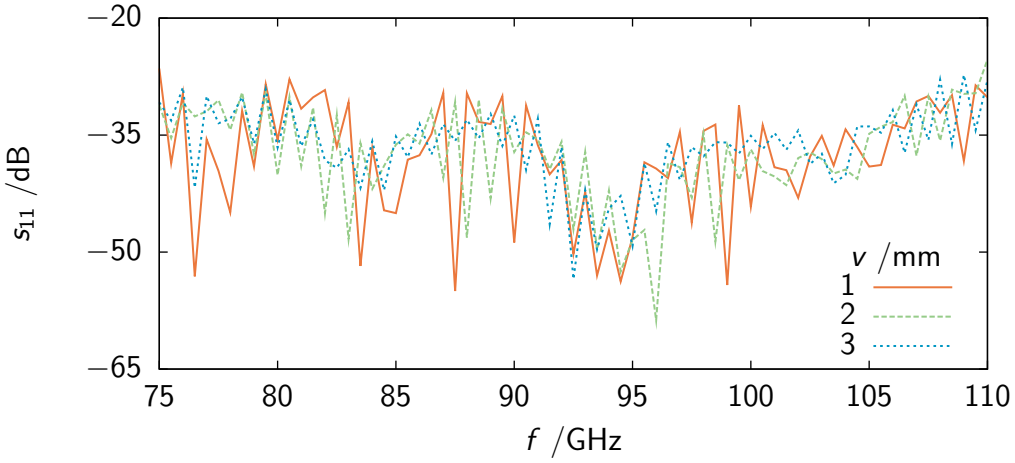

(c) $h = 7$ mm

Figure A.7: *Reflection coefficient s_{11}^{dB} of transition type (I) for varied transition length v*

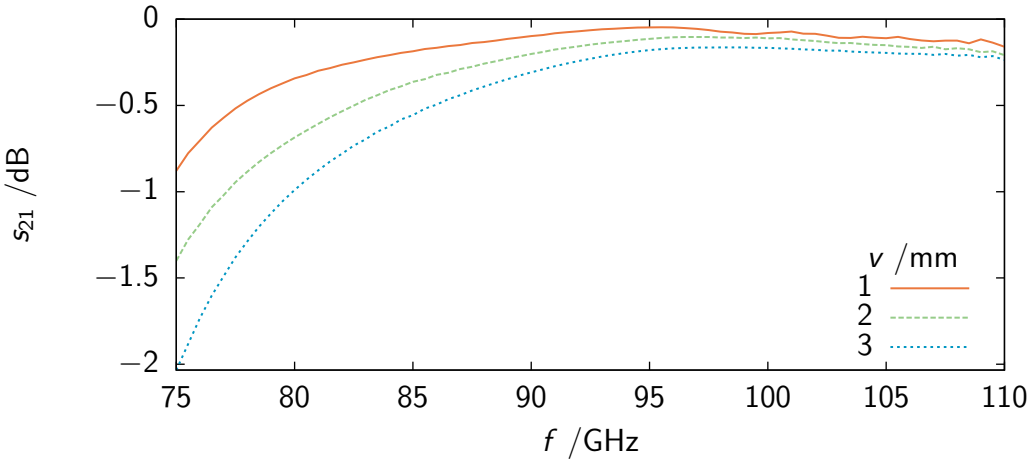

(a) $h = 3$ mm

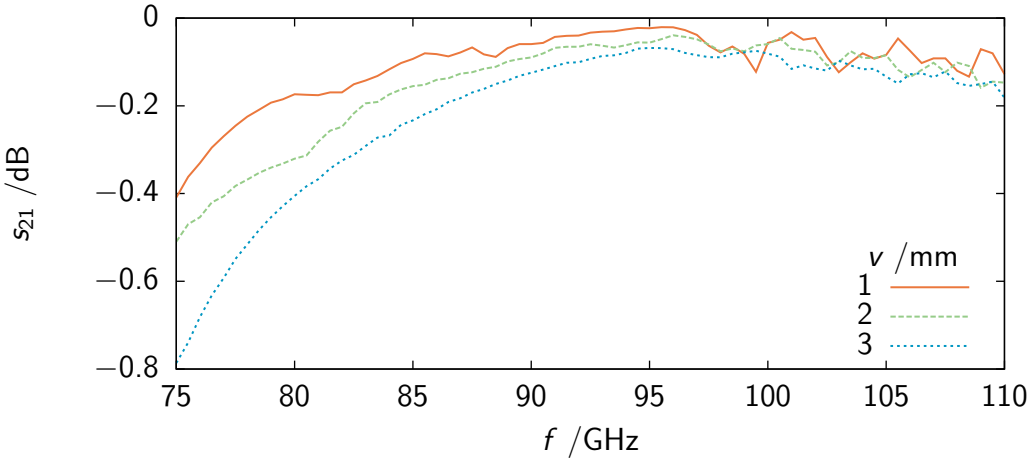

(b) $h = 5$ mm

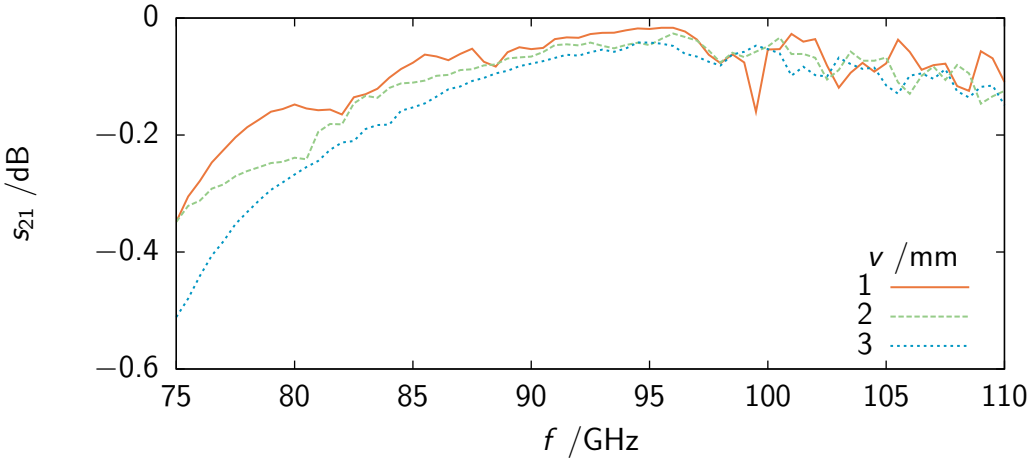

(c) $h = 7$ mm

Figure A.8: *Transmission coefficient s_{21}^{dB} of transition type (I) for varied transition length v*

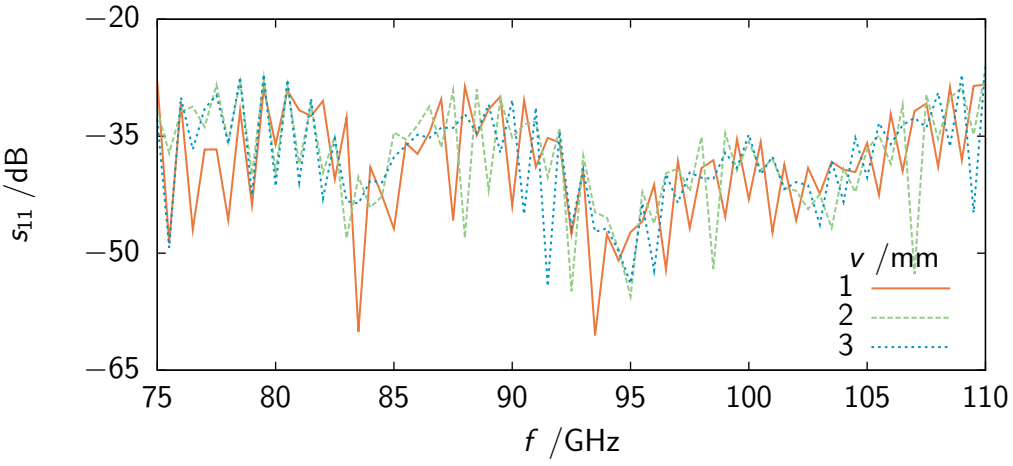

(a) $h = 3$ mm

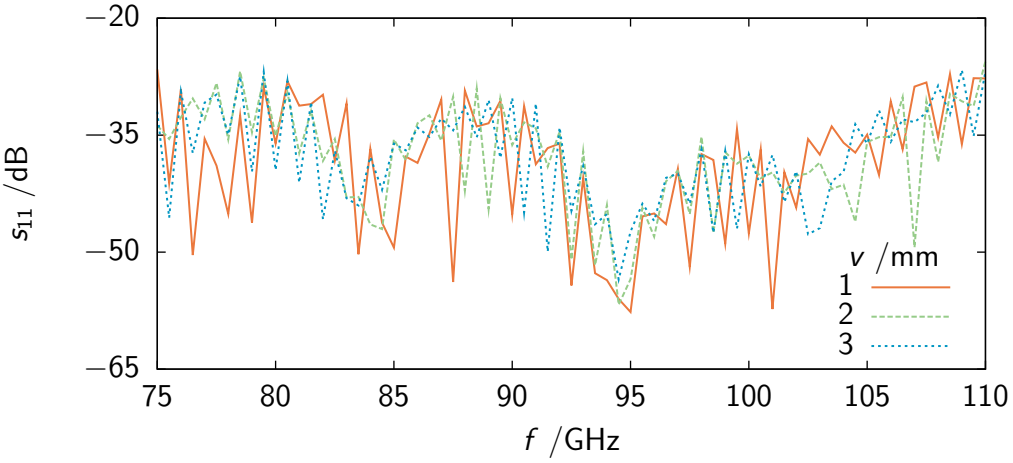

(b) $h = 5$ mm

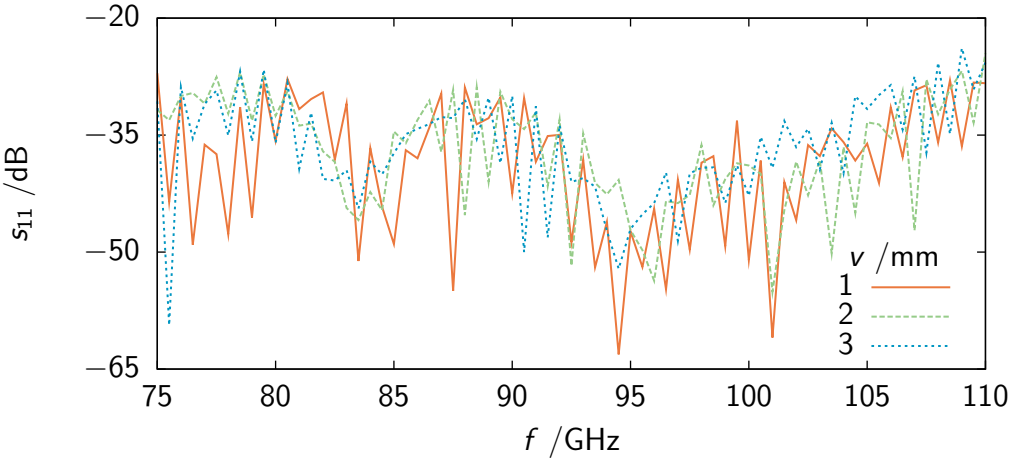

(c) $h = 7$ mm

Figure A.9: *Reflection coefficient s_{11}^{dB} of transition type (II) for varied transition length v*

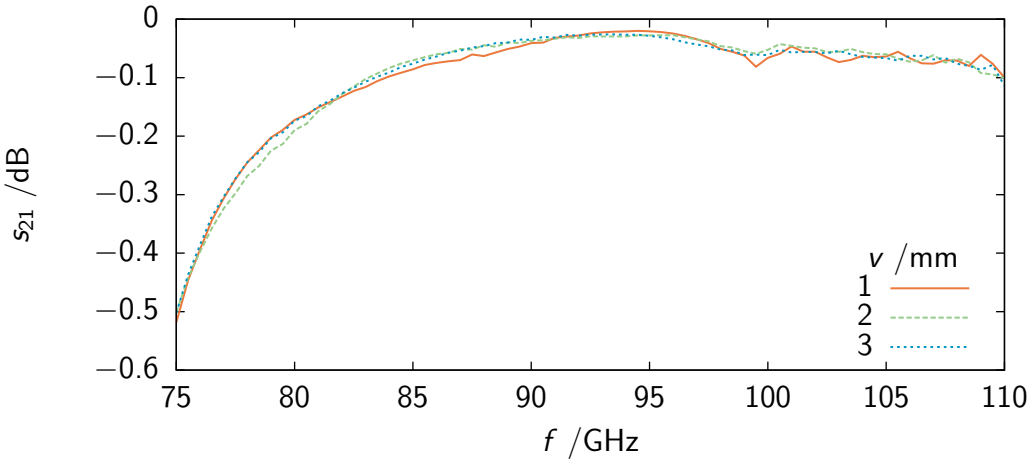

(a) $h = 3$ mm

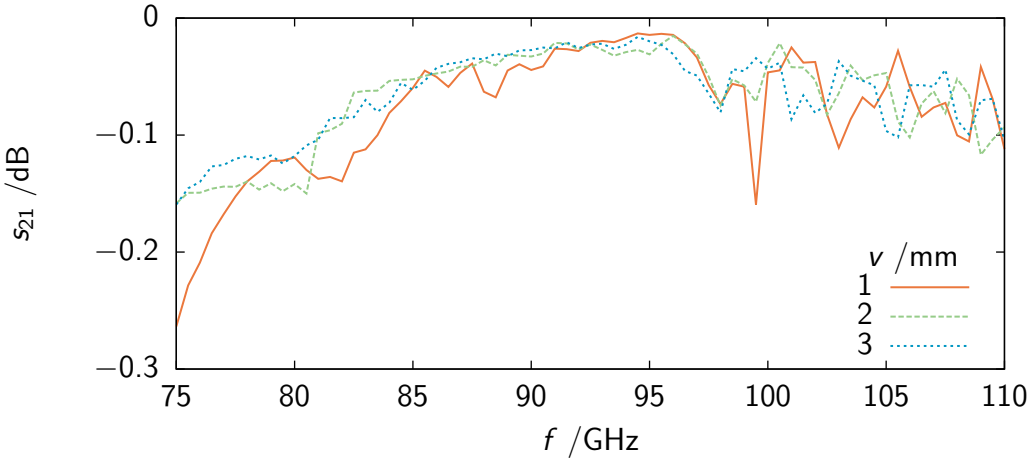

(b) $h = 5$ mm

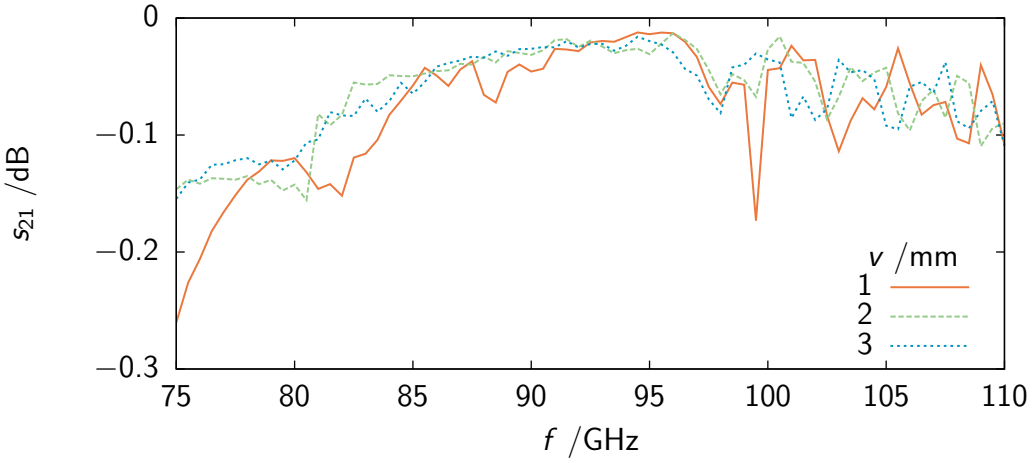

(c) $h = 7$ mm

Figure A.10: *Transmission coefficient s_{21}^{dB} of transition type (II) for varied transition length v*

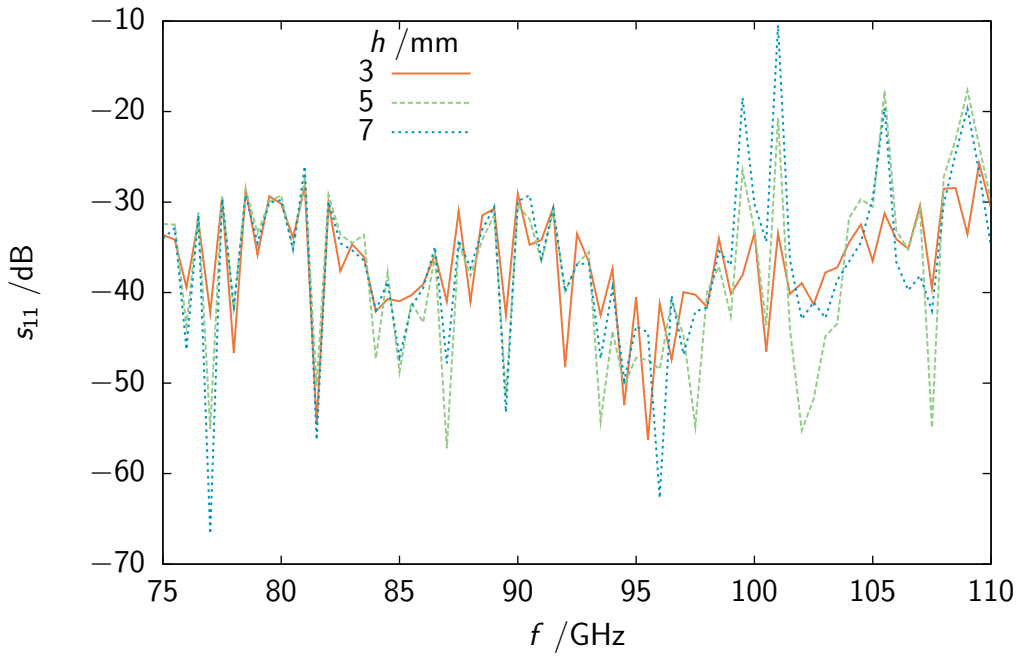

Figure A.11: *Reflection coefficient s_{11}^{dB} of transition type (IV)*

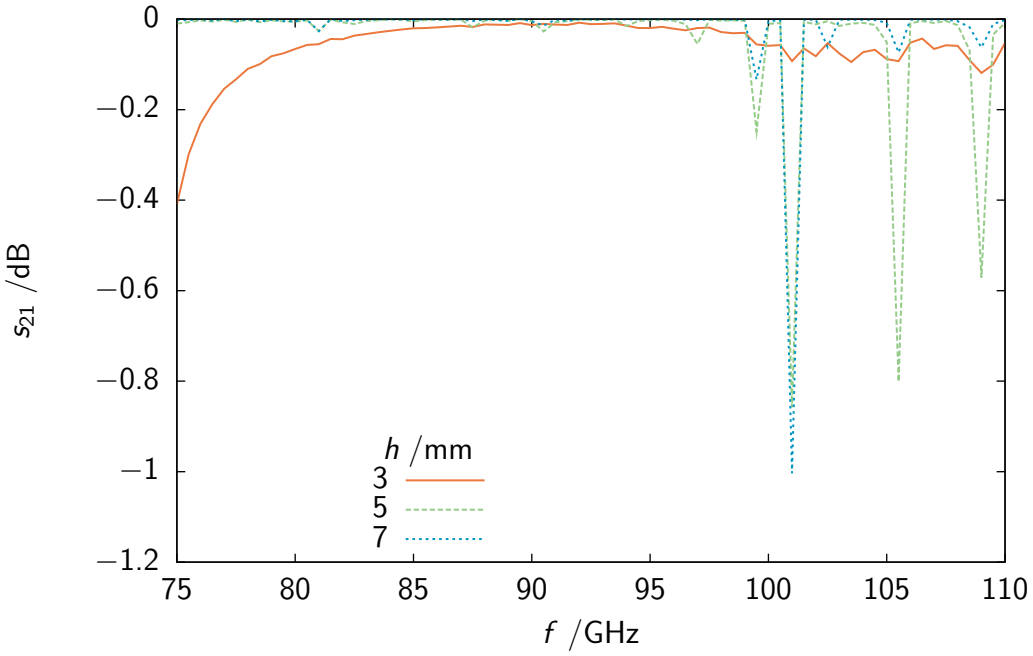

Figure A.12: *Transmission coefficient s_{21}^{dB} of transition type (IV)*

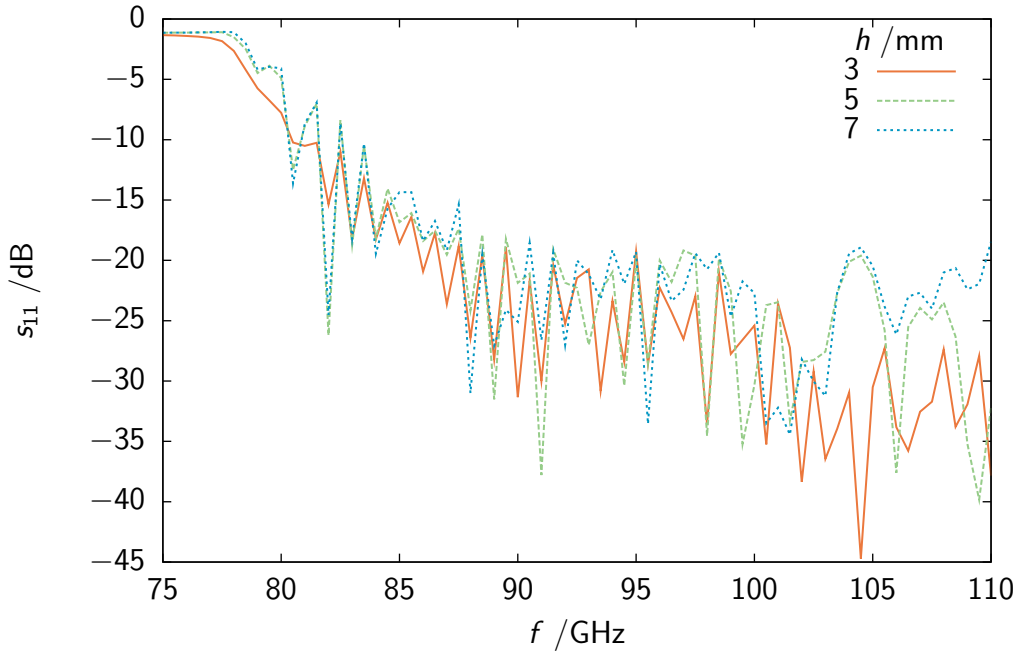

Figure A.13: *Reflection coefficient* s_{11}^{dB} *of transition type (III) for in* mm $a = d = 1.4$ *and* $b = 0.5$

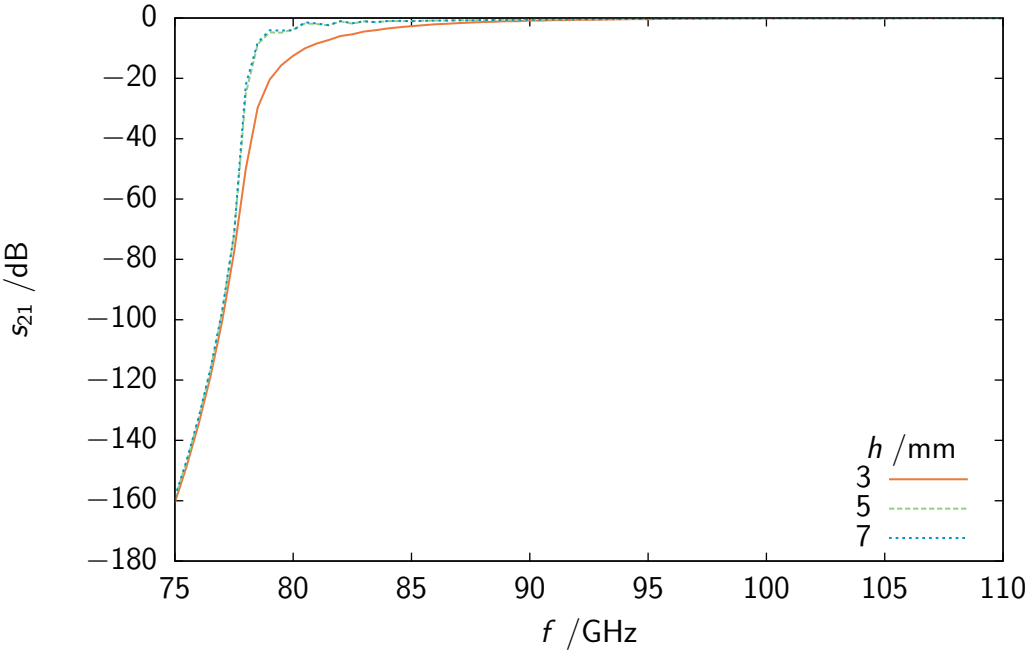

Figure A.14: *Transmission coefficient* s_{21}^{dB} *of transition type (III) for in* mm $a = d = 1.4$ *and* $b = 0.5$

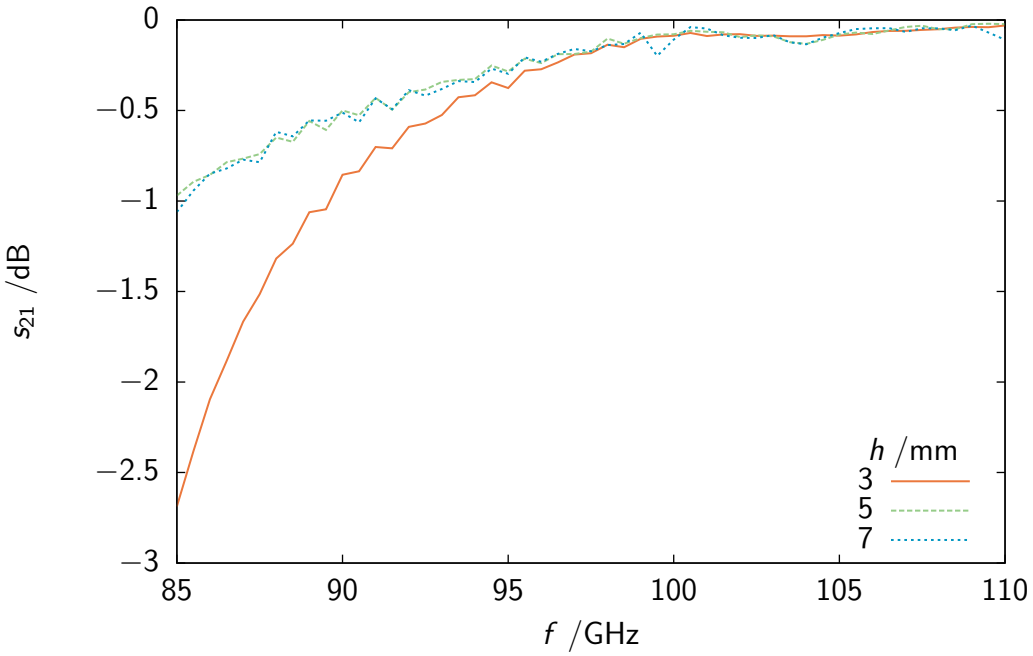

Figure A.15: *Transmission coefficient* s_{21}^{dB} *of transition type (III) for in* mm $a = d = 1.4$ *and* $b = 0.5$ *in the frequency range* 85 *to* 110 GHz

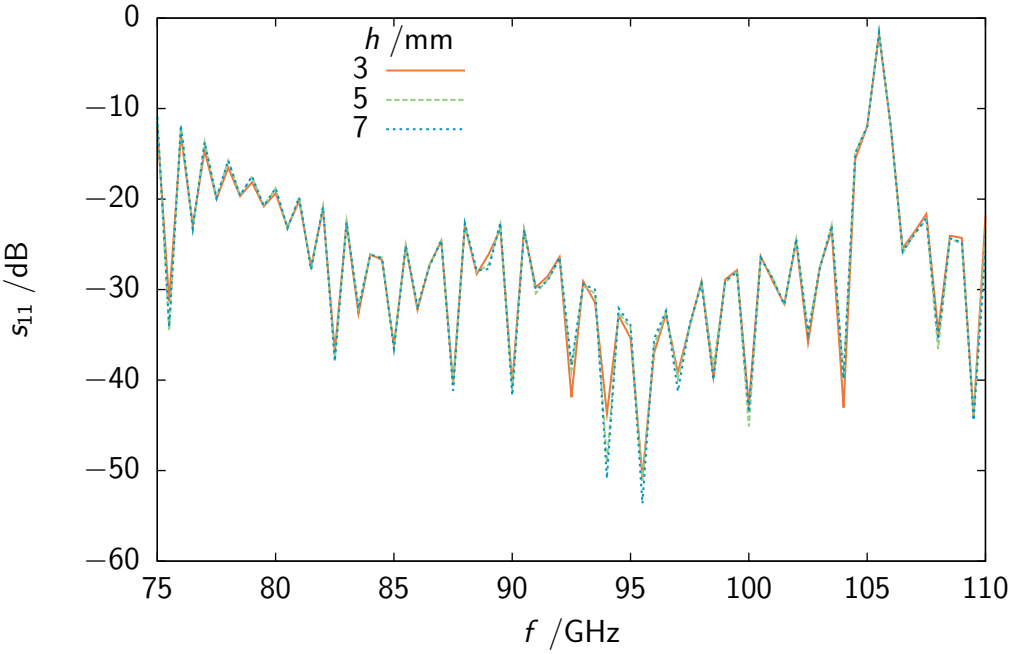

(a) $b = 0.6$ mm

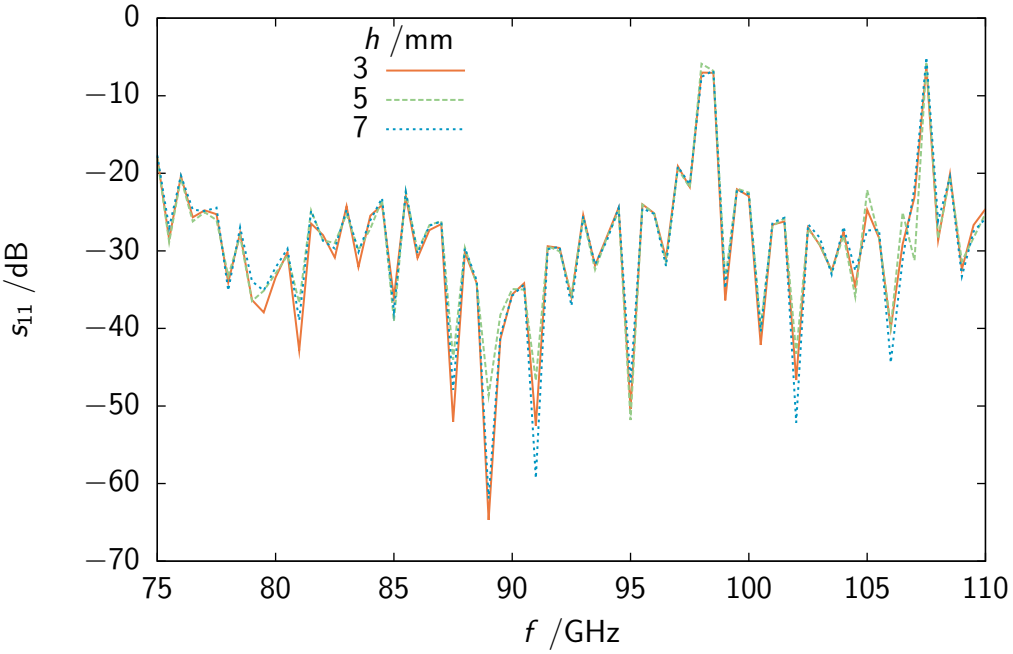

(b) $b = 0.7$ mm

Figure A.16: *Reflection coefficient* s_{21}^{dB} *of transition type (III) for* $a = d = 1.4$ mm

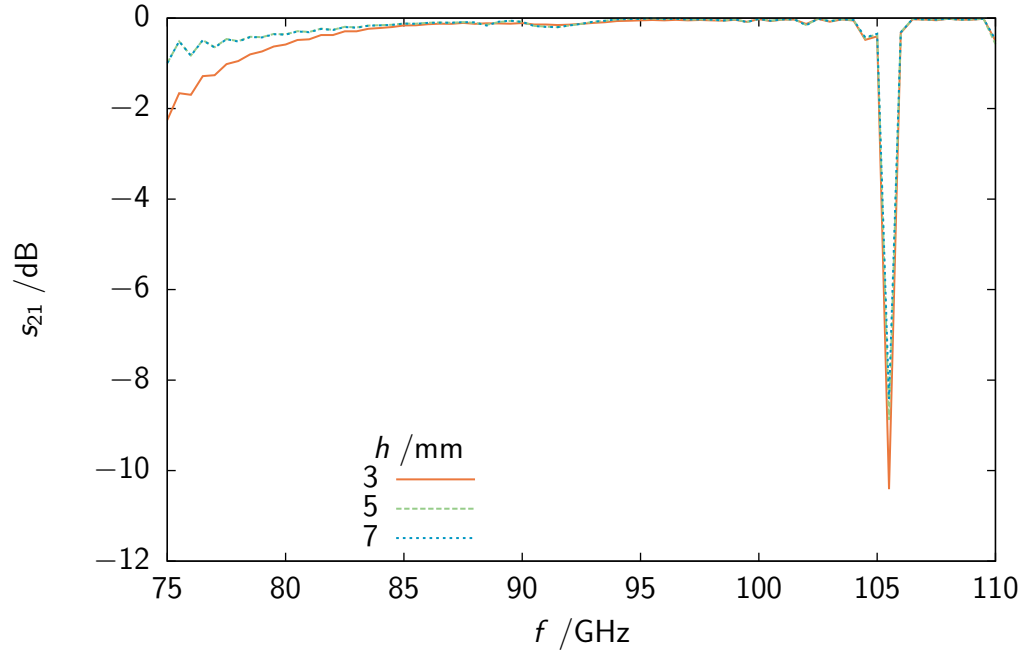

(a) $b = 0.6$ mm

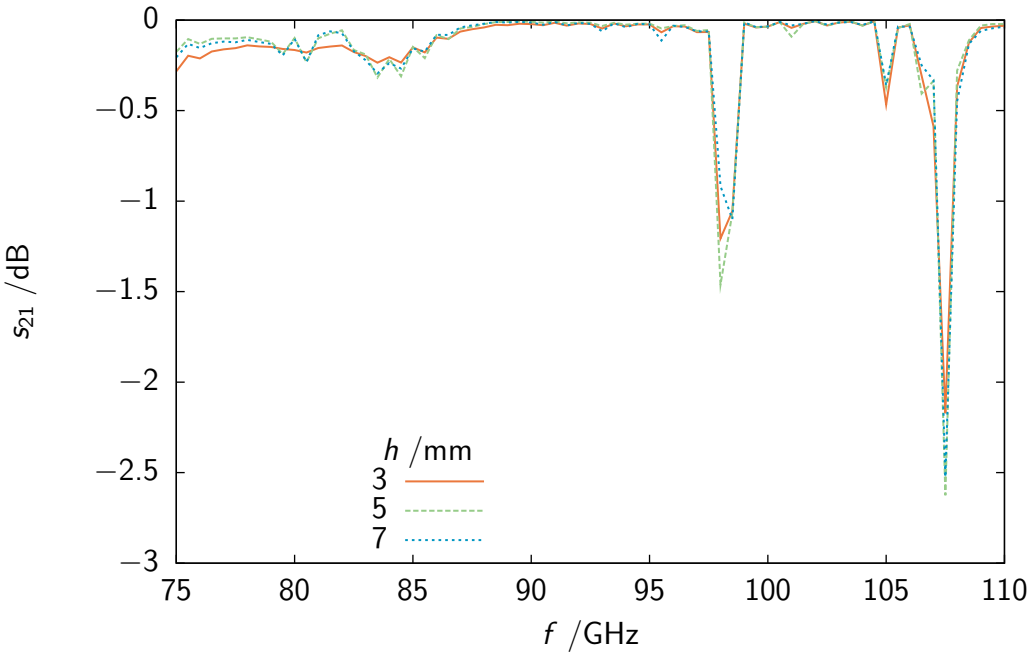

(b) $b = 0.7$ mm

Figure A.17: *Transmission coefficient* s_{21}^{dB} *of transition type (III) for* $a = d = 1.4$ mm

A.2 NON-RADIATING DIELECTRIC WAVEGUIDE ANTENNAS

A.2.1 NRD guide end-fire antenna

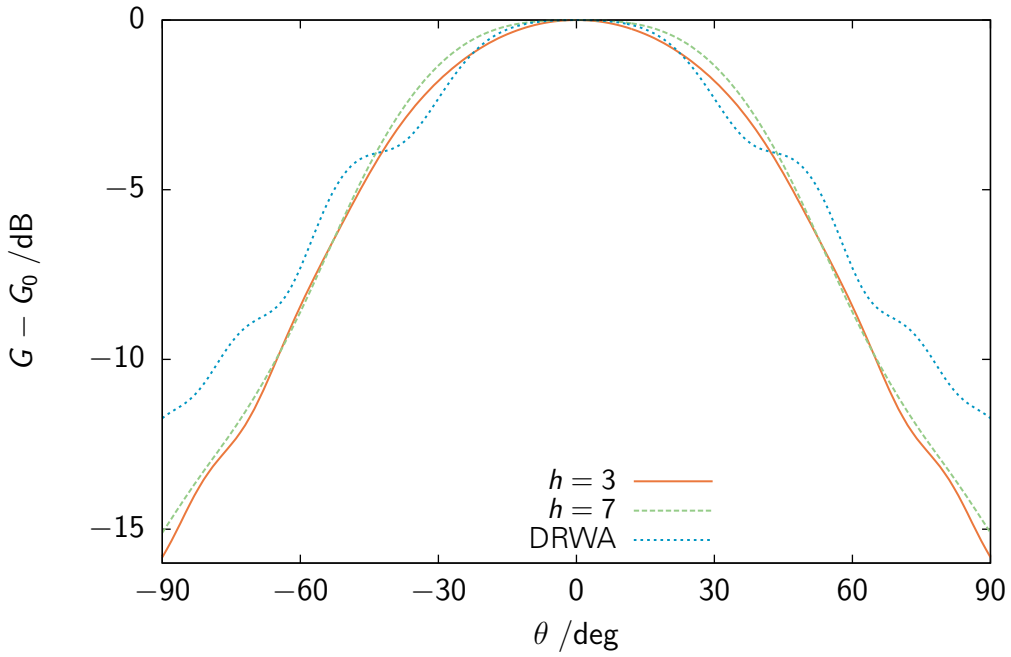

(a) **E** − *plane* , $f_2 = 85$ GHz

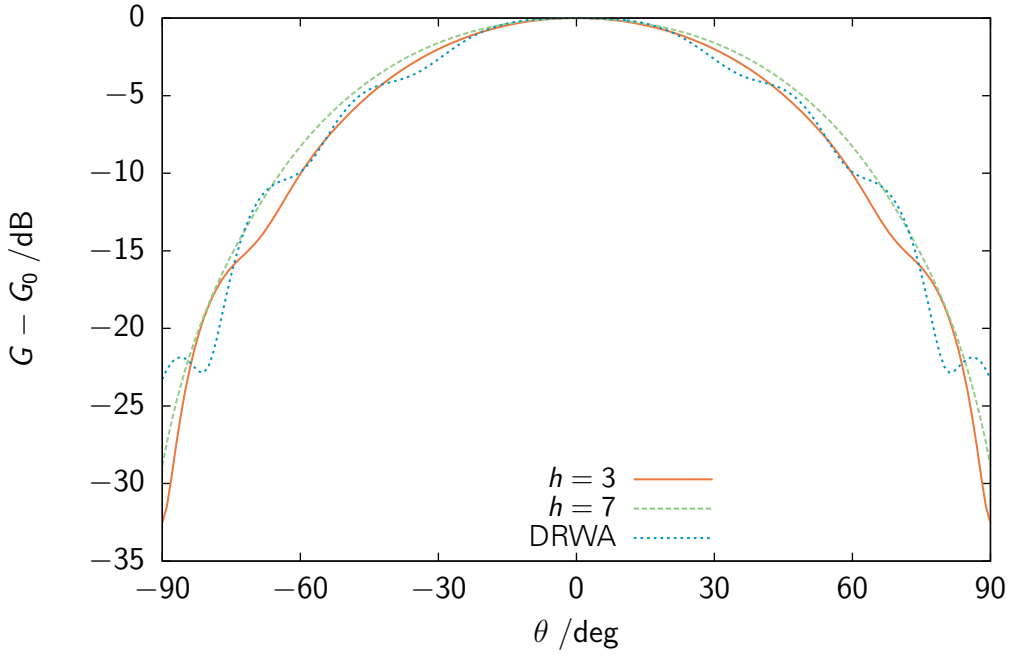

(b) **H** − *plane* , $f_2 = 85$ GHz

Figure A.18: *Comparison of the radiation patterns of the NRD guide and the DRW end-fire antenna for different values of the plate height h in* mm *at* $f_2 = 85$ GHz

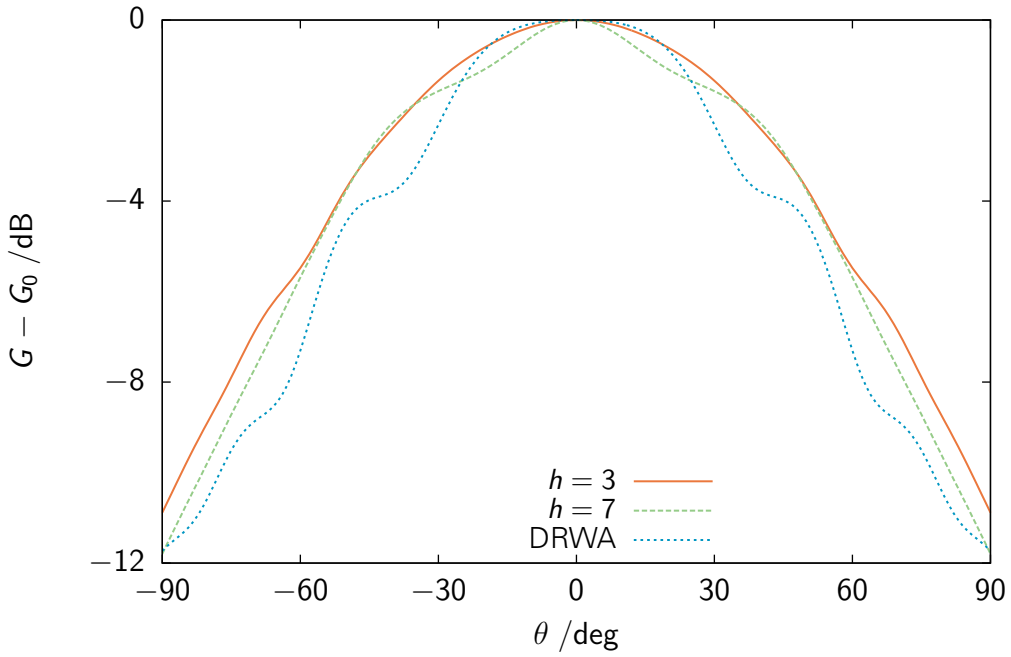

(a) **E** − *plane* , $f_3 = 95$ GHz

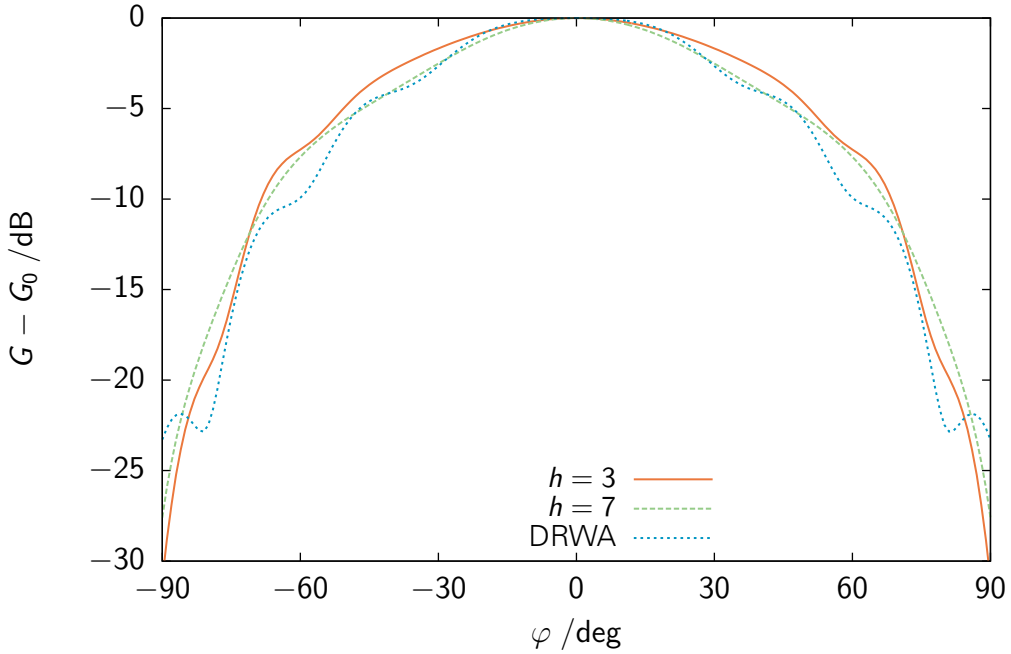

(b) **H** − *plane* , $f_3 = 95$ GHz

Figure A.19: *Comparison of the radiation patterns of the NRD guide and the DRW end-fire antenna for different values of the plate height h in* [mm] *at* $f_3 = 95$ GHz

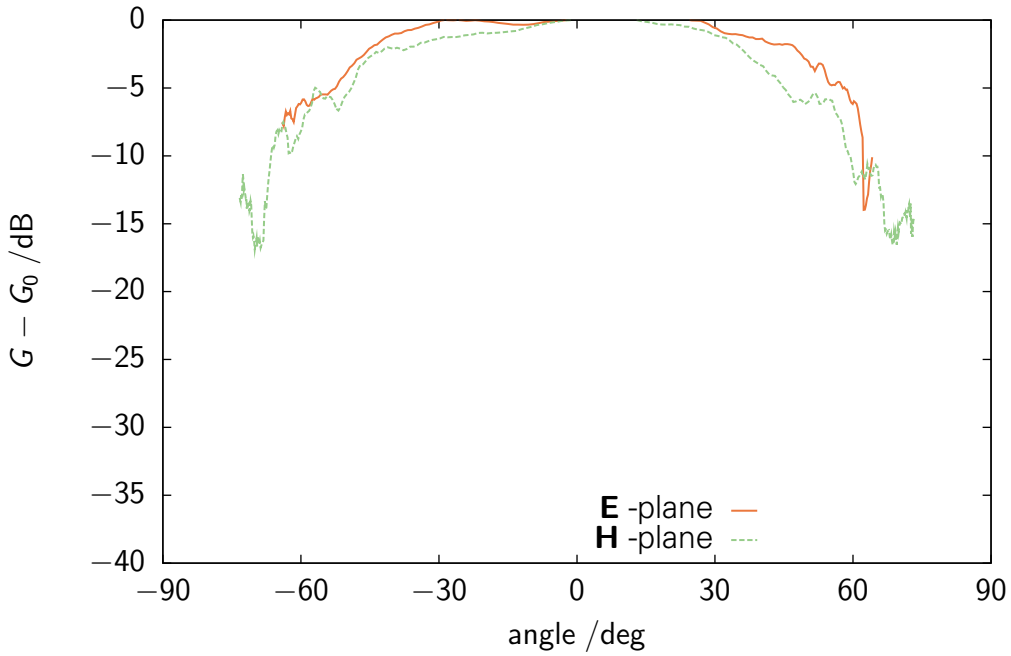

Figure A.20: *Measured* **E** *- and* **H** *-plane radiation pattern for* $f_4 = 105$ GHz

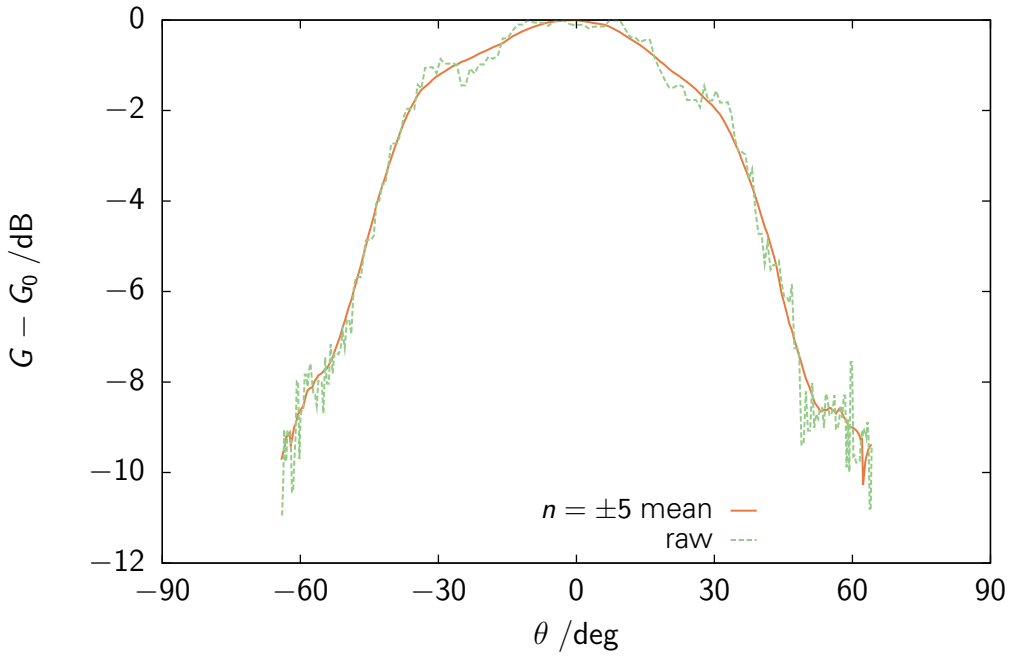

(a) $f_1 = 75$ GHz

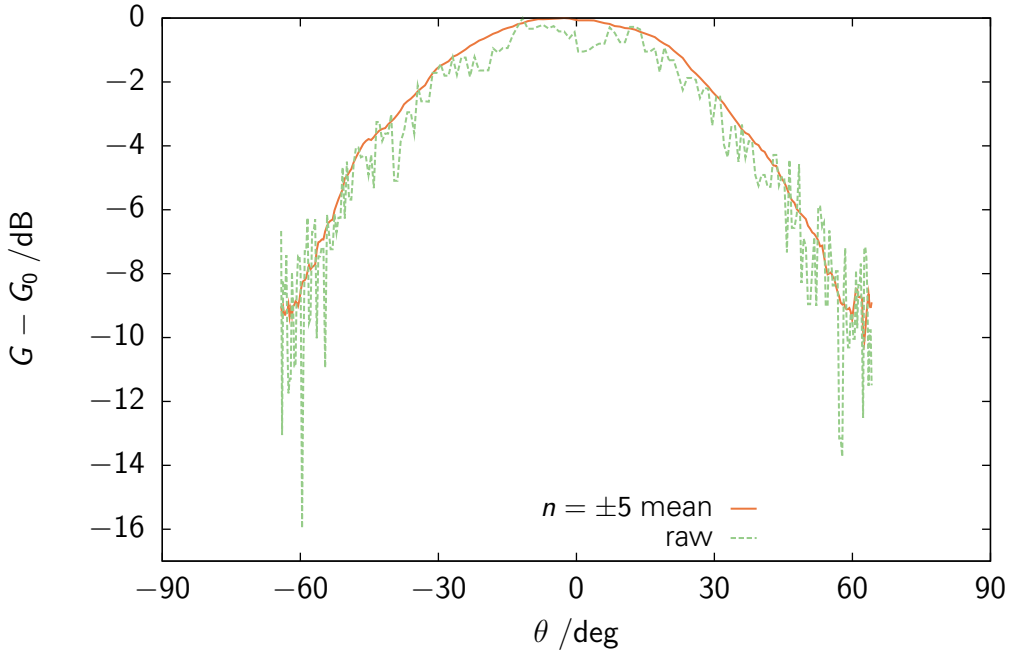

(b) $f_3 = 95$ GHz

Figure A.21: *Probe compensation* **E** *-plane radiation pattern showing the smoothing effect*

A.2.2 NRD guide leaky-wave antennas

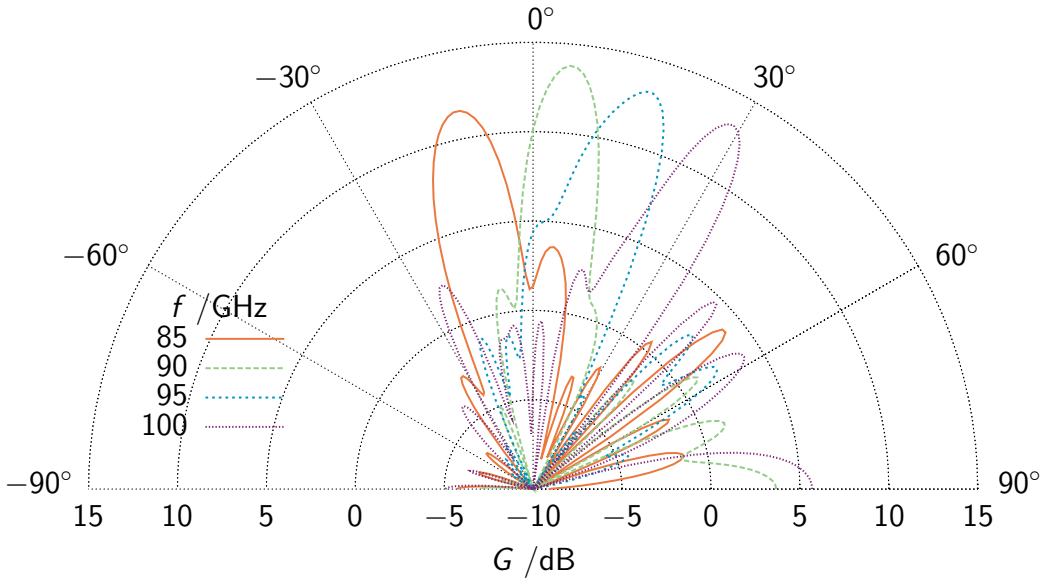

Figure A.22: **E** *-plane radiation pattern of the NRD guide leaky-wave antenna concept shown in Figure 3.22*

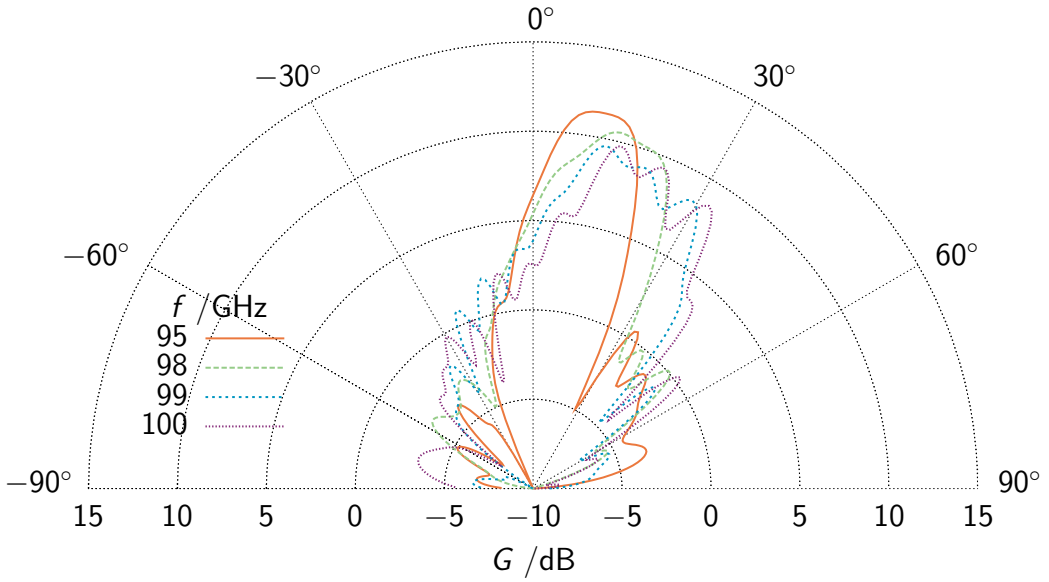

Figure A.23: **E** *-plane radiation pattern of the NRD guide leaky-wave antenna concept shown in Figure 3.22, with in* mm $o = 0$ *and* $s = 0.5$

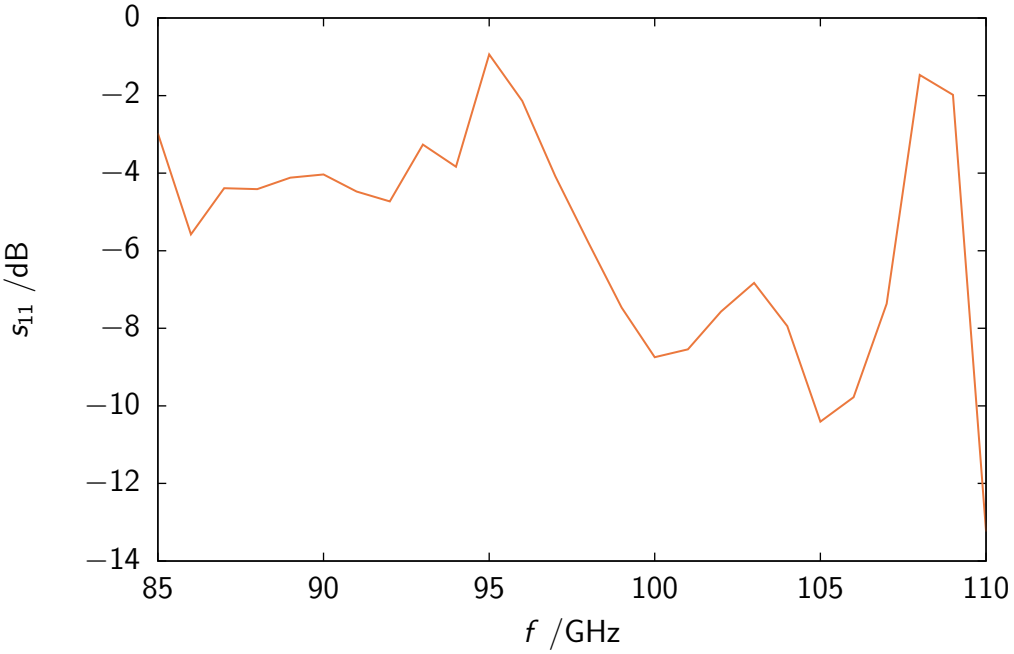

Figure A.24: *Reflection coefficient* s_{11}^{dB} *of an NRD guide leaky-wave antenna with discontinuities of type (b) shown in Figure 3.21b on page 78 with dimensions in* mm $a = 1.4$, $b = 0.5$, $p = 2$, $dl = 0.5$ *and* $dw = 0.1$

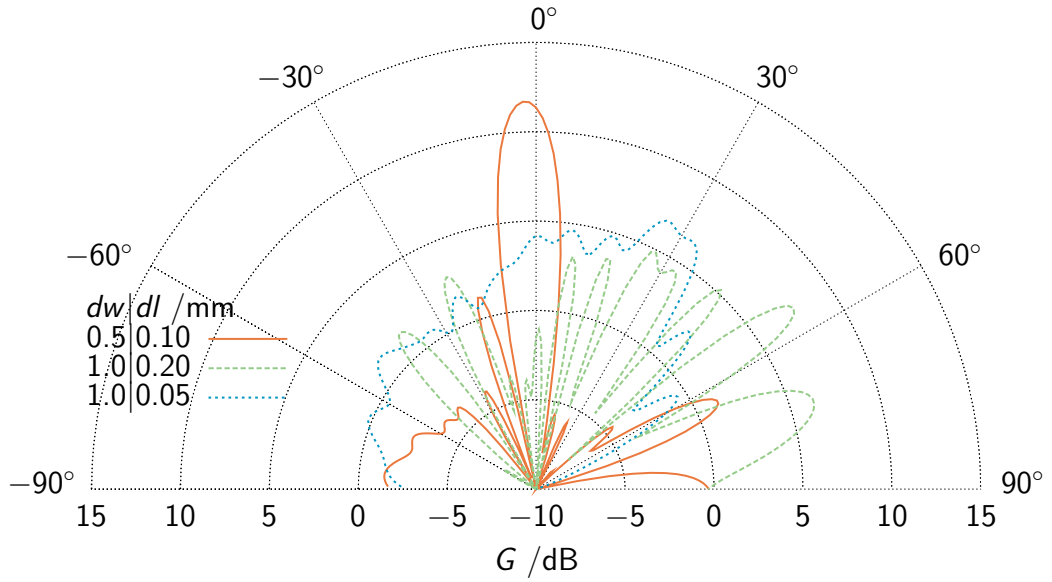

Figure A.25: E *-plane radiation pattern for different dimensions of the distontinuities with* $f = 95$ GHz *and* $p = 2$ mm

B LISTINGS

Listing B.1: NRD.m

```
function [y] = NRD_param (a,b,d)

global eps

E1=3.41^2;
%a=0.5;b=1.0;d=1.2;
y = [];
fmin=75;fmax=110;step=.1;
kx=[];ky=[];
freq=[fmin:step:fmax];
k=[2*pi*freq/300];

for f=[fmin:step:fmax]
        k0=2*pi*f/300;eps=11.9;
        x=find_kx(k0);
        kx=[kx,x];
        %eps=(k0^2*E1-x^2)/k0^2; %effective epsilon
        ky=[ky,find_ky(k0)];
end
y = (sqrt(k.^2*E1-kx.^2-ky.^2)./k)';
plot(freq,sqrt(k.^2*E1-kx.^2-ky.^2)./k,'b')


function [kx]=find_kx(k0)

        kx=fzero(@(x) Fx(x,k0),3);
end
```

```
29
        function [result]=Fx(kx,k0)
31              %global a d k0 eps;
                gammax=sqrt(k0^2*(eps-1)-kx^2);
33              C=tanh(gammax/2*(d-a));

35              result=kx*a-pi+2*atan(kx/gammax*C);
        end
37


39
        function [ky]=find_ky(k0)

41
                ky=fzero(@(x) Fy(x,k0),k0*2);
43      end


45
        function [result]=Fy(ky,k0)
47              %global a d k0 eps;
                gammay=sqrt(k0^2*(eps-1)-ky^2);
49
                result=ky*b-pi+2*atan(ky/gammay/eps);
51      end

53  end
```

C LONGITUDINAL AND TRANSVERSE FIELD COMPONENTS

$$\nabla \times \mathbf{H} = j\omega\varepsilon\mathbf{E} \,, \qquad \text{(C.1a)} \qquad -\nabla \times \mathbf{E} = j\omega\mu\mathbf{H} \,. \qquad \text{(C.1b)}$$

As described in [21] the electric and magnetic field can be expressed in longitudinal and transverse field components. Using the definition

$$\nabla = \nabla_t + \mathbf{e}_z \frac{\partial}{\partial z} \tag{C.2}$$

the electric and magnetic field can be described as

$$\mathbf{E} = \mathbf{e}_z E_z + \mathbf{E}_t \,, \qquad \mathbf{H} = \mathbf{e}_z H_z + \mathbf{H}_t \,. \tag{C.3}$$

Inserting equation (C.2) and equation (C.3) into equations (C.1) leads to

$$\begin{aligned} \left(\nabla_t + \mathbf{e}_z \frac{\partial}{\partial z}\right) \times (\mathbf{H}_t + \mathbf{e}_z H_z) &= j\omega\varepsilon \left(\mathbf{e}_z E_z + \mathbf{E}_t\right) \,, \\ \nabla_t \times \mathbf{H}_t + \mathbf{e}_z \frac{\partial}{\partial z} \times \mathbf{H}_t + \nabla_t \times \mathbf{e}_z H_z &= j\omega\varepsilon \left(\mathbf{e}_z E_z + \mathbf{E}_t\right) \end{aligned} \tag{C.4}$$

and

$$\begin{aligned} \left(\nabla_t + \mathbf{e}_z \frac{\partial}{\partial z}\right) \times (\mathbf{E}_t + \mathbf{e}_z E_z) &= -j\omega\mu \left(\mathbf{e}_z H_z + \mathbf{H}_t\right) \,, \\ \nabla_t \times \mathbf{E}_t + \mathbf{e}_z \frac{\partial}{\partial z} \times \mathbf{E}_t + \nabla_t \times \mathbf{e}_z E_z &= -j\omega\mu \left(\mathbf{e}_z H_z + \mathbf{H}_t\right) \,. \end{aligned} \tag{C.5}$$

These equations can be divided into a longitudinal (z) and a transverse (t) compo-

nent:

$$\text{z:} \qquad \nabla_t \times \mathbf{E}_t = -j\omega\mu \mathbf{e}_z H_z \ , \tag{C.6}$$

$$\nabla_t \times \mathbf{H}_t = j\omega\varepsilon \mathbf{e}_z E_z \ , \tag{C.7}$$

$$\text{t:} \qquad \mathbf{e}_z \frac{\partial}{\partial z} \times \mathbf{E}_t + \nabla_t \times \mathbf{e}_z E_z = -j\omega\mu \mathbf{H}_t \ , \tag{C.8}$$

$$\mathbf{e}_z \frac{\partial}{\partial z} \times \mathbf{H}_t + \nabla_t \times \mathbf{e}_z H_z = j\omega\varepsilon \mathbf{E}_t \ . \tag{C.9}$$

To eliminate E_t (C.9) is written in the form

$$\mathbf{E}_t = \frac{1}{j\omega\varepsilon} \left(\mathbf{e}_z \frac{\partial}{\partial z} \times \mathbf{H}_t + \nabla_t \times \mathbf{e}_z H_z \right) \tag{C.10}$$

and insert it in equation (C.8) with $\frac{\partial}{\partial z} = -jk_z$ (according to **??**) and $k^2 = \omega^2\mu\varepsilon$ being the wave number in the filling material:

$$\begin{aligned} -j\omega\mu\mathbf{H}_t &= \mathbf{e}_z \frac{\partial}{\partial z} \times \left(\frac{1}{j\omega\varepsilon} \left(\mathbf{e}_z \frac{\partial}{\partial z} \times \mathbf{H}_t + \nabla_t \times \mathbf{e}_z H_z \right) \right) + \nabla_t \times \mathbf{e}_z E_z \ , \\ &= -\frac{k_z}{\omega\varepsilon} \left(\nabla_t H_z + jk_z \mathbf{H}_t \right) + \nabla \times \mathbf{e}_z E_z \ , \\ \mathbf{H}_t &= -j\frac{k_z}{k^2} \nabla_t H_z + \frac{k_z^2}{k^2} - j\frac{\omega\varepsilon}{k^2} \mathbf{e}_z \times \nabla_t E_z \ , \end{aligned} \tag{C.11}$$

using the identities

$$\mathbf{e}_z \times (\nabla_t \times \mathbf{e}_z H_z) = \nabla_t H_z \ , \tag{C.12}$$

$$\mathbf{e}_z \times (\mathbf{e}_z \times \mathbf{H}_t) = -\mathbf{H}_t \ , \tag{C.13}$$

$$\nabla_t \times \mathbf{e}_z E_z = -\mathbf{e}_z \times \nabla_t E_z \ . \tag{C.14}$$

Now it is possible to write $\mathbf{H}_t$ depending on the longitudinal components E_z and H_z only:

$$\mathbf{H}_t = \frac{1}{k_z^2 - k^2} \left(jk_z \nabla_t H_z + j\omega\varepsilon \mathbf{e}_z \times \nabla_t E_z \right) \ . \tag{C.15}$$

The equation for $\mathbf{E}_t$ can be derived analogously:

$$\mathbf{E}_t = \frac{1}{k_z^2 - k^2} \left(jk_z \nabla_t E_z - j\omega\mu \mathbf{e}_z \times \nabla_t H_z \right) \ . \tag{C.16}$$

D PROPAGATION CONSTANT

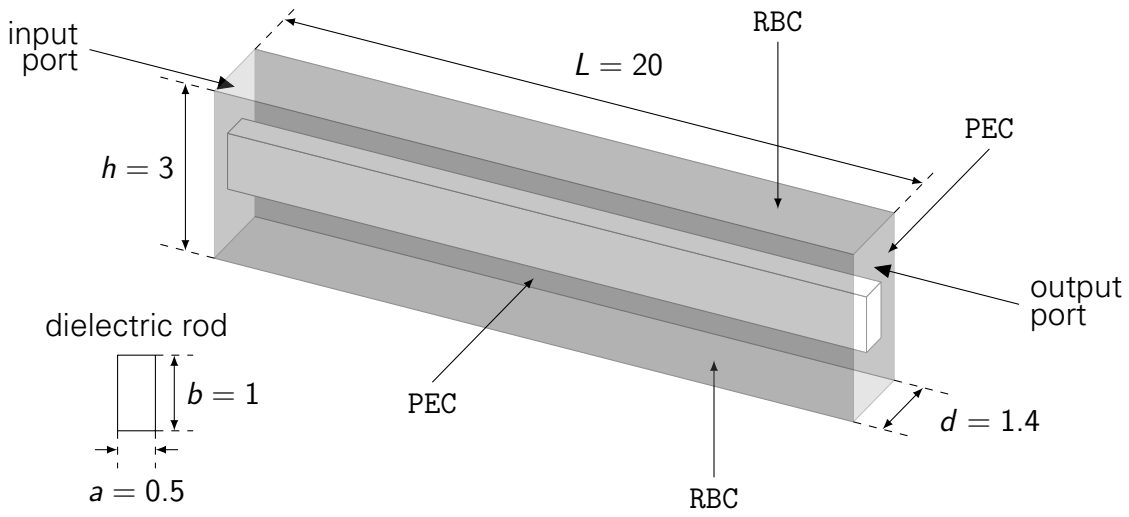

Figure D.1: HFSS *NRD model showing the simulation boundaries and the dimensions of the NRD guide and the dielectric rod in* mm

It is possible to obtain the dispersion curve of the NRD guide from simulation results in an analytical way. Therefore a structure as shown in *Figure D.1* has been simulated in *HFSS*. The parallel metal plates were presented as *perfect electric conductor* (PEC) boundaries and *radiation boundaries* (RBC) were assigned to the top and bottom layer of the model.

After simulation the phase shift $\varphi|_{s_{21}}$ of the wave at the ouput port compared to the incident wave at the input port was studied (*Figure D.2*. The propagation constant k_z can be calculated by

$$k_z = \frac{|\phi|}{L} \tag{D.1}$$

where L is the length of the guiding structure and ϕ the phase shift the field experiences along the length of the waveguide. As the phase shift at the output port

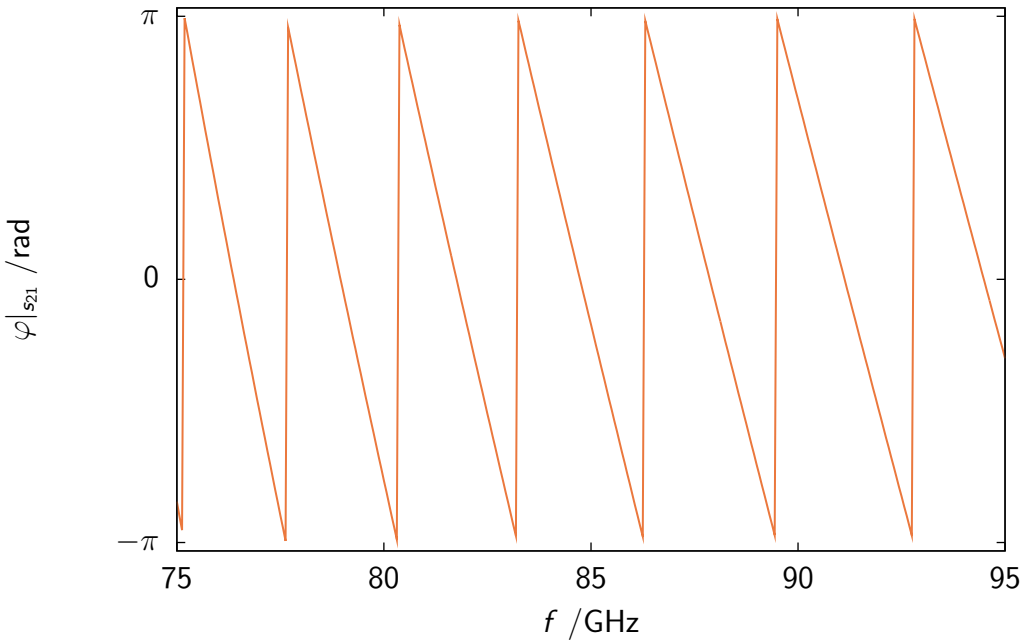

Figure D.2: *Phase shift $\varphi_{s_{21}}$ at the output port compared to the incident phase at the input port*

is only relative to the phase at the input port the distribution of the electric field along the waveguide had to be examined for the lowest frequency of the studied frequency range $f_l = 75$ GHz. The field distribution is presented in *Figure D.3*. The propagation constant k_z is the spatial equivalent to freuency representing the number of nodes of the field per unit length. The overall phase shift of the wave along the waveguide is then determined by

$$\phi = \phi_{s_{21}} - 2\pi \cdot N \tag{D.2}$$

where N is the number of rotations the incident wave experiences along the guiding structure obtained from *Figure D.3*. With $N_{75\,\mathrm{GHz}} = 8$ the phase shift ϕ is shown in *Figure D.4* and using equation (D.1) the dispersion diagram $k_z/k_0 - f$, with $k_0 = \frac{2\pi}{\lambda_0}$ being the wavenumber in free space, shown in *Figure D.5* was plotted. With the relation of the guide wavelength λ_g to the propagation constant k_z

$$\lambda_g = \frac{2\pi}{k_z} \tag{D.3}$$

the guide wavelength was calculated (*Figure D.6*) which is crucial for the design of leaky-wave antennas based on NRD guides.

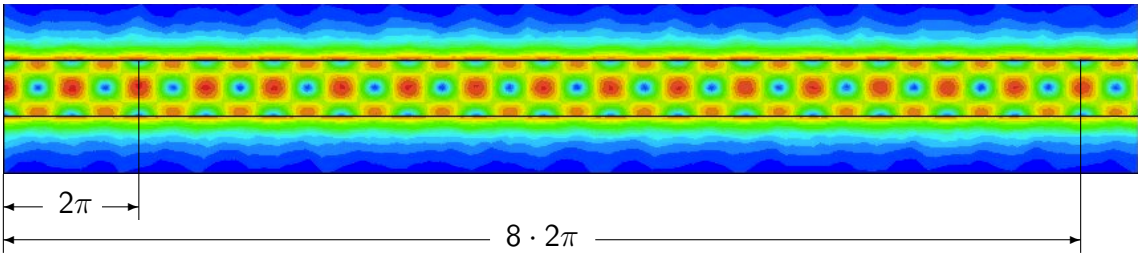

Figure D.3: *Magnitude of the electric field in the vertical plane of the NRD guide model at $f_l = 75$ GHz showing the number of full rotations the electromagnetic wave experience along the guide structure ($N = 8$)*

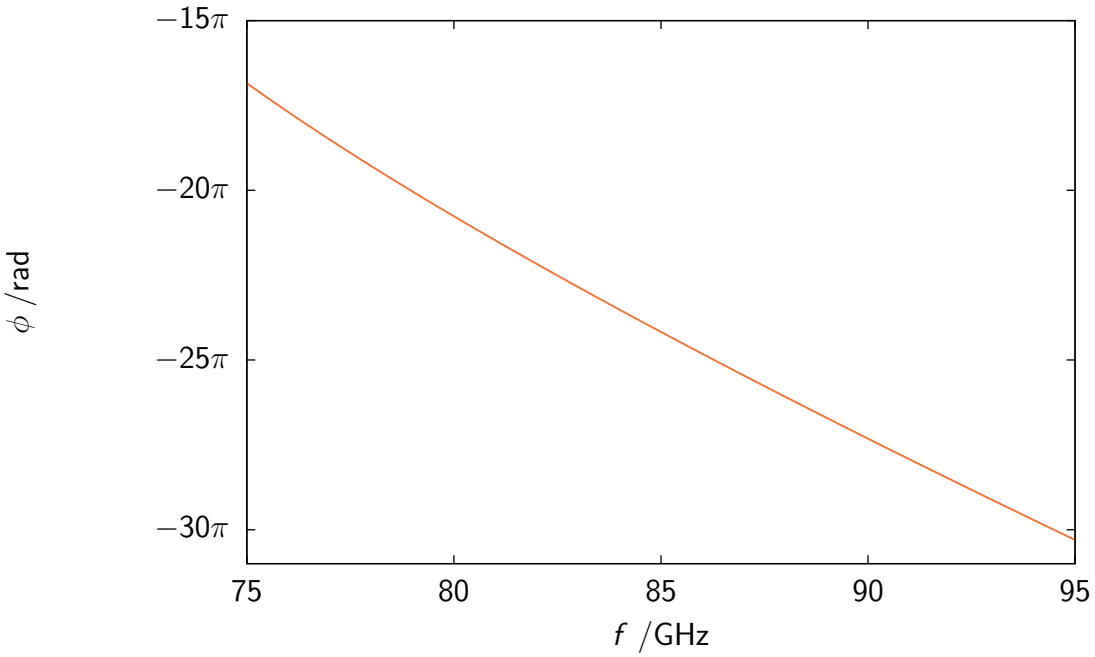

Figure D.4: *Cumulative phase shift $\phi_{s_{21}}$ along the NRD guide structure at the output port*

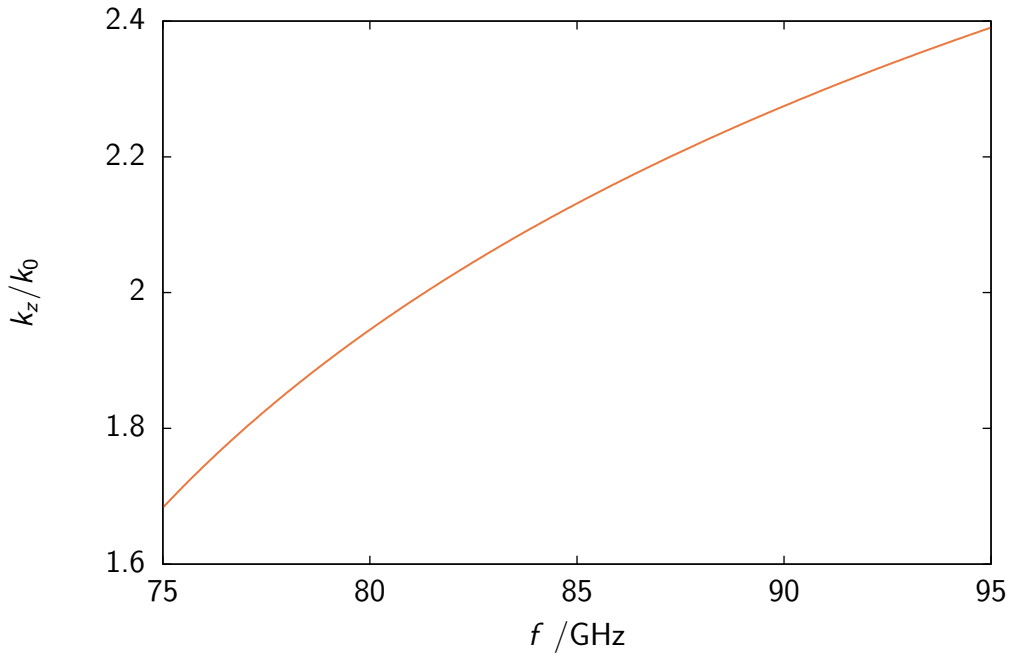

Figure D.5: *Dispersion curve $k_z/k_0 - f$ of the NRD guide model*

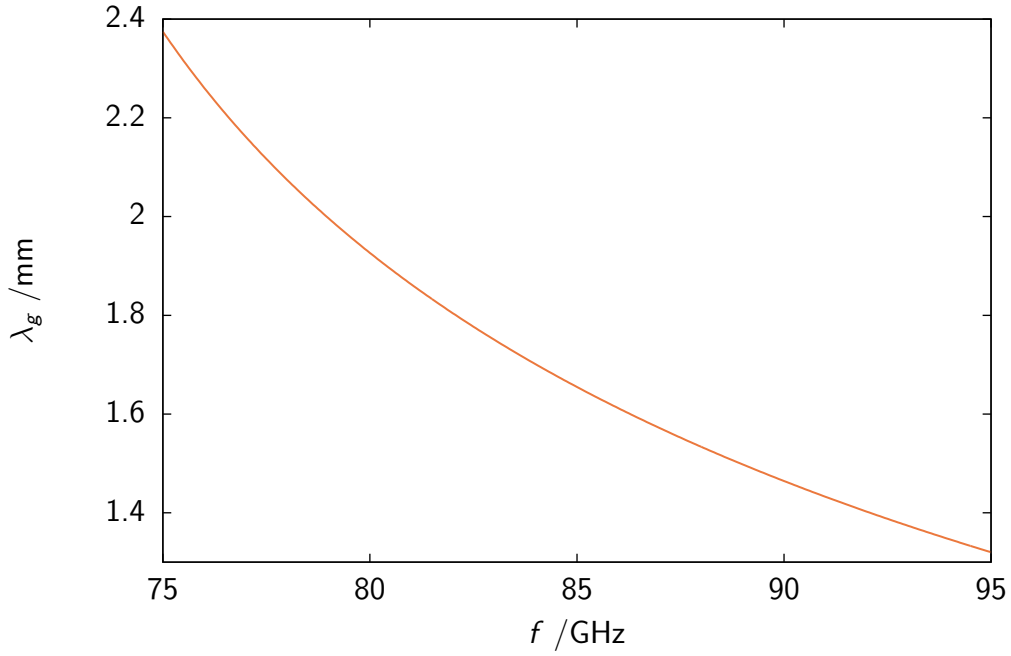

Figure D.6: *Guide wavelength $\lambda_g - f$ of the NRD guide model*

E DIELECTRIC ROD WAVEGUIDE ANTENNA

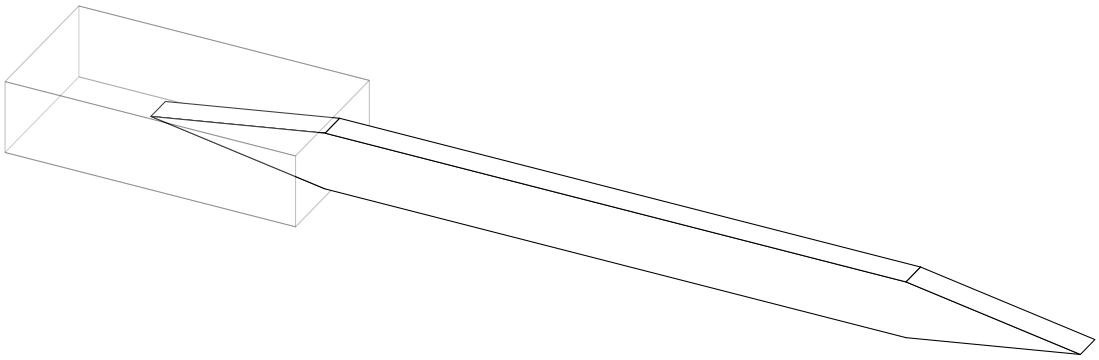

Figure E.1: *Schematic model of the dielectric rod waveguide antenna with RWG to DRW transition*

In [9] a dielectric rod waveguide antenna excited by a rectangular waveguide for the **W** frequency band from 75 to 110 GHz was introduced (its schematic is shown in *Figure E.1*). The dimensions of the dielectric rod are in mm $a = 0.5$, $b = 1$ and $m = 6$ for the length of the taper section (compare to *Figure 2.29* on page 45) and its simulation model with **E** and **H** symmetry planes is sketched in *Figure E.2*. The polar radiation patterns for $f_1 = 75$ GHz, $f_2 = 85$ GHz and $f_3 = 95$ GHz are shown in *Figure E.3* and the normalized gain $G^{\mathrm{dB}} - G_0^{\mathrm{dB}}$ in *Figures E.4* to *E.6*.

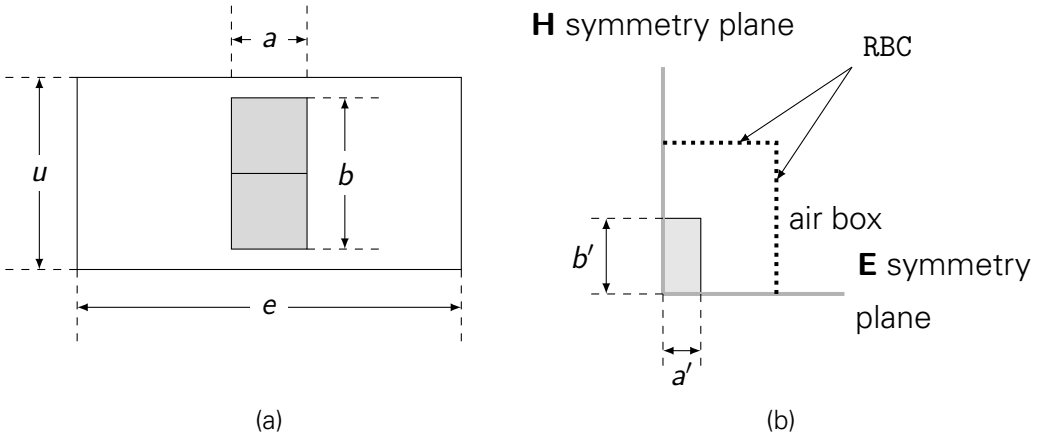

Figure E.2: *(a) Cross-section of the metal waveguide to DRW transition and (b) DRW end-fire antenna simulation cross-section with dimensions in* mm $a = 2a' = 0.5$ *and* $b = 2b' = 1$

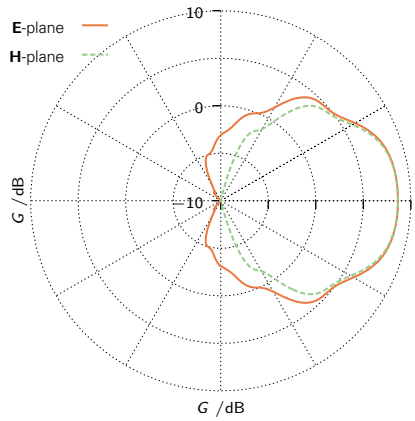

(a) $f_1 = 75$ GHz

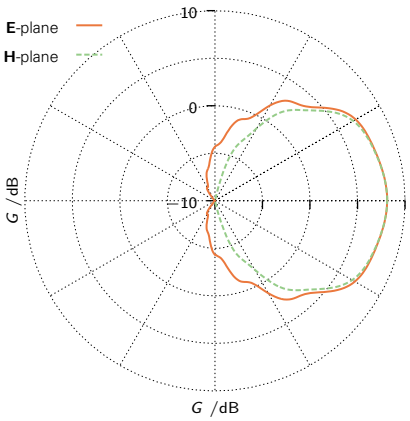

(b) $f_2 = 85$ GHz

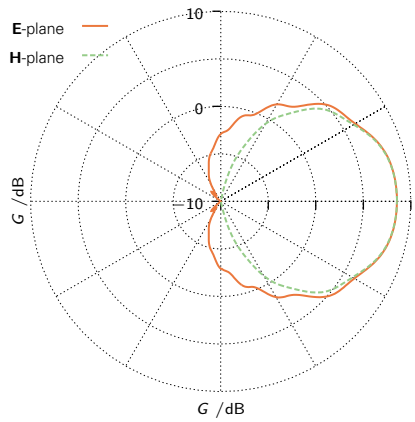

(c) $f_3 = 95$ GHz

Figure E.3: *Radiation patterns of the DRW end-fire antenna*

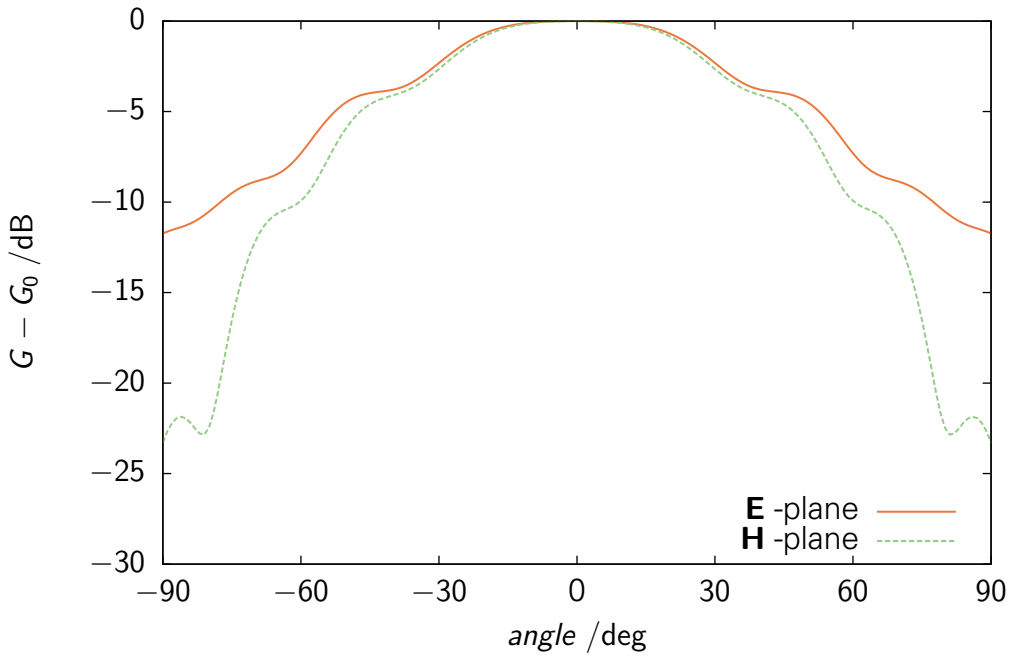

Figure E.4: *Normalized gain* $G^{\mathrm{dB}} - G_0^{\mathrm{dB}}$ *of the DRW antenna for* $f_1 = 75$ GHz

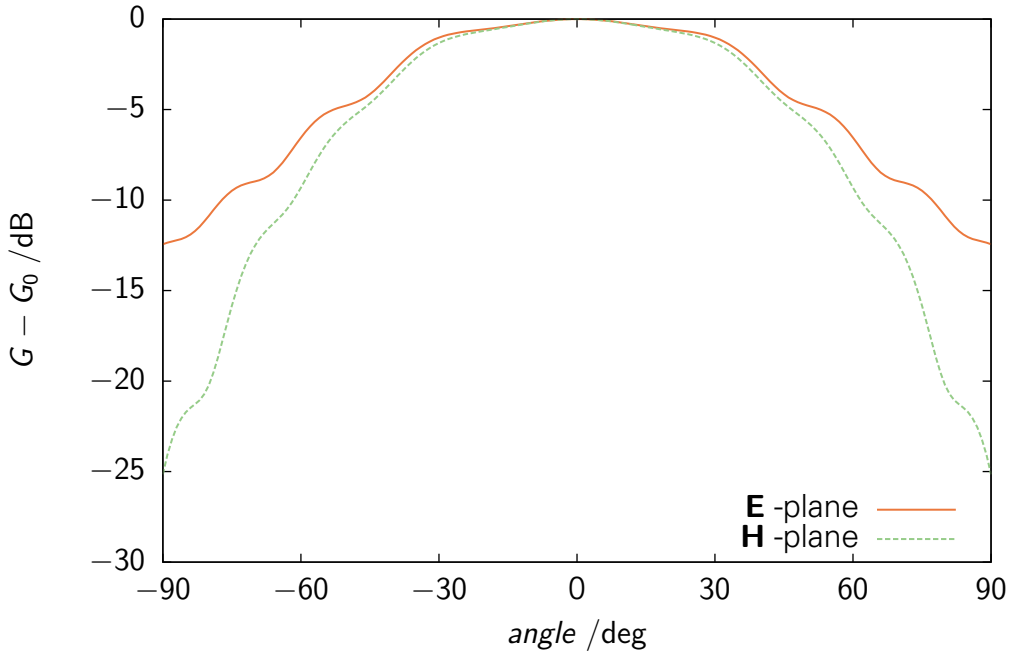

Figure E.5: *Normalized gain* $G^{\mathrm{dB}} - G_0^{\mathrm{dB}}$ *of the DRW antenna for* $f_2 = 85$ GHz

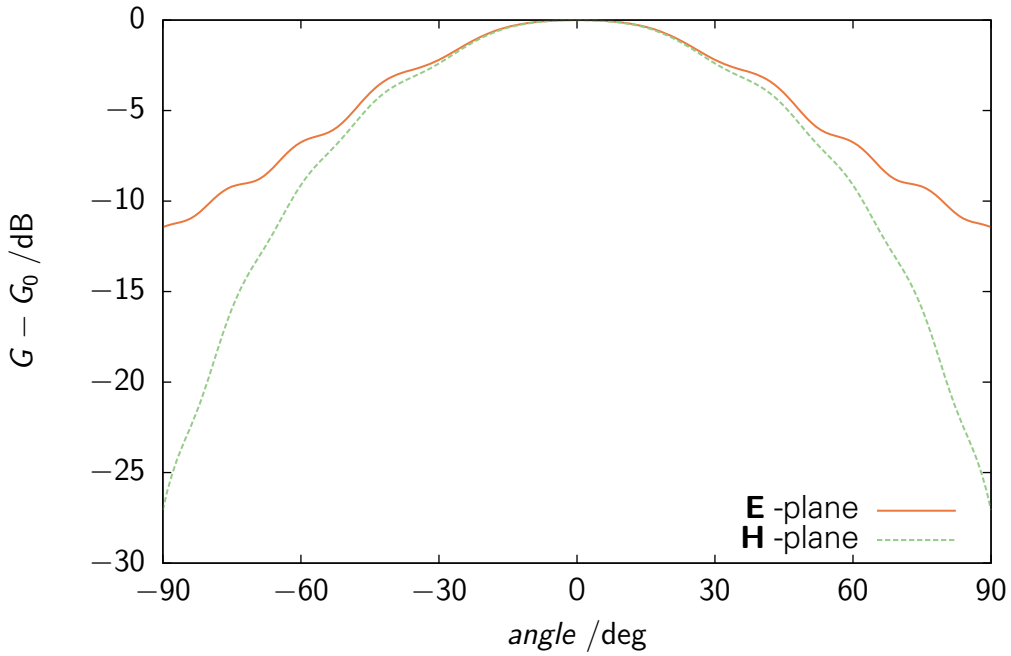

Figure E.6: *Normalized gain* $G^{\mathrm{dB}} - G_0^{\mathrm{dB}}$ *of the DRW antenna for* $f_3 = 95$ GHz

Bibliography

[1] R. Fitzpatrick, *Maxwell's Equations and the Principles of Electromagnetism*. INFINITY SCIENCE PRESS LLC, 2008.
http://www.jblearning.com/catalog/9781934015209/

[2] C. H. Papas, *Theory of Electromagnetic Wave Propagation*. McGraw-Hill, 1965.

[3] S. Mastalerz, "Electromagnetic Metamaterials in Transmission Line and Antenna Applications," 2009, Study thesis, Dresden University of Technology.

[4] R. F. Harrington, *Time-Harmonic Electromagnetic Fields*, 2nd ed. John Wiley & Sons, 2001.
http://eu.wiley.com/WileyCDA/WileyTITLE/productCd-047120806X.html

[5] R. P. Feynman, R. B. Leighton, and M. Sands, *The Feynman Lectures on Physics*. Addison-Wesley Longman, 1998, vol. 2.

[6] R. E. Collin, *Foundations for Microwave Engineering*. John Wiley & Sons, 2001.
http://eu.wiley.com/WileyCDA/WileyTITLE/productCd-0780360311.html

[7] MIL-DTL-85/3C, WAVEGUIDES, RIGID, RECTANGULAR (MILLIMETER WAVELENGTH), October 2005.
http://www.dscc.dla.mil/Downloads/MilSpec/Docs/MIL-DTL-85/dtl85ss3.pdf

[8] J. P. Pousi, D. V. Lioubtchenko, S. N. Dudorov, J. A. Mallat, and A. V. Räisänen, "High Permittivity Dielectric Rod Waveguide Antenna for 110–150 GHz," in *Proceedings of The European Conference on Antennas and Propagation*, 2006.
http://ieeexplore.ieee.org/iel5/4563629/4584476/04584930.pdf

[9] S. Dudorov, "Rectangular Dielectric Waveguide and its Optimal Transition to a Metal Waveguide," Ph.D. dissertation, Helsinki University of Technology,

2002.
http://lib.tkk.fi/Diss/2002/isbn951225901X/isbn951225901X.pdf

[10] R. A. Stern, R. W. Babbitt, J. Borowick, G. Mikucki, and W. Bayha, "A Millimeter Wave Dielectric Waveguide Antenna," *International Journal of Infrared and Millimeter Waves*, vol. 6, no. 10, pp. 999–1016, 1985.
http://www.springerlink.com/content/r11q3265094218g6/fulltext.pdf

[11] N. P. Pathak, "Integration of NRD Guide and Slot Line for Millimeter Wave Indoor Wireless Applications," in *Proceedings of Wave Propagation in Communication, Microwave Systems and Navigation*, 2007, pp. 124–126.
http://archiv.tu-chemnitz.de/pub/2007/0210/data/WFMN07_III_A2.pdf

[12] T. Yoneyama and S. Nishida, "Nonradiative Dielectric Waveguide for Millimeter-Wave Integrated Circuits," *IEEE Transactions on Microwave Theory and Techniques*, vol. MTT–29, no. 11, pp. 1188–1192, 1981.
http://ieeexplore.ieee.org/iel6/22/25096/01130529.pdf

[13] H. Ma and L. Qi, "A new type NRD-guide receiving front-end in Ka-band," *International Journal of Infrared and Millimeter Waves*, vol. 16, no. 10, pp. 1779–1788, 1995.
http://www.springerlink.com/content/t5u5j24j36415307/

[14] T. Teshirogi and T. Yoneyama, Eds., *Modern Millimeter-Wave Technologies*. IOS Press, 2001.

[15] A. A. Oliner, S. T. Peng, and K. M. Sheng, "Leakage from a Gap in NRD Guide," *MTT–S International Microwave Symposium Digest*, vol. 85, no. 1, pp. 619–622, 1985.
http://ieeexplore.ieee.org/iel6/8206/25126/01132055.pdf

[16] H. Ma, "Discontinuity of NRD-Guide and its Application in Millimeter Wave Circuits," *International Journal of Infrared and Millimeter Waves*, vol. 19, no. 10, pp. 1367–1384, 1998.
http://www.springerlink.com/content/u130885072625112/

[17] F. Kuroki, M. Yamaguchi, and T. Yoneyama, "Millimeter Wave Antennas fed by high permittivity LSE-NRD guide," in *Antennas and Propagation Society International Symposium 2001 Digest*, vol. 2. Boston, MA: IEEE, 2001, pp. 262–265.
http://ieeexplore.ieee.org/stamp/stamp.jsp?arnumber=00959705

[18] A. S. Sudbø, "Why are the accurate computations of mode fields in rectangular dielectric waveguides difficult?" *JOURNAL of Lightwave Technology*, vol. 10, no. 4, pp. 418–419, 1992.
http://ieeexplore.ieee.org/iel1/50/3664/00134193.pdf

[19] E. A. J. Marcatili, "Dielectric Rectangular Waveguide and Directional Coupler for Integrated Optics," *Bell Labs Technical JOURNAL*, vol. 48, no. 21, pp. 2071 – 2102, 1969.

[20] G. Lifante, *Integrated Photonics: Fundamentals*. John Wiley & Sons, 2003.
http://eu.wiley.com/WileyCDA/WileyTITLE/productCd-0470848685.html

[21] D. Lioubtchenko, S. Tretyakov, and S. Dudorov, *Millimeter-Wave Waveguides*. Kluwer Academic Publishers, 2003.
http://www.springer.com/engineering/electronics/BOOK/978-1-4020-7531-5

[22] C. Yeh and F. Shimabukuro, *The Essence of Dielectric Waveguides*, 1st ed. Springer, 2008.
http://www.springer.com/engineering/electronics/BOOK/978-0-387-30929-3

[23] C.-L. Chen, *Foundations for Guided-Wave Optics*. John Wiley & Sons, 2007.
http://eu.wiley.com/WileyCDA/WileyTITLE/productCd-0471756873.html

[24] A. Kumar, K. Thyagarajan, and A. K. Ghatak, "Analysis of rectangular-core dielectric waveguides: an accurate perturbation approach," *Optics Letters*, vol. 8, no. 1, pp. 63–65, 1983.
http://www.opticsinfobase.org/abstract.cfm?URI=ol-8-1-63

[25] K. Hattori, M. Yamamoto, and K. Itoh, "A New Transition from Rectangular Waveguide to Image NRD Guide," *Electronics and Communications in Japan (Part II: Electronics)*, vol. 84, no. 10, pp. 9–16, 2001.
http://www3.interscience.wiley.com/cgi-bin/fulltext/85512249/PDFSTART

[26] J. A. G. Malherbe, J. H. Cloete, and I. E. Lösch, "A Transition from Rectangular to Nonradiating Dielectric Waveguide," *IEEE Transactions on Microwave Theory and Techniques*, vol. MTT–33, no. 6, pp. 539–543, 1985.
http://ieeexplore.ieee.org/iel6/22/25149/01133115.pdf

[27] M. Golio and J. Golio, Eds., *RF and Microwave Circuits, Measurements, and Modeling*, 2nd ed. CRC PRESS, 2007.
http://www.crcpress.com/product/isbn/9780849372186

[28] C. A. Balanis, *Modern Antenna Handbook*. John Wiley & Sons, 2008. http://eu.wiley.com/WileyCDA/WileyTitle/productCd-0470036346.html

[29] R. Bansal, Ed., *Handbook of Engineering Electromagnetics*, 1st ed. CRC PRESS, 2004. http://www.crcnetbase.com/isbn/9780824756284

[30] C. A. Balanis, *Advanced Engineering Electromagnetics*. John Wiley & Sons, 1989. http://eu.wiley.com/WileyCDA/WileyTitle/productCd-0471621943.html

[31] L. O. Goldstone and A. A. Oliner, "Leaky-Wave Antennas I: Rectangular Waveguides," *IRE Transactions on Antennas and Propagation*, pp. 307–319, 1959. http://ieeexplore.ieee.org/stamp/stamp.jsp?tp=&arNUMBER=1144702

[32] T. Yoneyama, "Recent Development in NRD-Guide Technology," *Annals of Telecommunications*, vol. 47, no. 11–12, pp. 508–514, 1992. http://www.springerlink.com/content/0k80j507703g51x1/fulltext.pdf

[33] A. Sanchez and A. A. Oliner, "A New Leaky Waveguide for Millimeter Waves Using Nonradiative Dielectric Waveguide," *IEEE Transactions on Microwave Theory and Techniques*, vol. MTT–35, no. 8, pp. 737–747, 1987. http://ieeexplore.ieee.org/iel6/22/25173/01133740.pdf

[34] J. L. Volakis, *Antenna Engineering Handbook*, 4th ed. McGraw-Hill, 2007. http://www.mhprofessional.com/product.php?isbn=0071475745

[35] M. Guglielmi and D. R. Jackson, "Broadside Radiation from Periodic Leaky-Wave Antennas," *IEEE Transactions on Antennas and Propagation*, vol. 41, no. 1, pp. 31–37, 1993. http://ieeexplore.ieee.org/iel4/8/5450/00210112.pdf

[36] C. Brewitt-Taylor, "Limitation on the bandwidth of artificial perfect magnetic conductor surfaces," *IET Microwaves, Antennas & Propagation*, vol. 1, no. 1, pp. 255–260, 2007. http://ieeexplore.ieee.org/stamp/stamp.jsp?tp=&arnumber=4126197

[37] D. F. Sievenpiper, "High-Impedance Electromagnetic Surfaces," Ph.D. dissertation, University of California, Los Angeles, 1999. http://optoelectronics.eecs.berkeley.edu/ThesisDan.pdf

[38] S. Clavijo, R. E. Díaz, and W. E. McKinzie III, "Design Methodology for Sievenpiper High-Impedance Surfaces: An Artificial Magnetic Conductor for Positive Gain Electrically Small Antennas," *IEEE Transactions on Antennas and Propagation*, vol. 51, no. 10, pp. 2678–2690, 2003. http://ieeexplore.ieee.org/stamp/stamp.jsp?tp=&arnumber=1236086

[39] D. Chicherin, S. Dudorov, M. Sterner, J. Oberhammer, and A. V. Räisänen, "Micro-fabricated High-Impedance Surface for Millimeter Wave Beam Steering Applications," in *33rd International Conference on Infrared, Millimeter and Terahertz Waves*. Pasadena, CA: IRMMW-THz, 2008, pp. 1–3. http://ieeexplore.ieee.org/stamp/stamp.jsp?tp=&arnumber=4665714

[40] A. W. Rudge, K. Milne, A. D. Olver, and P. Knight, Eds., *The Handbook of Antenna Design*. Institution of Electrical Engineers, 1981, vol. 1.

[41] S. Gregson, J. McCormick, and C. Parini, *Principles of Planar Near-Field Antenna Measurements*. The Institution of Engineering and Technology, 2007.

[42] W. Hong and W.-X. Zhang, "Analysis of the Characteristics of NRD Waveguides loaded with Periodic Metallic Strips by using the Method of Lines for Millimeter Wave Filter and Antenna Applications," *International Journal of Infrared and Millimeter Waves*, vol. 11, no. 11, pp. 1323–1332, 1990. http://www.springerlink.com/content/h045uv6280157557/fulltext.pdf

[43] F. Schwering and A. A. Oliner, "Millimeter-Wave Antennas," in *Antenna Handbook: Applications*, Y. T. Lo and S. W. Lee, Eds. Kluwer Academic Publishers, 1993, vol. 3, ch. 17, pp. 17–3 – 17–150.

List of Figures

2.1 Decomposition of the (a) electric field and (b) electric flux density at the interface of two dielectrics with different relative permittivity into tangential and nominal components 5
2.2 Cartesian and polar coordinate system 6
2.3 Schematic model of a WR-10 rectangular waveguide for the **W** band having the inner dimensions [mm] $w = 2.54$ and $u = 1.27$ [6] 8
2.4 Electric and magnetic field lines for the TE_{10} mode in the cross-sectional plane of a RWG 9
2.5 Decomposition of the TE_{10} mode into two plane waves inside a RWG 10
2.6 Cross-sectional view of a dielectric rod waveguide with width a and height b having the permittivity ε_r 10
2.7 Illustration of the distribution of the field components E_y and H_x for the E_{11}^y dielectric rod waveguide mode [10] 11
2.8 Principle of operation of the NRD guide: (a) Rectangular waveguide working below cutoff, (b) parallel plates waveguide still below cut-off and (c) low-loss LSM_{01} mode electric and magnetic field lines for non-radiating dielectric waveguides [11] 12
2.9 Cross-sectional view of the NRD guide 13
2.10 NRD guide symmetry planes 14
2.11 Electric and magnetic symmetry plane 14
2.12 HFSS simulation model cross-sections of the NRD guide using electric and magnetic symmetry planes with $a' = a/2$, $b' = b/2$, $d' = d/2$ and $h' = h/2$ 15
2.13 Simulation results of the propagation constant k_z of the classical NRD guide $a = d$ 17

2.14 Simulation results of the guide wavelength λ_g of the classical NRD guide $a = d$ 18
2.15 The cross-sectional view of a dielectric rod waveguide in MARCATILI's method 20
2.16 Cross-sectional view of the vertical dielectric slab waveguide for MARCATILI's method embedded between parallel metal plates (refer to *Figure 2.9c*) with width $a = 2a'$ and distance of the metal plates $d = 2d'$ 22
2.17 Graphical method to obtain the solutions for the transcendental equation (2.68) for k_x with dimensions in mm $a = 0.5$, $b = 1$ and $d = 1.4$; limited by $k_{xl} = k_0\sqrt{\varepsilon_r - 1}$, with $k_{xl|75\text{GHz}} = 5.19$ mm^{-1} and $k_{xl|95\text{GHz}} = 6.57$ mm^{-1} 28
2.18 Cross-section of the horizontal dielectric slab waveguide for MARCATILI's method with thickness b 29
2.19 Graphical method to obtain the solutions for the transcendental equation (2.101) for k_y with dimensions in mm $a = 0.5$, $b = 1$ and $d = 1.4$; limited by $k_{yl} = k_0\sqrt{\varepsilon_r - 1}$, with $k_{yl|75\text{GHz}} = 5.19$ mm^{-1} and $k_{yl|95\text{GHz}} = 6.57$ mm^{-1} 33
2.20 Dispersion diagram $k_z/k_0 - f$ for the NRD guide using the developed MARCATILI method with dimensions in mm $a = 0.5$ and $b = 1$ for different values for the distance between the metal plates d and for the open dielectric rod waveguide (DRW) with $d \gg a$ . . . 35
2.21 Guide wavelength of the NRD guide using the developed MARCATILI method with dimensions in mm $a = 0.5$ and $b = 1$ for different values for the distance between the metal plates d and for the open dielectric rod waveguide (DRW) with $d \gg a$ 35
2.22 Calculated dispersion diagram $k_z/k_0 - f$ of the classical NRD guide with $a = d$ 36
2.23 Calculated guide wavelength λ_g of the classical NRD guide with $a = d$ 37
2.24 Comparison of the calculated and the simulated results for the propagation constant of the NRD guide with dimensions in mm $a = 0.5$, $b = 1$ and varying plate distance d 38
2.25 Comparison of the calculated and the simulated dispersion characteristic $k_z/k_0 - f$ 40
2.26 Comparison of the calculated and the simulated dispersion characteristic $\lambda_g - f$ 41

2.27 Comparison of the calculated and the simulated attenuation constant α for the classic NRD guide with $a = d$ and $b = 0.5$ mm . . . 42
2.28 Metal waveguide to NRD guide transition types: (I) pyramidal transition, (II) side wall opening, (III) direct connection and (IV) direct connection with additional shield plates 44
2.29 NRD guide, RWG cross-section and taper side view dimensions . 45
2.30 Reflection coefficient s_{11}^{dB} of transition type (III) with dimensions in mm $a = 0.5$, $b = 1$ and $d = 1.4$ 46
2.31 Transmission coefficient s_{21}^{dB} of transition type (III) with dimensions in mm $a = 0.5$, $b = 1$ and $d = 1.4$ 47
2.32 HFSS simulation model of the chosen NRD guide with transitions of type (III) with $l = 20$ mm 47
2.33 Reflection coefficient s_{11}^{dB} of transition type (III) for $a = d$ and $b = 0.75$ mm 48
2.34 Transmission coefficient s_{21}^{dB} of transition type (III) for $a = d$ and $b = 0.75$ mm 48
2.35 Metal waveguide to NRD guide transition measurement setup with $l = 32$ mm 49
2.36 Cross-section of the transition measurement setup with dimensions in mm 50
2.37 Top view of the transition measurement setup with dimensions in mm 50
2.38 Picture of the measurement setup showing the experimental NRD guide attached to two metal waveguide sections connected to the VNA 51
2.39 Measured reflection coefficient s_{11}^{dB} of the experimental transition . 51
2.40 Measured transmission coefficient s_{11}^{dB} of the experimental transition 52

3.1 Spherical coordinate system used for antenna parameter computations 54
3.2 Definition of the **E** - and **H** -plane of a vertical polarized antenna . . 54
3.3 Near-field and far-field region surrounding an antenna with diameter D [30] 55
3.4 Foreshortened-top leaky-wave NRD guide antenna developed by Sanchez and Oliner [33]. The leakage of the antenna is controlled by the stub length s. 58
3.5 Principle of operation of a periodic leaky-wave antenna 58

3.6 Cross-section of a Sievenpiper high impedance surface structure [37] 60
3.7 Top view of a Sievenpiper high impedance surface structure [37] . 61
3.8 NRD guide end-fire antenna model 62
3.9 Cross-sectional view of the NRD guide HFSS simulation model for the end-fire antenna with **E** and **H** symmetry planes with dimensions in mm $a = 2a' = 0.5$, $b = 2b' = 1$, $d = 2d' = 1.4$, $t = 0.1$ and $h = 2h'$ 63
3.10 Maximum gain G_0^{dB} (refer to Table 3.1) 64
3.11 Radiation pattern of the NRD guide end-fire antenna 65
3.12 HFSS 3D polar radiation plot of gain G^{dB} for the NRD guide end-fire antenna (a) – (c) without ($s = 0$) and (d) – (f) with extended metal plates ($s = 1.5$ mm), $h = 7$ mm 66
3.13 Comparison of the radiation patterns of the NRD guide and the DRW end-fire antenna for different values of the plate height h in mm for $f_1 = 75$ GHz 68
3.14 Front view of the NSI planar scanner 69
3.15 Side view of the end-fire antenna measurement setup 70
3.16 Top view of the end-fire antenna measurement setup 70
3.17 Scanning area with dimensions in m 71
3.18 Comparison of the simulated and measured far-field radiation patterns 74
3.19 Comparison of the simulated and measured far-field radiation patterns 75
3.20 2D contour plot of the measured radiation pattern for $f_2 = 85$ GHz . 76
3.21 Top view of the NRD guide with discontinuities separated by period p on top of the dielectric: (a) printed strips with $dw = a$ and (b) printed stubs with $dw < a$ 78
3.22 Concept of NRD guide leaky-wave antenna: (a) side view and (b) cross-section with dimensions in mm $a = 1.4$, $b = 0.5$, $s = 1.6$, $t = 0.25$, $p = 2$, $r = 0.01$ and $o = 0.3$ 78
3.23 Concept of periodic leaky-wave NRD guide antennas with PEC discontinuities loaded on the dielectric rod separated by distance p . 79
3.24 Calculated dispersion characteristics $\beta_{-1}/k_0 - f$ of the classical NRD guide with $a = d$ and dimensions in mm $a = 1.4$ and $b = 0.5$, $f_c \approx 96.7$ GHz 80

3.25 **E** -plane radiation pattern of an NRD guide leaky-wave antenna with discontinuities of type (b) shown in Figure 3.21b with dimensions in mm $a = 1.4$, $b = 0.5$, $p = 2$, $dl = 0.5$ and $dw = 0.1$ 81
3.26 beam angle θ_m of an NRD guide leaky-wave antenna with discontinuities of type (b) shown in Figure 3.21b on page 78 with dimensions in mm $a = 1.4$, $b = 0.5$, $p = 2$, $dl = 0.5$ and $dw = 0.1$ 82
3.27 Maximum gain G_0^{dB} of the main lobe of an NRD guide leaky-wave antenna with discontinuities of type (b) shown in Figure 3.21b on page 78 with dimensions in mm $a = 1.4$, $b = 0.5$, $p = 2$, $dl = 0.5$ and $dw = 0.1$ 83
3.28 Tridimensional radiation pattern of the NRD guide leaky-wave antenna with discontinuities shown in *Figure 3.21b* for the frequency range from (a) 92 to (f) 97 GHz with dimensions in mm $a = 1.4$, $b = 0.5$, $p = 2$, $dl = 0.5$ and $dw = 0.1$ 84
3.29 Tridimensional radiation pattern of the NRD guide leaky-wave antenna with discontinuities shown in *Figure 3.21b* for the frequency range from (a) 98 to (f) 103 GHz with dimensions in mm $a = 1.4$, $b = 0.5$, $p = 2$, $dl = 0.5$ and $dw = 0.1$ 85
3.30 Tridimensional radiation pattern of the NRD guide leaky-wave antenna with discontinuities shown in *Figure 3.21b* for the frequency range from (a) 104 to (f) 109 GHz with dimensions in mm $a = 1.4$, $b = 0.5$, $p = 2$, $dl = 0.5$ and $dw = 0.1$ 86
3.31 **E** -plane radiation pattern of an NRD guide leaky-wave antenna with strip discontinuities of type (a) as shown in Figure 3.21a having the dimensions in mm $a = d = 1.4$, $b = 0.5$, $dl = 0.1$ and $p = 2$ 87

A.1 Simulation results of k_z/k_0 of the classical NRD guide with $a = d$. 92
A.2 Simulation results of the guide wavelength λ_g of the classical NRD guide $a = d$ 93
A.3 Calculated attenuation constant α of the classical NRD guide with $a = d$ for $b = 0.5$ mm 94
A.4 Calculated dispersion diagram $k_z/k_0 - f$ of the classical NRD guide with $a = d = 1.4$ mm for different values of the height of the dielectric rod b 95
A.5 Calculated dispersion diagram $k_z/k_0 - f$ of the classical NRD guide with $a = d$ 96

A.6 Calculated guide wavelength λ_g of the classical NRD guide with $a = d$ 97
A.7 Reflection coefficient s_{11}^{dB} of transition type (I) for varied transition length v 99
A.8 Transmission coefficient s_{21}^{dB} of transition type (I) for varied transition length v 100
A.9 Reflection coefficient s_{11} of transition type (II) 101
A.10 Transmission coefficient s_{21}^{dB} of transition type (II) for varied transition length v 102
A.11 Reflection coefficient s_{11}^{dB} of transition type (IV) 103
A.12 Transmission coefficient s_{21}^{dB} of transition type (IV) 103
A.13 Reflection coefficient s_{11}^{dB} of transition type (III) for in mm $a = d = 1.4$ and $b = 0.5$ 104
A.14 Transmission coefficient s_{21}^{dB} of transition type (III) for in mm $a = d = 1.4$ and $b = 0.5$ 104
A.15 Transmission coefficient s_{21}^{dB} of transition type (III) for in mm $a = d = 1.4$ and $b = 0.5$ in the frequency range 85 to 110 GHz 105
A.16 Reflection coefficient s_{21}^{dB} of transition type (III) for $a = d = 1.4$ mm 106
A.17 Transmission coefficient s_{21}^{dB} of transition type (III) for $a = d = 1.4$ mm 107
A.18 Comparison of the radiation patterns of the NRD guide and the DRW end-fire antenna for different values of the plate height h in mm at $f_2 = 85$ GHz 109
A.19 Comparison of the radiation patterns of the NRD guide and the DRW end-fire antenna for different values of the plate height h in [mm] at $f_3 = 95$ GHz 110
A.20 Measured **E** - and **H** -plane radiation pattern for $f_4 = 105$ GHz . . . 111
A.21 Probe compensation **E** -plane radiation pattern showing the smoothing effect 112
A.22 **E** -plane radiation pattern of the NRD guide leaky-wave antenna concept shown in Figure 3.22 113
A.23 **E** -plane radiation pattern of the NRD guide leaky-wave antenna concept shown in Figure 3.22, with in mm $o = 0$ and $s = 0.5$ 113
A.24 Reflection coefficient s_{11}^{dB} of an NRD guide leaky-wave antenna with discontinuities of type (b) shown in Figure 3.21b on page 78 with dimensions in mm $a = 1.4$, $b = 0.5$, $p = 2$, $dl = 0.5$ and $dw = 0.1$ 114
A.25 **E** -plane radiation pattern for different dimensions of the distontinuities with $f = 95$ GHz and $p = 2$ mm 114

D.1 *HFSS* NRD model showing the simulation boundaries and the dimensions of the NRD guide and the dielectric rod in mm 119
D.2 Phase shift $\varphi_{s_{21}}$ at the output port compared to the incident phase at the input port 120
D.3 Magnitude of the electric field in the vertical plane of the NRD guide model at $f_l = 75$ *GHz* showing the number of full rotations the electromagnetic wave experience along the guide structure ($N = 8$) 121
D.4 Cumulative phase shift $\phi_{s_{21}}$ along the NRD guide structure at the output port 121
D.5 Dispersion curve $k_z/k_0 - f$ of the NRD guide model 122
D.6 Guide wavelength $\lambda_g - f$ of the NRD guide model 122

E.1 Schematic model of the dielectric rod waveguide antenna with RWG to DRW transition 123
E.2 (a) Cross-section of the metal waveguide to DRW transition and (b) DRW end-fire antenna simulation cross-section with dimensions in mm $a = 2a' = 0.5$ and $b = 2b' = 1$ 124
E.3 Radiation patterns of the DRW end-fire antenna 125
E.4 Normalized gain $G^{\mathrm{dB}} - G_0^{\mathrm{dB}}$ of the DRW antenna for $f_1 = 75$ GHz . . 126
E.5 Normalized gain $G^{\mathrm{dB}} - G_0^{\mathrm{dB}}$ of the DRW antenna for $f_2 = 85$ GHz . . 126
E.6 Normalized gain $G^{\mathrm{dB}} - G_0^{\mathrm{dB}}$ of the DRW antenna for $f_3 = 95$ GHz . . 127